HIGH-SPEED QUANTITATIVE SCHLIEREN MEASUREMENT OF DENSITY FIELDS AROUND CONICAL SUPERSONIC PROJECTILES

by

Jason Michael Falls

Submitted in Partial Fulfillment
of the Requirements for the Degree of
Master of Science in Mechanical Engineering
with Specialization in Explosives Engineering

NEW MEXICO TECH
SCIENCE • ENGINEERING • RESEARCH UNIVERSITY

New Mexico Institute of Mining and Technology
Socorro, New Mexico
April, 2022

ACKNOWLEDGMENTS

I would like to acknowledge my family and friends for their support and encouragement to pursue a graduate degree. I would also like to thank the members of Dr. Michael Hargather's Shock and Gas Dynamics Laboratory for assistance with field setup and test series support.

I would like to acknowledge my research adviser Dr. Michael Hargather for providing assistance and pushing me to learn best research practices and the mentorship received through my degree.

I would like to acknowledge Jeff Edmonds formerly of the New Mexico Tech Mechanical Engineering department machine shop for his assistance with machining the projectiles ballistically launched throughout this thesis.

This research was performed under funding from of the US Department of Energy Lawrence Livermore National Laboratory through Contracts: B645442 and B641460.

ABSTRACT

Supersonic attached shock waves in the form of oblique conical shock waves present a simple geometry which has a well known flow solution in the form of the Taylor-Maccoll conical flow solution. The application of quantitative schlieren imaging applied to two and three dimensional flows such as the Taylor-Maccoll conical flow has been applied for wind tunnel testing and free air blast measurements. Quantitative schlieren and background oriented schlieren reconstructions of ballistically obtained Taylor-Maccoll conical flow are presented. Refractions are recorded along the entire optical path and the three dimensional Abel inversion is applied utilizing an axi-symmetric spherical constraint to reconstruct the density profile around 10° half-angle cones. The density results are compared with the theoretical Taylor-Maccoll conical flow solution evaluated numerically and parametrized by cone geometry and Mach number. Agreement is seen between the experimental reconstructed density fields and the theoretical density profile. Quantitative high-speed measurements are shown to agree with theoretical density profiles even when considering the resolution constraints inherent to high-speed imaging.

Keywords: schlieren imaging, optical characterization, Abel inversion, background oriented schlieren, ballistic launch

CONTENTS

LIST OF TABLES

LIST OF FIGURES

LIST OF ABBREVIATIONS

a	Counter
b	Current height above cone surface
c	Sound speed
d	Physical diameter
f	Focal length of lens
g	Nondimensional height above cone
h	Total height from cone surface to oblique conical shock wave
i	Abel inversion index
j	Abel inversion index
k	Gladstone Dale coefficient
n	Refractive index
p	Pixel to distance calibration length
t	Background Oriented Schlieren length from refractive object to camera
u	Horizontal pixel shift
v	Vertical pixel shift
w	Width of bounding box from regionprops
x	Right handed Cartesian coordinate
y	Right handed Cartesian coordinate
z	Right handed Cartesian coordinate
dz	Depth of refracting object
L	Background Oriented Schlieren length from background to camera
M	Mach number
P	Absolute pressure
R	Specific gas constant for air
T	Absolute Temperature
I	Pixel intensity
$\bar{I}$	Average background intensity
N	Number of points in Abel inversion

γ	Ratio of specific heats
δ	Cone half angle or wedge angle
θ	Wave angle
λ	Wavelength of light
ρ	Density
ω	Number of twists in gun barrel
Ω	Twist rate in gun barrel
A_x	Cone apex x coordinate
A_y	Cone apex y coordinate
$A_{i,j}$	A matrix for Abel inversion calculation
$B_{i,j}$	B matrix for Abel inversion calculation
C_D	Coefficient of drag
C_L	Coefficient of lift
d_{CHT}	Diameter obtained from Circular Hough Transform
$D_{i,j}$	Linear coefficient matrix for Abel inversion calculation
G_x	Bounding box centroid x coordinate
G_y	Bounding box centroid y coordinate
L_g	Length of gun barrel
$n(r_i)$	Refractive index at radial position
n_0	Atmospheric refractive index
P_1	Pressure in gun headspace and cartridge
P_2	Pressure along gun barrel
T_r	Target t/L ratio
u_t	Tangential component of velocity in Taylor-Maccoll
v_m	Velocity
V_1	Volume in gun headspace and cartridge
V_2	Volume along gun barrel

α_i	Error associated with i'th component
α_z	Total error of function
$\Delta\varepsilon$	Change in refractive angle
$\delta(r_i)$	Change in radial position for Abel inversion calculation
ε_x	Refractive angle in x direction
ε_y	Refractive angle in y direction
θ_t	Angle of inclination of conical ray
ρ_c	Density at cone surface
ρ_t	Stagnation density
ρ_1	Atmospheric density
ρ_2	Density inside oblique conical shock wave
$\frac{\partial Z}{\partial a_i}$	Partial of function Z with respect to a_i
$\frac{dn}{dy}$	Derivative of refractive index with respect to y
AoA	Angle of Attack
BMG	Browning Machine Gun
BNC	Bayonet Neill-Concelman
BOS	Background Oriented Schlieren
CCI	Cascade Cartridge Incorporated
CHT	Circular Hough Transform
CNC	Computer Numerical Control
CT	Computed Tomography
DC	Direct Current
DIC	Digital Image Correlation
dpi	dots per inch
EMRTC	Energetic Materials Research and Testing Center
fps	Frames per second
IBHVG2	Internal Ballistics of High Velocity Guns Version 2
IMR	Improved Military Rifle
LED	Light Emitting Diode
PDGS	Propellant Driven Gun System
PEEK	Polyetheretherketone
TTL	Transistor Transistor Logic

This thesis is accepted on behalf of the faculty of the Institute by the following committee:

Michael Hargather

Academic and Research Advisor

Alejandro Campos

Tie Wei

I release this document to the New Mexico Institute of Mining and Technology.

Jason Michael Falls February 8, 2022

CHAPTER 1

INTRODUCTION

1.1 Research Motivation

Shock waves form in supersonic and hypersonic flows when the conservation of mass, momentum, and energy equations cannot be satisfied without an instantaneous jump in gas parameters such as temperature, density, pressure, and velocity. Shock waves are thus instantaneous disturbances separating regions of different flow properties. The shock waves that form around certain simple geometries traveling at supersonic speeds can be mathematically characterized via simplifying assumptions. One such geometry is a cone, where the attached shock wave is another cone with a different half-angle than that of the projectile. The angle of inclination of the shock wave to the flow, or wave angle, is ultimately a function of cone geometry and velocity of the projectile. The property variation around cones has been mathematically characterized by Taylor [1] and expanded upon by Maccoll [2]. A potential flow function is defined for the projectiles and conservation is solved similarly to oblique shock waves by orthogonally decomposing the flow into normal and tangential components. A flow condition where the flow has no normal flow component at the cone face is obtained by numerically solving the Taylor-Maccoll conical flow conservation equation. Although the theory developed by Taylor and Maccoll is widely accepted for conical flows, no direct experimental measurement of the density field surrounding conical projectiles in free flight has been performed.

1.2 Refractive Imaging Techniques

Refractive imaging techniques visualize variations in refractive index in transparent flow fields [3]. In gases, the refractive index is a function of the local density. As a result of the property variation around supersonic cones, small refractions of light occur. It is possible to measure and quantify the magnitude of these property variations through optical techniques. For gaseous species the local density can be related to the refractive index via the Gladstone-Dale law:

$$n = k\rho + 1 \tag{1.1}$$

where n is the refractive index, ρ is the gas density, and k is the Gladstone Dale constant for the gaseous species. Density gradients are thus refractive index gradients, which can be visualized.

1.2.1 Schlieren

Schlieren imaging was first described by Robert Hooke in the 17th century and later realized and popularized by August Toepler [3]. Schlieren imaging in the fashion of Toepler is the technique most widely adopted today [3]. The usage of schlieren imaging is ubiquitous in shock physics and provides both qualitative and quantitative analyses of flows containing refractive disturbances.

Schlieren imaging visualizes refractive index differences in the form of grayscale intensities which can be characterized through the quantitative schlieren process [4]. A typical schlieren system contains two parabolic mirrors or planoconvex achromatic lenses which are used to collimate and converge light respectively. Figure 1.1 displays a typical schlieren system which uses two achromatic doublet lenses. A point source of light is placed at the focal length of the lens or mirror, creating parallel light. Another lens is placed an appropriate distance away from the collimating lens, collecting and focusing the light. At the focal point a simple cutoff or mask is placed to interact with the light. Schlieren imaging is characterized by a light to dark variation due to the interaction of refracted light with the cutoff. Typical cutoffs include a razor blade or an ideally infinitely sharp edge. A camera is placed on the diverging side downstream of the masked focal point. The schlieren methodology visualizes the first derivative of refractive index and is mathematically described by:

$$\varepsilon_y = \frac{1}{n} \int \frac{dn}{dy} dz \tag{1.2}$$

where ε_y is the refractive angle in the plane orthogonal to the orientation of the razor blade, $\frac{dn}{dy}$ is the gradient of refractive index in the y coordinate, and dz is the depth of the refracting object.

The schlieren method yields the path integral of refractions along the entire optical path. The path integral yields the gradient of refractive index integrated over the depth of the refracting object.

Color or rainbow schlieren imaging utilizes the same test setup, but uses a color camera and a filter instead of a razor blade cutoff. The color filter can provide quantitative measures of density via the observed color [5]. The bidirectional heterodyne color schlieren technique discussed by Stricker et al. [6] changes the source slit to contain both a vertical and horizontal dimension. The knife edge is replaced by a filter containing both red and blue regions orthogonal to one another. Behind the filter a color camera is placed. The orthogonal grid causes vertical refractions to be recorded in the red plane, and horizontal refractions to

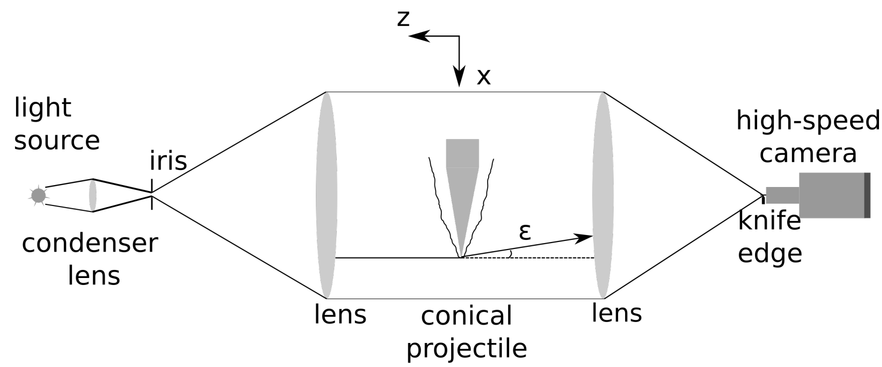

Figure 1.1: Typical schlieren schematic for lens type schlieren measurements

be recorded in the blue plane of the image. This methodology has been utilized for comparisons of vertical and horizontal refractive calibration and analysis.

Color gradient schlieren has been used to quantitatively measure the density change around a flat plate-wedge model. The results compare well with Prandtl-Meyer theory for the density change around a flat plate [7]. The orthogonal refraction data obtained through the color imaging is not required to accurately reconstruct the fields as shown in Elsinga at al. [7]. The limitations with color schlieren include less light sensitivity and more sensor noise as a result of the Bayer demosaicing applied to recorded intensity values. These additional constraints without need for the orthogonal refractive fields limit the application of color or rainbow schlieren.

1.2.2 Shadowgraph

Shadowgraph imaging is another refractive technique with similar light to dark variations, but doesn't provide information on the specific orientation of the refraction. Focused shadowgraph simplifies the field lens or mirror type schlieren methodology by simply removing the knife edge. A focused shadowgraph system contains parallel light which allows for a direct projection of objects and their refractive disturbances into a camera. Focused shadowgraph visualizes the Laplacian of refractive index and can be used to qualitatively observe flow features causing a refractive disturbance. The deconvolution of the two derivatives is too complicated to perform quantitative calibration, but size analyses are possible using shadowgraph techniques for diagnostics on location, and geometry of shock features as discussed in Winter [8].

1.2.3 Background Oriented Schlieren

Background Oriented Schlieren (BOS) is a post-processing technique to visualize refractive disturbances via their distortion to a background pattern as reviewed by Raffel [9]. BOS is traditionally performed in diverging light and relies on a post-processing correlation or other operation to determine shifts between a "cold" image and the distorted "hot" image. The "cold" image is that obtained when the flow is not present, or when there are no refractive disturbances. Multiple methodologies can be used to determine the shift between the cold image and the hot image, but one of the simplest is through using a correlation algorithm which searches within an image for areas of high contrast with distinct patterns [9]. The BOS methodology relies on knowledge of the physical testing setup including distances between the refractive disturbance and the background. Figure 1.2 displays the general schematic for a BOS imaging setup. Typical diverging light results in the schlieren plane and the background plane being of different physical size. Geometric corrections between the relative plane sizes are performed to determine the physical size from the projected size imaged on the background plane.

Typical high-speed BOS measurements struggle with obtaining enough light on the background plane such that sufficient contrast can be picked up by the camera. Cameras with very high light sensitivity are necessary to provide sufficient dynamic range and resolution for BOS measurements. Additional considerations for aperture adjustment provide another requirement for focusing. Large focal length camera lenses have narrow regions of focus resulting in a necessary stopping down of the aperture such that depth of field is appropriate for keeping both background plane and schlieren plane in reasonable focus. The geometric values of t and L relate to the BOS sensitivity and are used to obtain the refractive angles ε. Adjustments to obtain the ideal BOS setup have been discussed by Hargather and Settles for the appropriate t/L setup, aperture, and shutter speeds [10].

A pixel shift from the image registration is obtained as a vector valued quantity projected onto either horizontal or vertical pixel shifts, u or v, respectively. The vector refraction intensities are obtained through trigonometry of the setup via:

$$\frac{\text{pixel shift p}}{L - t} = \tan \varepsilon \tag{1.3}$$

The refractive angle from the field is the same as that obtained through traditional lens or mirror based schlieren techniques except with some distortion due to the correlation or post processing technique.

BOS imaging is highly scalable and offers a methodology to obtain schlieren results for larger scales and with a simpler testing setup. BOS measurements can be performed utilizing natural backgrounds and can have essentially a limitless scale. The applicability of BOS is only hindered by the reduction in resolution seen as a result of the correlation between the two images.

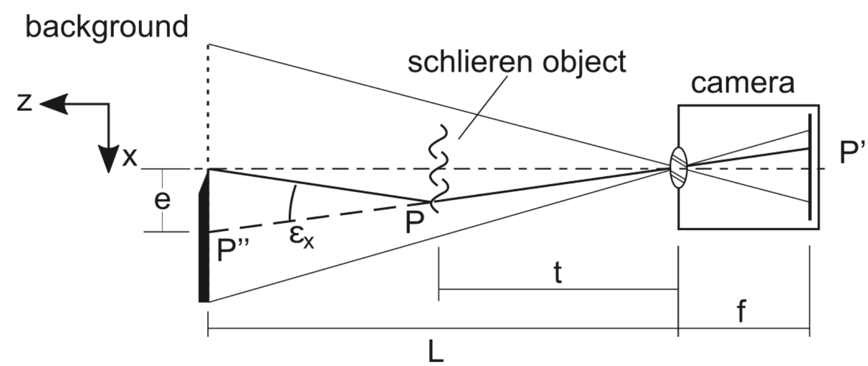

Figure 1.2: Schematic of traditional BOS setup displaying refractive plane and background plane. Values t and L are varied to change the sensitivity of the BOS system

1.3 Compressible Flow

General compressible flow relationships are derived from conservation of mass, momentum, and energy, and an equation of state. For most applications the assumptions of compressible flow are inviscid, steady state, and ideal gas. Shock waves occur when a flow is traveling faster than the sound speed of the material, and property variations are ultimately characterized as a function of Mach number and geometry of the shock wave [11]. The Mach number (M), named for Ernst Mach, is defined as the local velocity divided by the sound speed in the material:

$$M = \frac{v_m}{\sqrt{\gamma R T}} \tag{1.4}$$

where v_m is the velocity of the air, γ is the specific heat ratio, R is the specific gas constant, and T is the absolute temperature of the gas.

Normal shock waves are the simplest kind of shock wave which occur when a uniform flow encounters the shock wave perpendicularly, which simply results in a discontinuous jump in density, pressure, temperature, and velocity of the flow. Normal shock wave analysis forms the basis for analysis of compressible flow phenomena and is a one dimensional process moving from a non-shocked to a shocked environment. On the front of a bow shock of a projectile sits a nearly normal shock wave resulting in the streamline passing through the center of a bow shock having the greatest density, temperature, and pressure rise within the flow around the projectile. This streamline moves from a non-shocked condition to a normal shocked condition according to:

$$\frac{\rho_2}{\rho_1} = \frac{(\gamma+1)M_1^2}{(\gamma-1)M_1^2+2} \tag{1.5}$$

The normal streamline continues past the shock up to the surface of the projectile. Since the fluid cannot flow through the projectile itself, this streamline must come to a stop at the surface of the projectile. The slowing process is modeled as an isentropic compression to stagnation at the face of the projectile. The stagnation relationship is defined as:

$$\frac{\rho_t}{\rho} = \left(1 + \frac{\gamma - 1}{2} M^2\right)^{\frac{1}{\gamma - 1}} \tag{1.6}$$

Compressible aerodynamics relationships for low Mach Numbers ($M \leq 5$) are defined under the assumptions of the ideal gas law, inviscid flow, isentropic flow everywhere besides shock waves. Since the density is a property that is directly related to the refractive index of the gas through the Gladstone Dale relationship it can be measured directly. The ideal gas law for density is:

$$\rho = \frac{P}{RT} \tag{1.7}$$

The local atmospheric density is typically determined from measured quantities and is used to determine the specific values of other properties at locations around the projectiles.

Around a projectile, an oblique shock wave is present. An oblique shock wave is a shock wave that is inclined at an angle to the flow. These shock waves result from a turning motion of the flow. The compression from this turning through angle δ causes a shock wave at an inclined angle θ, as shown schematically in Figure 1.3. Analysis for this case is to break the flow into tangential and normal components with respect to the wave angle θ. The tangential component is unaffected by the presence of the shock wave, and the normal component encounters a shock wave that is normal to its direction of travel. The normal shock relationships defined by Equation 1.5 are applied to this component of the flow. Downstream of the shock wave, a recombination of the flow properties is performed, and the local properties can be calculated for the flow. All property variations arise in this flow condition as a result of the normal component passing through the oblique shock wave. Three dimensional effects around projectiles result in differing shock strengths, but are largely based on the analysis of an oblique shock wave.

1.3.1 Conical Supersonic Flow

One common geometry which doesn't create large changes in properties of the flow is a cone. An attached shock wave is one which originates from the tip of the cone, and is a function of the sharpness of the projectile and the velocity at which it is traveling. The sharper the body in supersonic flow conditions, the more likely that the shock wave will be attached to the body. Conical flow is developed under the assumption that the shock wave is attached to the body.

Cones have a wide variety of applications due to the relative weakness of the attached shock waves which occur on a sharp curved body. Supersonic aircraft such as the Lockheed Martin SR-71 Blackbird leveraged the highly predictable nature of conical flow to attach a shock between the spike of the engine housing and the body of the aircraft [12]. Translation of the spike was designed such that the shock-wave angle θ would be consistent with the cone half angle and the current velocity. The attached shock is a so called "started inlet" for the subsonic air breathing engine.

First mathematically studied by Taylor and Maccoll in the 1930's, conical flow has been mathematically and experimentally characterized via wind tunnel and ballistic testing [1, 2]. The Taylor-Maccoll conical flow approximation provides a basic avenue for which to compare experimentally measured conical-flow property variations. The conservation of mass, momentum, and energy equations are recast as functions of position along cone and conical ray wave angle θ_t. The assumptions of irrotational flow and isentropic compression within the shock layer are applied. The conservation equations under the assumption of irrotational flow become an ordinary differential equation in terms of the sound speed c, ratio of specific heats γ, the ray wave angle θ_t, and the tangential component of velocity u_t along the conical ray as defined by:

$$\begin{aligned} \frac{1}{c} * \frac{\mathrm{d}^2 u_t}{\mathrm{d}\theta_t^2} \left\{ \frac{\gamma+1}{2c^2} \left(\frac{\mathrm{d}u_t}{\mathrm{d}\theta_t} \right)^2 - \frac{\gamma-1}{2} \left(1 - \frac{u_t^2}{c^2} \right) \right\} &= (\gamma-1) \frac{u_t}{c} \left(1 - \frac{u_t^2}{c^2} \right) \\ + \frac{\gamma-1}{2c} \left(1 - \frac{u_t^2}{c^2} \right) \cot\theta_t * \frac{\mathrm{d}u_t}{\mathrm{d}\theta_t} - \frac{\gamma u_t}{c^3} \left(\frac{\mathrm{d}u_t}{\mathrm{d}\theta_t} \right)^2 &- \frac{\gamma-1}{2c^3} \cot\theta_t \left(\frac{\mathrm{d}u_t}{\mathrm{d}\theta_t} \right)^3 \end{aligned} \tag{1.8}$$

The ordinary differential equation is evaluated numerically to determine the velocity tangential to the cone surface. When the flow in the normal direction is zero, a continuity equation for pressure inside the oblique conical shock wave and at the cone surface is found. An oblique shock wave analysis on the flow is performed in order to determine the the appropriate shock wave angle θ for the cone half angle and Mach number. The wave angle for a conical shock is weaker and has a shallower wave angle (θ) for a cone than a wedge with the same angle (δ). An iterative calculation is performed to determine the shock wave angle based on normalized position and the oblique shock wave relationships. It follows from the shock condition that the properties vary only along conical rays originating from the apex of the supersonic cone as discussed further by Anderson [11]. Figure 1.3 schematically shows the inclination of conical rays in the geometry, and a schlieren image of a ballistically launched cone. The highest property values are obtained at the cone surface due to the stagnation at the surface.

A wide study of the property variations along conical rays utilizing this analysis path have been performed in the past. As with many compressible flow

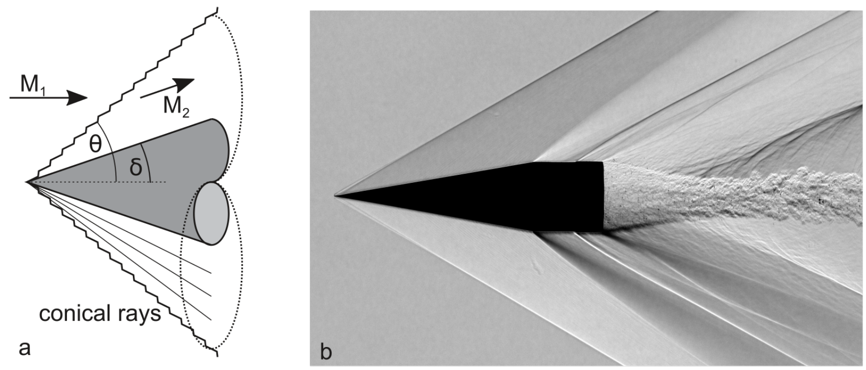

Figure 1.3: a. Cone schematic of property variation along inclined conical rays. b. Sample cone schlieren image

phenomena, the results are presented in tabular or graphical form. From these studies, the conservation is recast such that an input of Mach number and cone half angle can be used to look-up the high speed gas properties [13]. Limitations to the Taylor-Maccoll conical flow solution are discussed in Whitham indicating that the flow solutions work exceptionally well for cones with half angle $\leq 10^\circ$ and Mach numbers below 3 [14].

1.3.2 Supersonic Flow Around Blunt Bodies

Cone flow assumes that a cone is sufficiently sharp that the shock wave is attached to the body. The sharper the projectile, the more likely that the shock wave attaches to the body [11]. A blunted body causes the shock waves to detach from the body and form a bow shock. The bow shock characteristics are highly dependent on geometry, but has been studied for specific geometries with that are predominantly cone shaped [15, 16]. The addition of the standoff between shock wave and projectile body results in a stagnation point which is not the origination point of an oblique conical shock wave, but rather at the center of the projectile face. Bow shocks occur due to the bluntness or as a result of an attempt to turn the flow too much and a stronger shock wave forms away from the body as shown in Maccoll's contact shadowgrams [2].

The pressure, density, and temperature are highest on the surface of the blunted part of the projectile and are of particular interest for characterization [11]. The flow around a blunted body has been characterized through simulations and wind tunnel testing [16]. Ballistic performance is of specific interest in the fields of bullet manufacture and many aerospace or defense applications.

1.4 Projectile Research and Conical Flow in Literature

In 1937, Maccoll published a continuation paper containing data of contact shadowgrams visualizing conical projectile flow [2]. A series of discussions of the conical flow and associated wave angles were presented and how theoretical wave angle and measured wave angle compare when using a ballistic method to launch projectiles. This method provides an accurate measure of velocity when resolution is sufficiently high and has been used in the past as discussed by Anderson [11].

Other properties of cone flow such as the drag coefficient have been studied both numerically and in wind tunnels. Experiments have typically measured relevant forces experienced by the cone through an instrumented sting in a wind tunnel as performed by Owens [16]. The wind tunnel testing also investigated the effect of a spherical blunt on the nose of cones [16]. Spherically blunted cones are common in hypersonic applications and will have a bow shock standing off the projectile to change aerodynamics and heat transfer where stagnation of the flow occurs. The experiments on the spherically blunted cones in supersonic flows are used to evaluate the drag as a function of a bluntness ratio, that is, the ratio of the diameter of the spherical blunt and the diameter of the projectile.

Multiple cone half angles, bluntness ratios, and flow conditions were evaluated. Qualitative film schlieren photos were taken during the investigation, providing an insight into the distance between oblique shock and cone surface. The schlieren images show flow structure and display the locations of shock waves and expansion fans. Large property changes in the gas around the ballistic bodies is shown through the individual sensitivity of the schlieren system used.

While the schlieren images obtained by Owens are largely qualitative, the schlieren images are useful for validating the shape of the bow shock and provide a visualization of the flow around multiple geometries of cones [16]. Additionally, the discussion on the design of the spherical blunts on the cones provides a framework to compare experimental results with.

The drag around a conical projectile that has a sharp or blunt nose and a cylindrical base has been evaluated semi-empirically and compared with wind tunnel measurements. A similar geometry is commonly found in aerospace or ballistic bodies and is the subject of substantial research and characterization. Madhi discuss the drag's dependance on properties such as Mach number and angle of attack (AoA) [17]. A comparison with numerically obtained correction factors for each drag coefficient and relevant geometry are performed. Conical geometries form the basis for all ballistic projectiles and are highly optimized by bullet manufactures such as Hornady [18]. The blunted ogive body of revolution of bullets is tested for a ballistic coefficient of interest. The ballistic coefficient is a function of the mass of the bullet, the frontal area, and the experimentally determined drag coefficient.

1.4.1 Experimental Studies of Property Variation around Cones

Quantitative schlieren measurements have been recorded in wind tunnels by Venkatakrishnan and Meier [19]. The use of the BOS technique and a radon filtered backprojection algorithm from a single image of an axi-symmetric model in a supersonic wind tunnel allowed measurement of the density field around the cone model. Agreement is seen between Taylor-Maccoll cone tables and density profiles obtained through the backprojection algorithm. Kato et. al. [20] discuss a color grid background oriented schlieren method for reconstruction of density change around the projectiles using a computed tomography method similar to Venkatakrishnan, and discuss artifacts of the Computed Tomography (CT) reconstruction. Kato et. al. [20] and Venkatakrishnan and Meier [19] present traditional color and grayscale schlieren images respectively of conical flow. The schlieren images provide a color variation or grayscale intensity proportional to the density gradient used for a qualitative comparison with the BOS measured density profiles.

Conventional schlieren and BOS measurements have been performed and compared by Fisher et. al. for low hypersonic conical flow around a flared cone model [21]. The comparisons provide a quantitative comparison for the intensity of the refractions simply between one knife edge orientation and the displacements which are present in a single orientation in the displacement field obtained through BOS. Discussion on the unsteady nature of the wind tunnel state results in deviation from steady-state flow around the model. Fisher provides an analysis in the low hypersonic regime where additional considerations for ideal gas are no longer appropriate and as such provides quantitative comparisons only with the refractions visualized by both BOS and schlieren methodologies.

1.5 Goals of Current Research

The present research is focused on developing a methodology to reconstruct density variation around ballistically launched conical projectiles using quantitative schlieren and BOS measurement techniques. Comparisons between the accuracy of schlieren and BOS measured density fields are made. Previous works for characterizing the property variation around cones have been limited to wind-tunnel testing with static schlieren measurement and the inclusion of a sting on the projectile to hold it in place in the wind tunnel test section. To expand on previous efforts, the goals of this research are to:

1. Further develop quantitative traditional and background-oriented schlieren methods, apply them to steady-state cone flow, and validate against the theoretical Taylor-Maccoll solutions

2. Design and predict ballistic performance of conical projectiles in varying flow conditions and of varying geometries

3. Develop and characterize a new Background Oriented Schlieren methodology leveraging parallel light
4. Expand upon previous efforts for the Abel inversion based quantitative schlieren
5. Perform a direct comparison between steady state cone flow for both schlieren and BOS reconstructed densities

CHAPTER 2

EXPERIMENTAL METHODS

A series of tests of conical projectiles, smokeless black powders, and gun parameters was performed using the New Mexico Tech Propellant Driven Gun System (PDGS) on the Energetic Materials Research and Testing Center's (EMRTC) field lab. Multiple tests were conducted using parallel light schlieren systems and BOS systems to characterize property variation around the projectiles.

2.1 Propellant Driven Gun System

The PDGS is a system designed to launch projectiles of varied diameters using gun propellant. The system is based around a universal receiver into which gun barrels of varying characteristics are mounted. Each gun barrel is chambered to hold a 0.50″-caliber (12.7 mm diameter) Browning Machine Gun (BMG) brass cartridge. Individual gun barrels have different bore diameters and rifling. The primary gun barrel used here is a 0.50″-caliber (12.7mm diameter) rifled barrel. Traditional rifled barrel measurements are defined by:

$$\Omega = \frac{L_g}{\omega} \tag{2.1}$$

where: Ω is the twist rate, L_g is the length of the barrel and ω is the total number of rotations in the barrel. The standard units for Ω is: in/twist

The 0.50″-caliber (12.7mm diameter) 50BMG barrel used here has a twist rate 30:1 and a total length of approximately 84 cm (33.1″). Thus indicating that the gun barrel contains approximately 1.10 total twists. Figure 2.1 and 2.2 display the complete PDGS system.

The PDGS sits on a recoil carriage which is designed to damp the recoil during ballistic launch of projectiles from the universal receiver. This carriage and stand ultimately translate all forces into the foundation of the building to which it is bolted. The universal receiver and recoil carriage are mounted onto a plate that is pinned at the front and sits on an adjustable elevation controller in the rear. The elevation controller provides fine control over the pitch of the gun barrel. High precision bubble levels are mounted to the universal receiver to ensure that the shot line is leveled.

The universal receiver includes both electrical and pneumatic isolation valves for the pneumatically actuated firing pin. The pneumatic system works together with the electrical system to safely fire the PDGS only when all safety mechanisms have been disarmed. The pneumatic system works to strike the firing pin which initiates the detonation-deflagration train that pushes the projectile through the gun barrel. The electrical isolation switch is designed as a safety mechanism, but also allows for an electrical measurement of the state of the PDGS. When the PDGS is triggered, an electrical zero time is obtained. An in-depth research plan discussing the specific operational steps for launching the cones can be found in Appendix D.

The gun zero time is obtained from a 24V trigger signal sent to the PDGS which opens the electro-pneumatic switch, in turn striking the firing pin and initiating the primer. The 24V trigger box is designed with both a momentary key switch and momentary button switch to ensure that the key must be held in the on position and the button must be pressed simultaneously to initiate the primer. The primer ignites the gun propellant which deflagrates and generates a propulsion force on the bullet in the barrel. The deflagration of the smokeless black powder propels the projectile through the rifled gun barrel and accelerates it to the desired velocity at exit of the barrel. Downrange of the gun barrel, a ballistic light gate system is set up to trigger the high-speed camera and pulsed imaging laser illumination source. The projectile is imaged as it passes through the schlieren test section. The zero time for the camera is obtained from the ballistic light gate and is the zero time for the high-speed schlieren imaging. The light gate unit runs off of 5V DC and contains a 850nm LED emitter and an 850nm photodiode which drops a 5V Transistor Transistor Logic (TTL) signal from high to low. A Stanford Research Systems' DG535 delay generator box controls the timing for the illumination and high speed camera. Further technical specifications on the ballistic light gate and laser illumination source are included in Apendicies B and C, respectively. The internal ballistics and muzzle velocity of the projectiles must be characterized to ensure that the desired velocity will be achieved from a given amount of smokeless black powder gun propellant.

Ballistics model predictions provide a method to validate the safety and overall ballistic performance of the projectiles. Projectiles are hand-loaded into a commercial 0.50″-caliber gun followed by a case with a known mass of smokeless black powder and an associated primer. Nominally, the ballistic launch system's cartridges can withstand $370 \leq x \leq 417$ MPa ($54 \leq x \leq 60$ ksi) [22, 23] of breech pressure without permanently deforming and causing damage to the PDGS. In addition to the limitation of overpressure on the 50BMG cases, an overpressure failure of the projectile can also occur. The overpressure of the projectile will cause significant deformation and loss of the gas seal between the projectile and gun barrel. Design considerations for the gas seal and internal ballistics modeling must be performed to ensure that the projectile will survive ballistic launch and neither the case nor the projectile are overpressured.

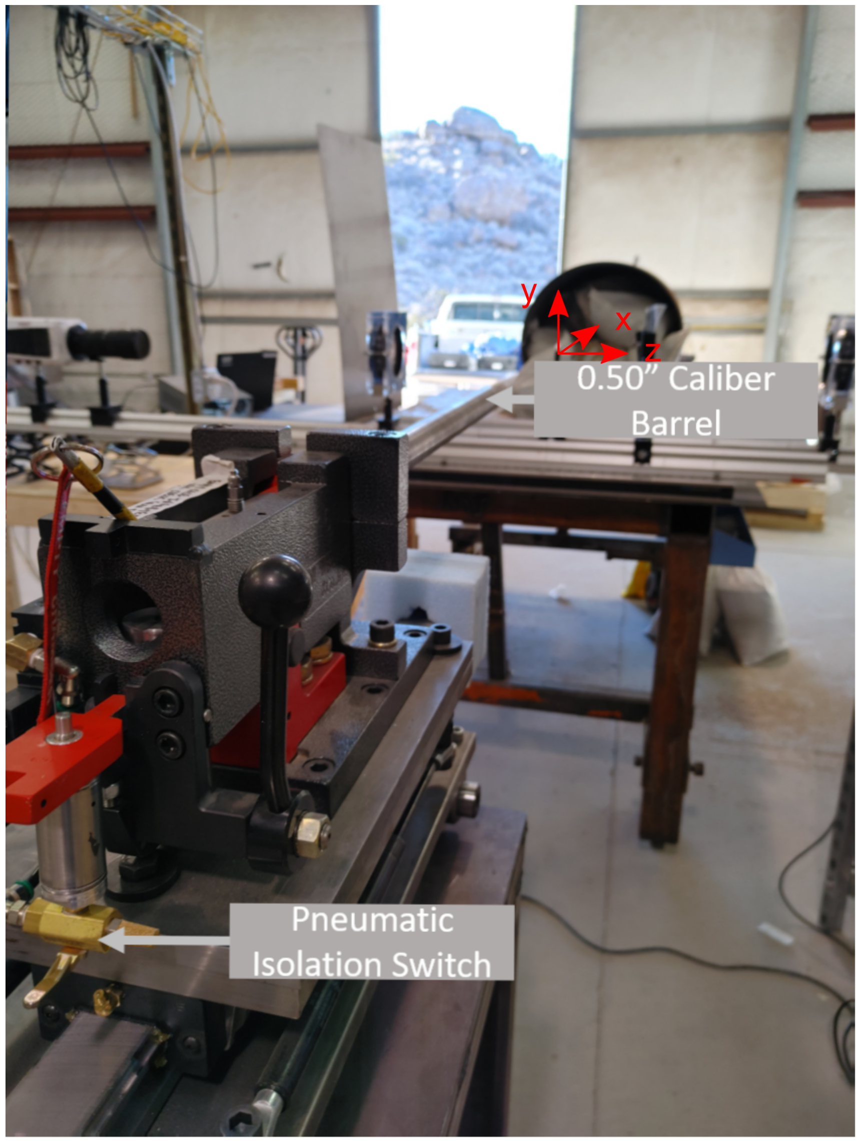

Figure 2.1: PDGS setup from right displaying pneumatic isolation switch

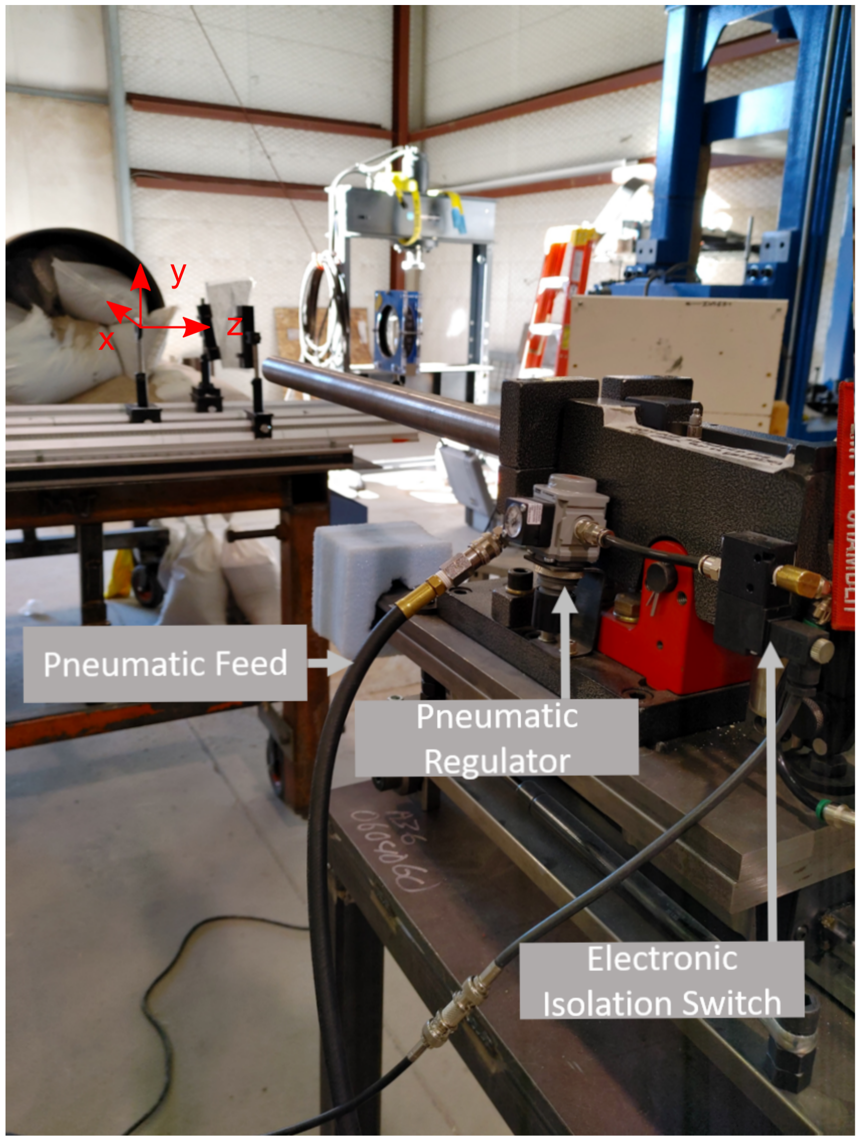

Figure 2.2: PDGS setup from left displaying pneumatic feed, pneumatic regulator, and the electronic isolation switch

2.1.1 Rifled Projectile Design

The large forces caused by the ballistic launch require materials for the projectile be sufficiently strong. On the other hand, the hardness of the projectiles must be less than that of the hardness of the rifling in the gun barrel such that no excessive wear or damage to the rifling occurs [24]. Typical materials which posses high strength, and low hardness include copper and brass alloys. Some higher strength plastics such as Polyetheretherketone (PEEK) and a variety of nylons provide strength and dimensional stability sufficient for ballistic applications.

The 10° half-angle cones used here are machined from 353 brass. Brass possesses high strength and is relatively soft having between 60-80 Rockwell B when compared to the hardened steel material that the barrel is made from with 103-107 Rockwell B hardness. Machining of the 10° half-angle cone of interest is performed using a Haas ST-20 computer numerical control (CNC) 3-axis lathe. The G-Code for the Haas ST-20 lathe can be found in Appendix A.2. The projectiles are machined to have a driving band with a diameter of 12.95 mm and height of 4.57 mm. The diameter of the driving band is greater than the gun barrel's 12.65 mm minor groove diameter. As a result, the projectile is loaded into the barrel so that the driving band is engaged with the minor diameter of the rifling. Figure 2.3 schematically displays the conical projectiles.

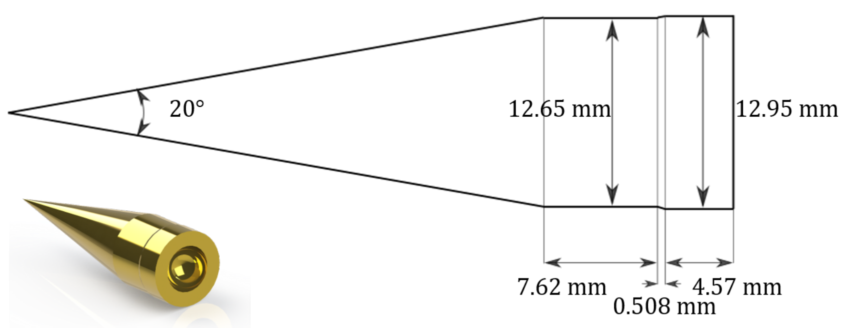

Figure 2.3: Cross-section of the cones launched from the PDGS

Significant plastic deformation occurs to the driving band from the ballistic launch of the projectile. The barrel rifling forms the driving band to the greater diameter of the grooves. The driving band and associated engraving process provides the gas seal between the projectile and the barrel [24]. The major diameter is the same for these conical projectiles as that used in standard match ammunition from Hornady [18]. The 0.50″-caliber gun barrel contains slightly more than 1 turn which rotates the projectile to a very high rotational velocity. The high rotational velocities allow the projectile to overcome the instability induced by the relative locations of center of mass and center of aerodynamic pressure. The center of mass is located behind the center of aerodynamic pressure for these projectiles meaning that a restorative aerodynamic force is not generated by the center of mass to right the body. The stability is only obtained through the angular momentum imparted by the rifling onto the projectile. Gun and projectile geometry lead to the desired internal ballistic performance.

Each projectile is measured and weighed before ballistic launch. This ensures that the dimensions are appropriate for the gun barrel and the mass is within an acceptable range of the mass used for internal ballistic modeling. The weighing operation is performed on a Fisher Scientific Model S-110 analytical balance. Masses of the projectiles are within ± 0.1 g of one another. The Haas ST-20 CNC lathe returns parts with a variance of 0.002g and average mass of 25.3 g. The internal ballistic modeling codes such as IBHVG2 to be described in the next section, accept a mass of the projectile to be used for calculation of relevant ballistic parameters.

2.1.2 IBHVG2 Model

Internal Ballistics of High Velocity Guns version 2 (IBHVG2) is a lumped-parameter ballistics modeling code designed to provide predictions of internal ballistics. The internal ballistics results can be used to select an appropriate charge mass of gun propellant for a desired ballistic performance [25]. The model provides accurate predictions of ballistic performance and details useful for designing projectiles. Of interest in the output parameters from the model are the predicted muzzle velocity and the maximum pressures developed at the base of the projectile and the breech. Material considerations for engagement with the rifling in the gun barrel and for strength of material to base pressures dictate the material which projectiles are machined from. IBHVG2 allows for selection of specific smokeless black powders and includes information on the deflagration through grain size, amount of powder, backpressure due to friction, and overall gun barrel geometry.

The relative burn rates of each Improved Military Rifle (IMR) powder are provided by the manufacturer and can be used to select the powder for appropriate ballistic performance [26]. IMR7828 is a slow burning powder which is favorable for high caliber weapons firing heavy projectiles. The deflagration of the powder is designed such that timescale is longer allowing a projectile to have the force from the deflagration act on it for a longer amount of time. As the projectiles fired are machined to a 0.50″-caliber specification, and weigh on average 25.3g, a slow burning powder which will impart a propulsion force for longer is necessary to overcome the inertial and frictional forces of the bullet during launch. Similar slow burning powders are used in commercial 50BMG match ammunition from Hornady [18]. Commercial No. 35 50BMG primers manufactured by CCI are used to initiate the IMR7828 for all tests.

One input to IBHVG2 of particular interest is the friction table. The friction table is input to the model as a pressure value for varying fractions of the length along the gun barrel. Adjustment of the friction table allows for a tuning of the completeness of the deflagration of the gun propellant. The twist rate of the gun barrel, and the dynamic friction between the bullet material and gun barrel influence this pressure as discussed by Wu et. al [27]. The completeness of the deflagration determines backpressure and muzzle velocity of projectiles. Values for the friction table can be determined experimentally through pressure tapped barrels [23], or modeled and iterated on as an adiabatic process of gas expansion governed by the ideal gas law.

Pressure measurements on the barrel were not taken during the test series, so an iterative approach under the assumptions of an adiabatic ideal gas expansion process is taken to adjust the IBHVG2 model input friction table. An adiabatic gas expansion is recast as a function of initial pressure, ratio of specific heats and the volume. The ratio of specific heats for gun propellant is provided as: $\gamma = 1.25$. The adiabatic gas expansion is started with a base pressure obtained from IBHVG2 for the known friction table of a smooth-bore gun barrel. The IBHVG2 model predictions for the internal ballistics using smooth-bore values is displayed on the "No Tuning" row of Table 2.1. The model inputs for the friction table are adjusted until the experimentally measured muzzle velocity of the projectiles is obtained from the model.

Table 2.1: Predicted gun performance using known backpressure method for smooth-bore barrels

	Breech Pressure	Base Pressure	Predicted Velocity	Measured Velocity	Percent Difference
	(MPa)	(MPa)	(m/s)	(m/s)	(%)
No Tuning	38	23	515	715	-28.0
Tuned Model	169	154	675	715	-5.6

As the projectile moves through the gun barrel, the volume of the barrel increases and therefore the pressure in the barrel decreases according to:

$$\frac{P_2}{P_1} = \left(\frac{V_1}{V_2}\right)^{\gamma} \tag{2.2}$$

where γ is the ratio of specific heats for product gases (taken as 1.25), V is the volume, and P is the pressure. State 1 is the initial volume and pressure of the case, and state 2 is obtained as a function of length the bullet has traveled along the barrel.

A simple MATLAB script was written to plot and predict the pressure at varying points along the gun barrel based on the adiabatic gas expansion. The IBHVG2 model is run for the initial base pressure generated for the projectile and charge mass of interest. The distances and pressures along the barrel where the backpressure is input into the model are shown in Table 2.2 from the neck of the gun barrel.

Figure 2.4 is a flow-chart that displays the process followed to adjust the friction table. The iterative calculation of the backpressure in the gun barrel as an

Table 2.2: Input friction table to IBHVG2 modeling code. Change in pressure between smooth-bore and tuned pressure displayed as a function of distance along gun barrel

	Position in Barrel (cm)			
	0	0.254	2.54	82.4
Original Backpressure (MPa)	4.14	6.21	3.45	2.07
Tuned Backpressure (MPa)	34.5	34.4	34.0	23.7

assumed adiabatic gas expansion results in the gun parameters displayed on the "Tuned Model" row of Table 2.1 which are observed when using the IMR 7828 smokeless black powder and the 353 brass 10° half-angle cone projectile.

A charge mass of 9.07 g (140.0 grains) of IMR 7828 powder results in a muzzle velocity of approximately 715 m/s which is approximately Mach 2. The IBHVG2 model adjustments to the friction table predict that the base pressure on the projectile is approximately 150 MPa. This pressure applied to the bullet is not greater than the quasi-static yield strength of the 353 brass material (170 MPa), and as such the material is predicted to survive the ballistic launch. As the cones travel downrange they trigger the high-speed quantitative schlieren imaging system. Figure 2.5 displays a still from the PDGS firing one of the conical projectiles at approximately Mach 2.

2.2 Quantitative Lens Based Schlieren

The schlieren system employed for the analysis of the quantitative density fields around the projectiles is a lens type schlieren system, as shown schematically in Figure 1.1. The schlieren system allows for the visualization of gradients of density orthogonal to the orientation of the knife edge in the schematic. The schlieren effect is obtained as a result of refracted light interacting with the knife edge. Each element in the system acts to direct light to a point which is where the cutoff is placed.

The illumination source is a Specialised Imaging SI-LUX 640 spoiled coherence laser. The Specialised Imaging SI-LUX 640 allows for pulsed spoiled coherent 640 nm laser illumination down to 10 ns individual pulses. The SI-LUX has a laser safety unit and a timing box used for triggering. Each box requires various

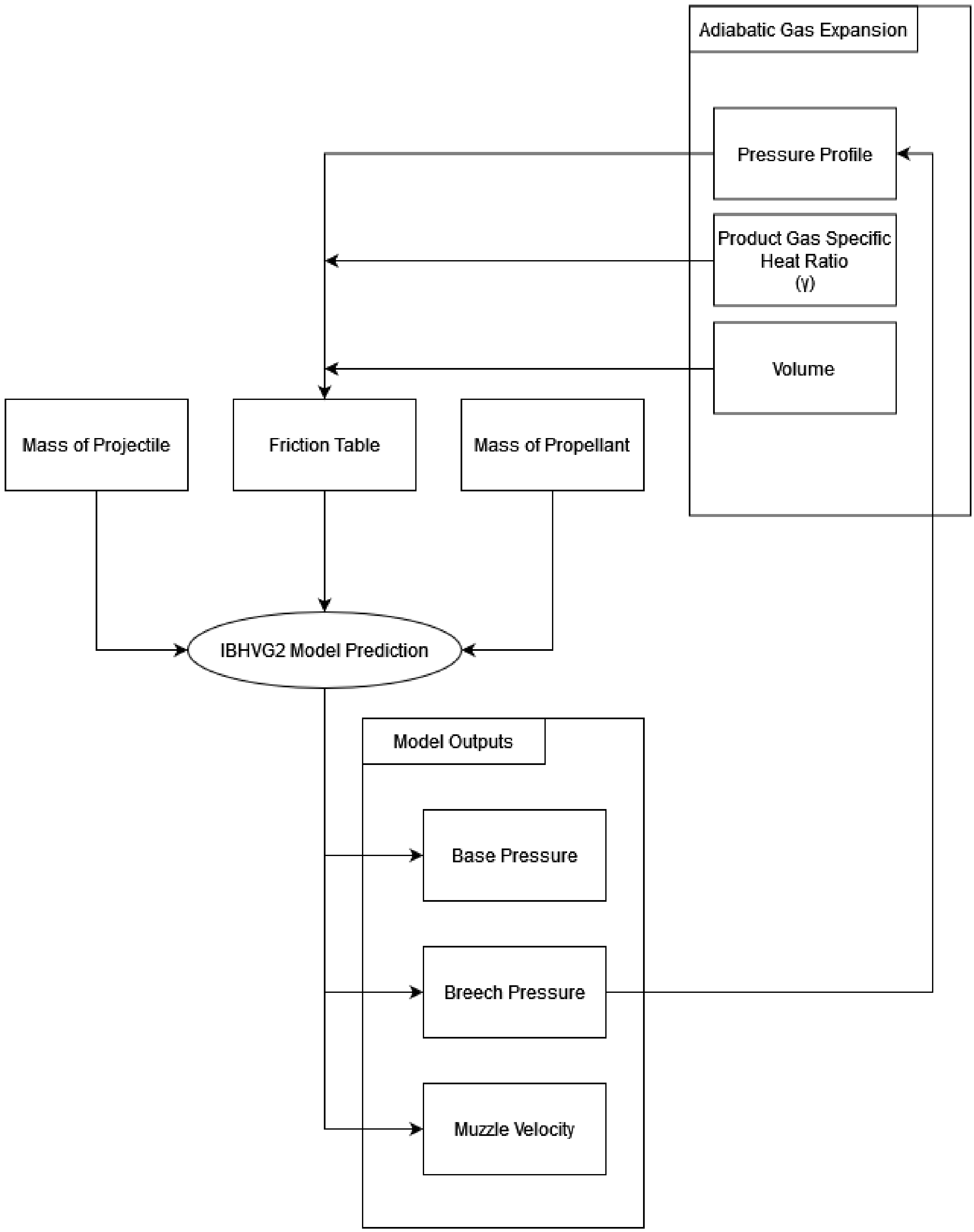

Figure 2.4: Flow chart outlining the iterative approach for prediction of backpressure for conical projectiles via IBHVG2

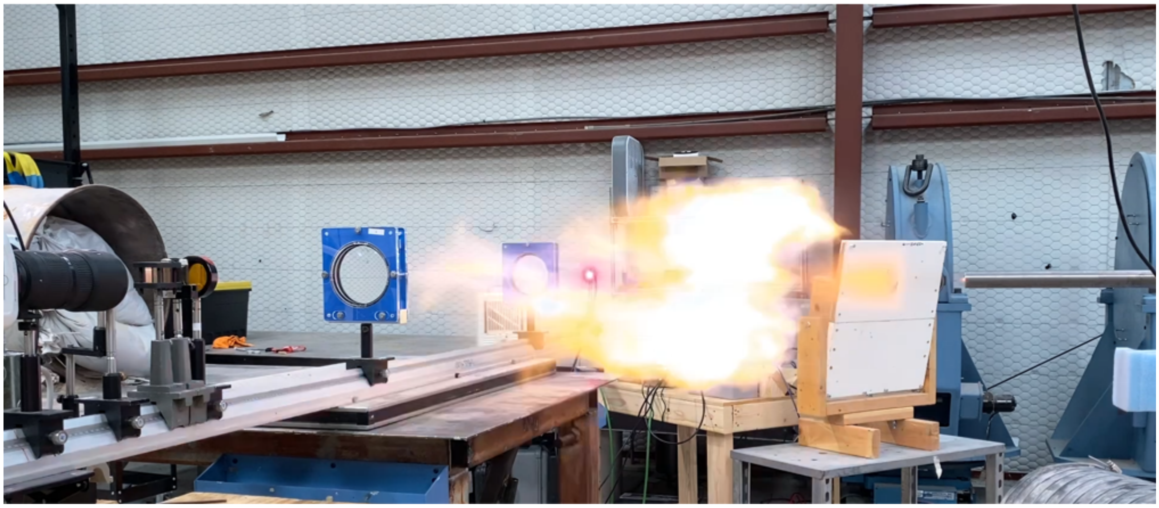

Figure 2.5: PDGS firing conical projectile with SI-LUX pulsed laser illumination source visible

signals and states to be met such that the laser illumination source is allowed to fire at its 380 W of power. The system allows for a total on time of 30 μs separated by a given delay after a signal pulse is sent. Each pulse of the laser illumination can be selected in total time width $\leq$ 30 μs. Further detail on the operations of the SI-LUX system can be found in Appendix C. The illumination source is sent through a liquid light guide which is placed in line with the center-line of the schlieren optics. The light output from the liquid light guide is arranged such that uniform intensity is achieved across the entire face of the 5 mm diameter liquid light guide. A smaller point source of light is needed for the best collimation of light in the schlieren test section. The light from the liquid light guide thus is allowed to expand, and is recollected using condensing optics.

The condensing optics consist of both an aspheric plano convex lens and an iris diaphragm. The condensing lens is a 75-mm-diameter, 40-mm-focal-length aspheric lens. The center-line of the asphere is aligned with the center-line of the liquid light guide, and is placed approximately 15-20 cm away from the liquid light guide. The aspheric lens is placed with the spherical side facing away from the incoming light. The geometric optics of the aspheric lens will converge light to a focal point at one focal length away from the lens. The aspheric lens has a focal length of 40 mm and converges light to a focal point this distance away from the lens. An iris diaphragm is used to further reduce this point size of the light. The iris diaphragm is also aligned with the center-line of the focal point. Care must be taken to ensure that the aspheric lens is not rotated and that all of the light travels from the focal point which has been reduced in size by the iris diaphragm. The iris diaphragm is located one focal length from the schlieren lenses.

The schlieren lenses are f/5.5-127-mm-diameter, 700-mm-focal-length achromatic doublets. The schlieren lenses are centered with the iris diaphragm and located at the 700 mm focal length down from the iris. The light expands from the idealized point source and when the light reaches the first schlieren lens the light rays within the diameter of the lens will travel parallel. If placed correctly, the first schlieren lens will project purely parallel light until recollected. At any arbitrary distance from the schlieren lens, another achromatic doublet is placed in the opposite orientation to recollect the light. Any change in species or refracted light will be seen from this type of system as a change in intensity of light. This is the focused shadowgraph system. If any refractive disturbance is present in the test section between the two achromatic doublets this light will not converge to the same point. At the focal point, the light can be interacted with to visualize different gradients of the flow phenomena [3].

At the focal point where the light converges back to a point, a simple mask is placed to create the schlieren effect. The schlieren effect is a result of the separate gas species within the test section or refractions of light which result in the light being bent into or away from the mask. The testing utilized here implements a simple cutoff mask in the form of a razor blade. The razor blade is positioned on a filter holder at the focal point of the converged light. The refractions result in a perceived change in local refractive index which causes the image after the focal point to have a light to dark variation in intensity which is ultimately related with refractive angles ε_y orthogonal to the cutoff. The amount of cutoff, focal point size, and schlieren lens selection all contribute to the overall system sensitivity [3]. Additional optics are sometimes required when performing schlieren measurements to obtain desired images or specific cutoffs. These optics are only necessary for certain testing conditions.

2.2.1 Optional Optical Components

In order to simultaneously collect horizontal and vertical knife edge images, 50/50 transmission-reflection non-polarizing beam-splitter cube is placed before the knife edge location to split the light into two optical paths. The cube beam-splitter turns 50% of an incident beam 90° while allowing for the other 50% of the beam to transmit through the optic. The cube beam-splitter is an additional optic that is only required if a multi-view schlieren system is desired. Here two different knife edge orientations are used to measure the vector refraction angle in some tests. Both 25 mm and 50 mm cube beam-splitters are used here to observe orthogonal refractions. A cube beam-splitter will reduce the light that is observed at each camera. An increase to the pulse width of light from the SI-LUX is sometimes required. If too much light is received at each camera, neutral density filters must be introduced.

Neutral density filters are used to decrease the overall intensity of light that passes through them. Tests using a multi-view system typically do not require the neutral density filters as the pulse width of the SI-LUX is adjusted to obtain sufficient intensity reaching the camera sensors. If the camera sensors are receiving too much light after reducing the intensity of the SI-LUX down to 10 ns, neutral density filters can be used to reduce the amount of light reaching the camera sensors. The neutral density filters have varying optical densities used to attenuate light through uniform absorption of light.

A 640 nm imaging quality bandpass filter is used to filter out all light without the specific wavelength λ=640nm. For the SI-LUX laser illumination source, a bandpass which allows 640 nm light to pass through and removes all light within a $\pm 10\%$ band above and below the 640 nm can be used. As these tests do not emit their own illumination from combustion or other sources, there is no need for a bandpass filter. Some tests utilized a bandpass filter, but the filter simply adds another absorbing optic. With the correct amount and wavelength of light reaching and being masked at the focal point, a high-speed camera is placed after the knife-edge.

2.2.2 High-speed Imaging

Phantom V711 or VEO4K 990S high-speed cameras were used to collect schlieren images here. High-speed imaging is utilized due to the required precision of timing when recording flow phenomena of the projectiles as they pass through the schlieren system at a supersonic velocity. The high-speed cameras have the ability to output a 5V TTL signal immediately on the opening of the shutter, which is used to trigger the pulsed laser illumination source.

Since the supersonic cones are not self-luminous, the exposure time on the high speed camera is not of concern because the exposure is controlled by the SI-LUX light pulse. The exposure time on the high speed camera is typically set at a time of 5 μs. The SI-LUX 640 laser illumination source allows for an equivalent exposure on the order of 10's to 100's of nanoseconds when using these specific high-speed cameras. The pulsed illumination freezes all motion seen in the images by only illuminating the projectile in the schlieren test section for a fraction of the time that the high-speed camera's shutter is open. The SI-LUX has a limitation on the duty cycle and amount of on-time that the laser can support. A maximum on-time of 30 μs cannot be exceeded with the laser. A +5V TTL shutter open pulse from the high-speed camera is sent to the Specialised Imaging delay generator box. The delay generator box sends a pulse to the imaging laser to pulse with a given width input to Specialised Imaging's SI-LUX software. Further specifics on the laser operations can be found in Appendix C. The light received at each camera exposes the pixels being sampled for the test.

High-speed camera architecture allows for faster frame-rates at reduced resolution with most common speeds of 5,000-15,000 frames per second (fps) at the total resolution. The Phantom V711 can record at 7500 fps at a 16:10 aspect ratio 1 megapixel sensor (1280x800 pixels). The Phantom VEO 990S can record at 900 fps at a 16:9 aspect ratio 9.4 megapixel sensor (4096x2304 pixels). Each camera is used at differing frame-rates and for differing applications. Multiple resolutions provide insight into the requirements and relative accuracy of the reconstructed density field through the calibration process. If a greater pixel resolution camera is used in the schlieren system, the continuum of flow around the cone is discretized into smaller physical regions.

2.2.3 Refractive Calibration

The schlieren images recorded of the supersonic projectiles are arrays of intensities at discretized points in space. A relationship between the array of intensities is necessary for a quantitative measure of the flow field imaged. A calibration process wherein a long focal length, small format lens is placed in the schlieren system to calibrate the raw intensities seen at the camera sensor with known refractive angles is used [10]. A calibration image is taken of a simple plano-convex lens from CVI Laser Optics with focal length of 10m. The 10m focal length lens radially refracts light from the edges of the lens to the center of the lens. As schlieren images are directional based on the orientation of the knife edge, a projection of the gradient is seen in the lens orthogonal to the razor blade rather than the whole radial gradient. In horizontal knife edge images, the lens appears with a vertical gradient in it. The un-refracted light at the center of the lens ideally appears as the average background intensity. Light rays bent into the knife edge appear as dark regions in the image. Likewise, light rays bent away from the knife edge appear as light regions in the image. As the focal length of the lens is known, a theoretical profile for the refraction can be developed through the thin lens equation [28]. The thin lens equation for the change in refractive angle ($\delta_{i,j}$) is given by:

$$\varepsilon = tan^{-1}\left(\frac{(I-\bar{I})p}{f}\right) \tag{2.3}$$

where: I is the intensity at a given location, $\bar{I}$ is the average background intensity not including the lens in frame, p is the size of each pixel in the projected image, and f is the focal length of the lens.

The value of ε is a radian valued quantity. The change in refractive angle must be obtained through the value p which is a physical pixel to distance calibration. The physical pixel to distance calibration is performed using the Circular Hough Transform (CHT) to identify the most statistically likely circle within an image as discussed by Atherton and Kerbyson [29]. Since the holder for the calibration lens is circular in shape and takes up a large portion of the field of view it is used as a spatial calibration target. For the parallel light present in schlieren imaging, all pixels are projected onto the camera sensor as the same physical size. Simply identifying the diameter of the lens case and dividing the physical size by the number of pixels results in the value (p) as shown by:

$$p = \frac{d}{d_{CHT}} \tag{2.4}$$

where: d is the physically measured diameter of the lens case, and d_{CHT} is the diameter of the lens holder in pixels identified by the CHT algorithm.

With a known relationship between the intensities and the refractive field, the sensitivity of the system is the limiting factor for reconstruction of flow phenomena. The sensitivity is a function of the bit depth of the camera sensor, the amount of cutoff, the point source size of light, and the selected calibration lens [3]. The longer focal length of the lens, the weaker the refractive disturbance and therefore the greater the sensitivity [30].

2.3 Focus Sensitivity to Point Source Size

A side-by-side comparison between the schlieren images with and without the condensing optics was performed. Figure 2.6 shows the comparison of images obtained with and without condensing optics.

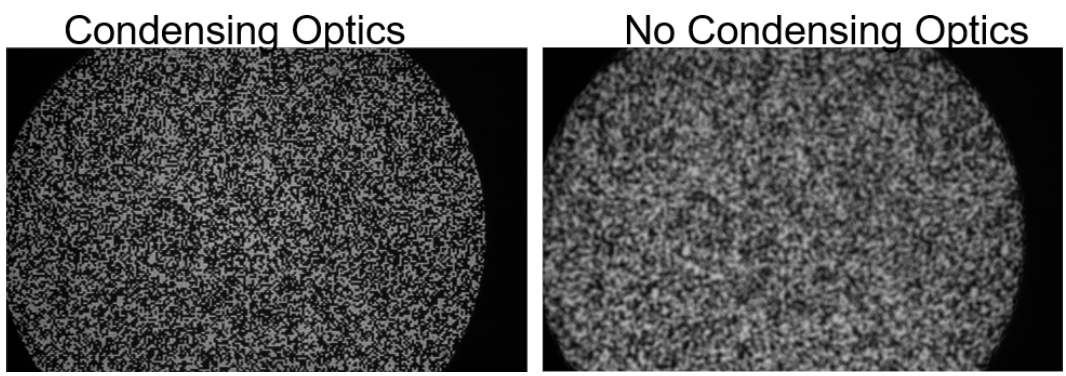

Figure 2.6: left: Image obtained with condensing optics with t/L of 0.9. right: Image obtained without condensing optics with t/L of 0.9

Both schlieren and BOS focusing are largely dependent on the size of the light source being small. The limit case of a pinhole camera corresponds to large aperture stops nearing f/500 [28]. The case of a 5 mm point source of light (like the liquid light guide alone) has an effective aperture of f/25.4, creating a small effective aperture, but not generating purely parallel light in the test section. The focus limitations are also a function of effective initial aperture. When the aperture nears f/160 for the minimum aperture for the iris diaphragm, the depth of field is wider resulting in better schlieren and BOS reconstructions. The differences between using the purely parallel light and an extended light source are discussed further in Settles [3]. With the depth of field being widened by decreasing the initial point source of light, the effects of depth can be evaluated using Background Oriented Schlieren.

2.4 Parallel Light Background Oriented Schlieren Methodology

Background Oriented Schlieren (BOS) allows for creation of schlieren-like pictures from two high contrast images and image registration post-processing techniques [9]. Typically, a simpler testing setup is obtained when using BOS as there is no requirement for sensitive optical arrangements. A comparison between BOS and traditional schlieren for imaged refractive angles is discussed in Fisher et. al. [21]. A new BOS methodology is proposed here which leverages the same testing setup as the schlieren system without a knife edge similar to a focused shadowgraph setup as discussed in Section 1.2.2. A transparency with a black and white BOS random dot pattern printed on it is placed within the test section of the focused shadowgraph setup at a known location to act as the BOS background. The high contrast image displayed on Figure 2.6 is from the BOS test setup.

Only a single camera is necessary for the BOS testing. The other change from the setup discussed in Section 2.2 is the removal of the knife-edge at the focal point. The same imaging laser, condensing optics, schlieren lenses and camera placement are valid for the parallel light BOS testing. The BOS background speckle pattern's position relative to the schlieren object allows for the measurement of refractive angles. BOS relies on a post-processing algorithm to determine apparent displacement between the cold "flow-off" image and a hot "flow on" image. Multiple algorithms for this post processing exist [9], but Digital Image Correlation (DIC) is the post processing method used here. DIC is used for measuring displacements in images with the intent of characterizing displacements and typically strain in solid samples [31]. In the BOS application, the displacement output initially used for strain can be related to a refractive angle (ε). The benefit of these two-dimensional correlation algorithms is that they directly provide orthogonal displacement fields. To achieve the same result with quantitative schlieren, two camera viewpoints are necessary for the fields ε_x and ε_y. Figure 2.7 displays an output from Correlated Solutions' VIC2D two-dimensional correlation algorithm for the u and v contours. The u and v contours are analogous to ε_x and ε_y, respectively. The sensitivity can be varied through the size of the correlation window used in the software, but is generally established by the BOS setup geometry [10].

DIC seeks to extract a window of a given size from the cold image and locate the same features in the hot image. An apparent shift between the location of distinct features is found by the algorithms. Typical individual features for correlation are recommended to be 3-5 pixels in size according to the International Digital Image Correlation Society [32]. The refractive conversion from the displacement is a trigonometric calculation. As discussed in Hargather and [10], the conversion from BOS displacement contours to refractive angles is defined by:

$$\frac{\text{pixel shift } p}{L - t} = \tan \varepsilon \tag{2.5}$$

where pixel shift is obtained from the u or v contour relating to the refractive

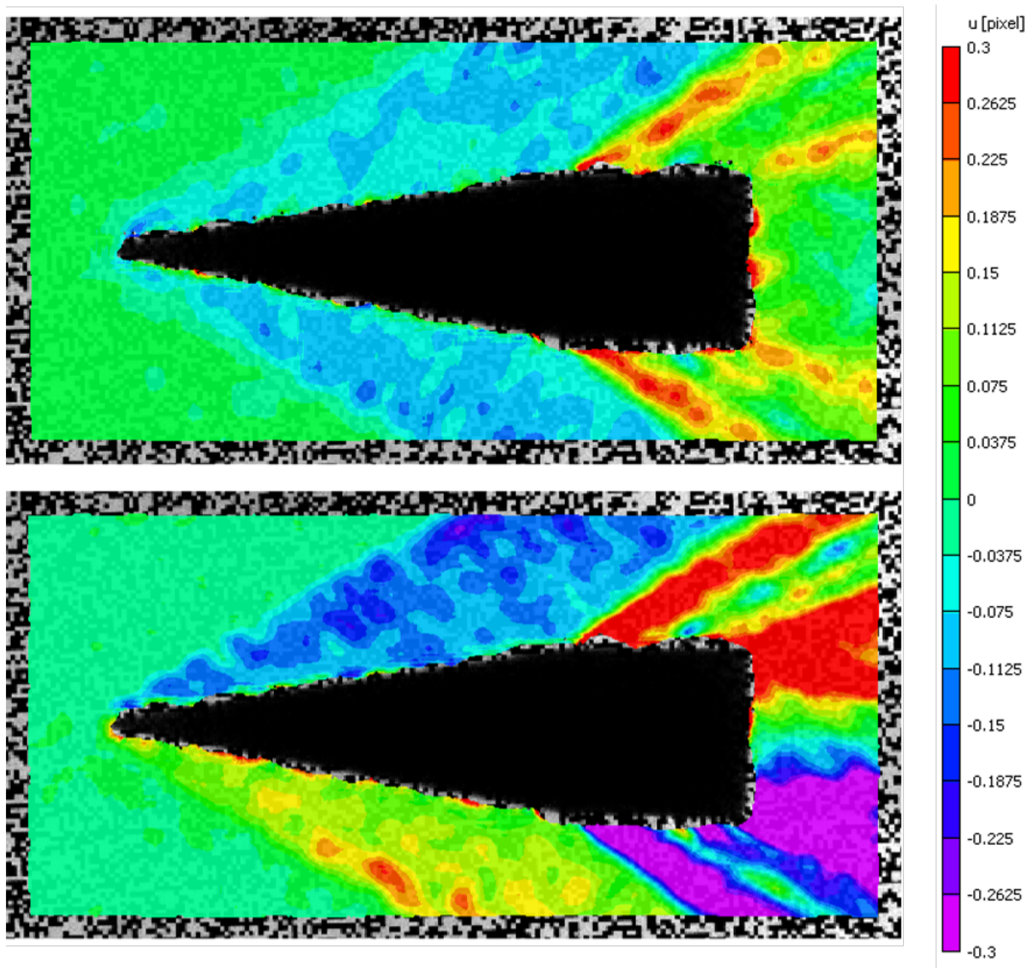

Figure 2.7: top: u contour (analogous to vertical knife edge schlieren). bottom: v contour (analogous to horizontal knife edge schlieren)

angles ε_x, or ε_y, respectively for the pixel shift contours, p is the physical pixel to distance calibration, L is the distance from the camera to the background, and t is the distance from the camera to the schlieren object.

The refractive angle is again a radian valued change between a flow off and a flow on image. The difference here is that the average background intensity is no longer necessary, but rather is already included in the contour. A similar calibration process to the refractive calibration discussed for the quantitative schlieren in Section 2.2.3 can be performed to validate the methodology. Further discussion and results on validation of the parallel light BOS methodology is included in Section 3.2.1. Both schlieren and BOS return a change in refractive angle which is the input to the three dimensional Abel inversion.

2.5 Abel Inversion

The schlieren imaging techniques capture the entire light bending along the optical path taken by each light ray. The three dimensional nature of conical flow results in the bending of a light ray over two discrete shocks and a continuously varying density field as the ray travels through the conical shock flow field. This means that an algorithm for projections must be applied to correctly deconvolute the integral and obtain the refractive index at each radial location in the schlieren images. A two point Abel deconvolution algorithm discussed by Kolhe and Agrawal [33] is used to correctly deconvolute this integral.

Multiple Abel inversion algorithms exist, each with varying applicability, but a two point algorithm discussed by Kolhe and Agrawal [33] and documented for schlieren by Biss [34] and Tobin [30] is used here. The input of the Abel inversion is a change in refractive angle between the background and the local radial point being inverted. The applicability of the method to the conical flow requires that the curvature of the oblique conical shock is negligible and that the property varies radially from an origin to the inversion location. The inversion origin is asserted to be the symmetry line of the field being imaged. For a cone, this is the center line of the cone. Locations at the surface of the cone which have either a zero or near-zero intensity are inverted, but are removed due to their non-physical reconstruction. The indices i and j are refractive δ's ranging from 1 to $N+1$, where N is the number of data points. The value of $D_{i,j}$ are the independent data spacing linear operator coefficients specific to the 2-point Abel inversion method [33]. A MATLAB code is written to perform the inversion returning $\delta(r_i)$ which is the change in refractive index at the specific radial location.

The Abel inversion's coefficient matrix $D_{i,j}$ relates the deflection of neighboring radial points with a diagonal dominance and is an upper triangular matrix [33]. The inversion moves inward along the radial position indicating that values inside the main diagonal affect the inversion progressively less when moving further radially inward. The inversion does not consider the points radially spaced beyond the current radial distance from the symmetry line. Equations 2.6-2.9 describe the formulation of the $D_{i,j}$ matrix and the inversion process.

$$\delta(r_i) = \sum_{j=i}^{N+1} D_{i,j} \cdot \varepsilon_j \tag{2.6}$$

$$D_{i,j} = \begin{cases} \frac{1}{\pi}\left(A_{i,j} - A_{i,j-1} - jB_{i,j} + (j-2)B_{i,j-1}\right), & if\ j > i\ and\ j \neq 2 \\ \frac{1}{\pi}\left(A_{i,j} - jB_{i,j} - 1\right), & if\ j > i\ and\ j = 2 \\ \frac{1}{\pi}\left(A_{i,j} - jB_{i,j}\right), & if\ j = i\ and\ i \neq 1 \\ 0, & if\ j = i = 1\ or\ j < i \end{cases} \tag{2.7}$$

$$A_{i,j} = \sqrt{j^2 - (i-1)^2} - \sqrt{(j-1)^2 - (i-1)^2} \tag{2.8}$$

$$B_{i,j} = \ln\left(\frac{j + \sqrt{j^2 - (i-1)^2}}{(i-1) + \sqrt{(j-1)^2 - (i-1)^2}}\right) \tag{2.9}$$

$$\delta(r_i) = \frac{n(r_i)}{n_0} - 1 \tag{2.10}$$

The output of the inverted field is the refractive index at a specific location. The Gladstone-Dale relation relates a material's refractive index with its local density. From the Abel inversion, the density of the air around the projectile can be obtained. The Gladstone-Dale constant for air is taken to be $k = 0.000226$ m^3/kg and although this value is wavelength dependent the change is negligible across the visible spectrum and is further discussed in Tobin [30].

CHAPTER 3

EXPERIMENTAL RESULTS

The application of the Abel inversion to the schlieren images of free-flight cones results in the conversion from the refractive angle field (ε) to a refractive index field (n). The Gladstone-Dale Law then relates the gas refractive index to density, which allows for the reconstruction of the density field around the projectile. Measurement of density variations in the gas around the projectile allow for insight into the stability and performance of ballistic bodies.

3.1 Quantitative Schlieren Reconstruction of Conical Flow

The density variation around the projectiles is calculated through the quantitative schlieren calibration process. The calibration process requires three total images for the analysis performed here. The three images are a background image, an image of the supersonic cone, and an image of the calibration lens. Theoretical density profiles are obtained from the Taylor-Maccoll conical flow relationships.

3.1.1 Image Pre-Conditioning

The image pre-conditioning performed here is a simple background subtraction to remove the influence of any defects on the camera lens, schlieren lenses, beamsplitter, neutral density filter(s), bandpass filter, condensing lens, and liquid light guide. Additionally, some additive Gaussian noise common with laser imaging or high-speed camera sensor gain is reduced. The background subtraction is a simple linear operation where the background image has the schlieren image of the cone subtracted off of it. This subtracted image is then subtracted from the average background intensity. The resultant image from this operation only differs from the cone image in its relative zero intensity value. The final operation involves subtracting the minimum intensity in the cone image to have the same intensity distribution between the background-subtracted image and the original cone image.

Non-linear adjustments to the images are not appropriate since intensity variations are directly proportional to the density changes in the air around the projectile. As a result, intensity adjustments are only linear additions or subtractions to obtain the same overall background intensity. The zero refraction intensity value which is the average background intensity is set to the local density (ρ_1) calculated during the time of the test from recorded atmospheric properties.

A simple binary mask is applied to the cone image so that any refractive disturbance is not included in the determination of the average background intensity for the schlieren image of the cone. A MATLAB script is written utilizing the built-in MATLAB function “graythresh” to identify the background from the foreground [35]. This MATLAB function is an implementation of Otsu’s ideal thresholding algorithm for a grayscale image [36]. The Otsu threshold provides the most statistically likely intensity level within a grayscale image that maximizes the variance between the classes assigned to the background and foreground of the image. This level is used alongside the built-in MATLAB function ”im2bw” to develop a mask which will remove areas of the image that are not considered in the average background intensity. The mask was applied onto the cone image and the non-zero intensity values within the masked image are averaged to obtain the average background intensity for the cone.

A similar method is applied to the calibration image to determine the average background intensity. Before thresholding this image, the MATLAB function “imfill” was utilized to fill regions of the image that are the calibration lens. This operation fills the entirety of the lens with zero intensity values. The returned image is thresholded utilizing “graythesh” and “im2bw” to identify regions where the average background is the only intensity value present. The average of the non-zero intensity values was taken for the calibration image and compared with the average background intensity of the cone image. If there was any difference between these two values, the difference was added to or subtracted from the cone image.

3.1.2 Schlieren Calibration and Abel Deconvolution

The pixel intensity-position calibration is performed on the calibration image taken of a 10-m-focal-length plao-convex lens. The intensities in the calibration lens are extracted and a linear regression of pixel intensity versus pixel location was performed. MATLAB’s built-in curve fitting functions “polyfit” and “polyval” were used to relate position with intensity. Figure 3.1 displays the quantitative regression relating the pre-processed pixel intensities with their pixel locations. A linear fit is consistent with other quantitative schlieren implementations like those discussed in Tobin [37].

The polynomial coefficients from the pixel location and pixel intensity regression is saved for future reference in an input file to be used by the quantitative schlieren imaging code. Additional inputs to the quantitative schlieren imaging code include the average background intensity, the local atmospheric density, and the locations about which to invert. A symmetry line must be selected for the schlieren inversion about which the field is assumed to be radially

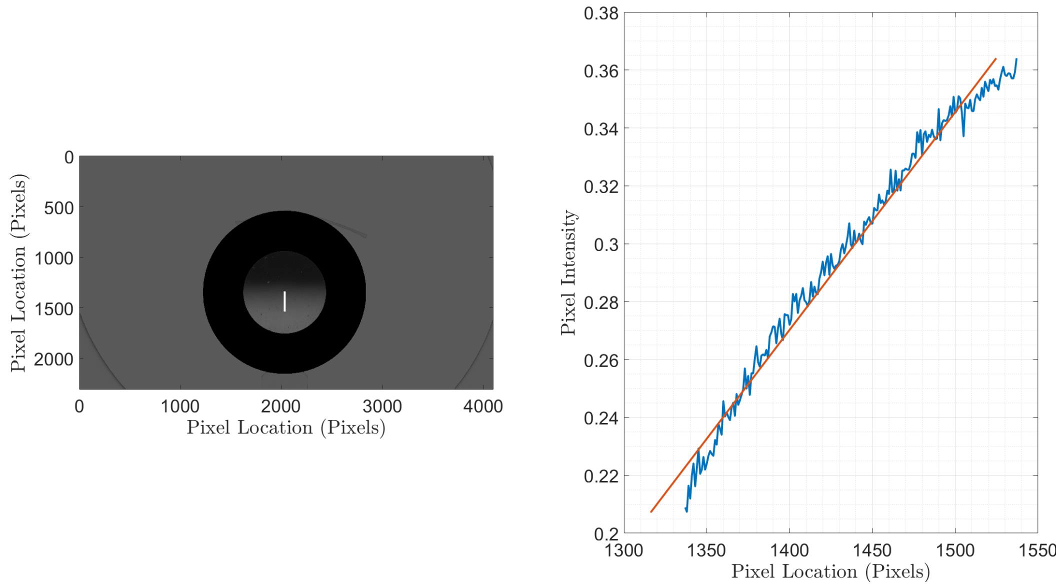

Figure 3.1: (left) Post-Processed schlieren calibration image with pixels extracted along the white line. (right) Linear regression of pixel intensity versus pixel location

symmetric. In the case of the cones, the center-line of the cone is the symmetry line. The quantitative schlieren imaging code requires that the inversion be performed moving from the outer-most radial position of the path integrated radial field to the center of the field. Figure 3.2 displays the horizontal symmetry line that exists for the conical projectiles.

The linear coefficient matrix ($D_{i,j}$) in the Abel inversion is formed based on the length of vector being inverted. The inversion is performed to include only regions within the particular column of the image that display the radial symmetry. The oblique conical shock wave is inclined at an angle (θ), so the length of the vector to be inverted is a function of position along the cone. The deflection at the farthest radial position for the D matrix is a single free-stream pixel and the shock wave boundary is also input to the inversion.

A MATLAB script was written to identify the locations for each column of the image to be inverted. The oblique conical shock wave is treated as a line segment with one endpoint at the apex of the cone and the other inclined at the wave angle (θ). The apex of the cone is identified within the velocity tracking code via the built-in MATLAB function “regionprops”. The bounding box return from this function provides details of both the centroid, length, and width of the rectangle that the cone outline fits within. The final pixel location for the apex is defined by:

$$A_x = G_x - \frac{w}{2} \tag{3.1}$$

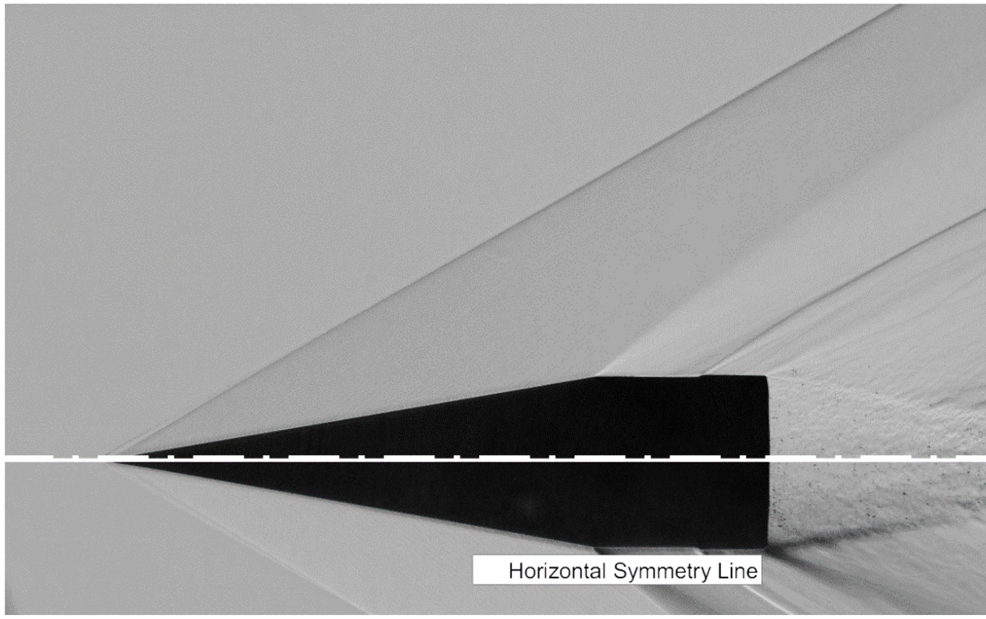

Figure 3.2: Symmetry line assumed for quantitative schlieren calculation

$$A_y = G_y \tag{3.2}$$

where $A_{x,y}$ is the x,y value pair of the location of the cone apex, $G_{x,y}$ is the location of the centroid returned from MATLAB's regionprops, and w is the length of the bounding box returned by the "regionprops" function

The other endpoint of the wave angle for inversion is determined from an additional MATLAB code which prompts the user to identify the endpoint of the oblique conical shock wave. From this identified location, a linear least squares regression is performed between the two endpoints. The (x,y) value pairs are rounded since intensity values are only obtained for discrete locations on the image array. Each column of data now has a specific height such that the Abel function can generate the correct D matrix for the current column of quantitative data.

The input to the Abel inversion is ε which is the change in refractive angle between the background intensity and the current pixel being inverted. This refractive angle is obtained through the pixel location and intensity relation developed from the calibration image and the average background intensity's position in the lens ($\bar{I}$). This change in refractive angle is input to the Abel inversion as defined by:

$$\varepsilon \; = \; tan^{-1}\left(\frac{(I-\bar{I})p}{f}\right) \tag{3.3}$$

where I is the location within the calibration lens that the intensity corresponds with, p is the pixel spacing obtained from the spatial calibration, and f is the calibration lens' focal length.

The output of the Abel inversion is the quantity $\delta(r_i)$ which is proportional to the refractive index at the current radial position. This refractive index is defined by Equation 2.10.

The Gladstone-Dale law can be applied to calculate the density since the value of k is well known for the illumination wavelength $\lambda = 640$nm. It has been shown that the constant k varies non-negligibly in the IR spectrum as discussed further in Settles [3]. From the density output of each column in the image, a composite of each inverted row is assembled into a matrix. One final masking operation is performed to remove the erroneous reconstructed density values from the intensities of the cone itself. The 353 brass is opaque, so the projection in the schlieren image should be zero, but a non-zero intensity value is typically recorded by the camera due to noise on the sensor or as a result of image preprocessing.

The binary mask is a black and white image obtained from Otsu's ideal thresholding algorithm discussed in Section 3.1.1. The thresholding algorithm follows the same procedure discussed for obtaining the average background intensity. This mask was stored as an array that is the size of the image. This masking array was saved out and applied to remove erroneous reconstructed densities. MATLAB's element-wise multiplication for arrays was used for the masking operation. Figure 3.3 displays a binary mask of the cone applied onto the density reconstruction. The density field is overlain onto the pre-processed schlieren image as a contour overlay.

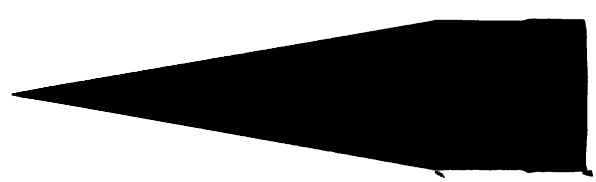

Figure 3.3: Sample binary mask for removing erroneously reconstructed density values

MATLAB's built-in contour overlay tools allow for visualization of property variation using a sliding color-scale. The standard colormap "jet" is used to visualize the density variation. A contour density overlay is displayed on Figure

3.4. As the Taylor-Maccoll conical flow solution would predict, a visible increase to the density can be seen moving from the free-stream to the cone surface. Since the assumptions of Taylor and Maccoll have been met, a comparison with the theoretical density profile can be performed.

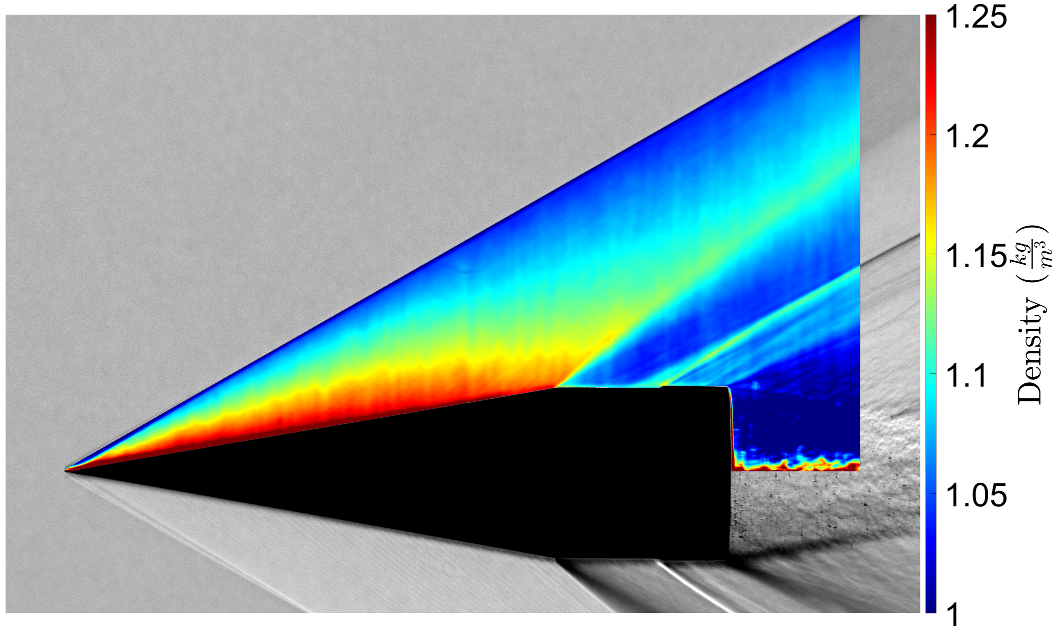

Figure 3.4: Quantitative contour overlay of schlieren image for density profile

3.2 Background Oriented Schlieren Reconstruction of Conical Flow

Post processing of the Background Oriented Schlieren measurement of the cones takes a slightly different approach to obtain a qualitative density contour overlay. The BOS images are taken using the high-seed camera and then post-processed using a commercially available correlation software. The correlation software used here is Correlated Solutions' VIC2D. The parallel light test setup for BOS is different from traditional BOS measurements, so a laboratory scale test series was performed first to ensure that the methodology can be used for quantitative schlieren reconstructions. The input to all quantitative schlieren measurements is a change in refractive angle, so ensuring that the parallel light BOS method can record and calculate a refractive angle needed to be performed.

3.2.1 Laboratory Scale BOS Validation

The quantitative BOS reconstruction relies on the setup discussed in Section 2.4. To the author's knowledge, BOS performed in parallel light has not been previously published, nor has it been used for quantitative measurements. A series of experiments were thus performed to ensure that a refractive angle field ($\varepsilon_{i,j}$) can be obtained through the parallel light BOS methodology. A quantitative schlieren calibration lens was used to perform this validation testing.

A simple weak plano-convex lens is used to baseline the methodology against a known refraction in the test section. A similar type of validation testing was performed for rainbow schlieren by Stricker et al. [6]. Both horizontal and vertical refractions are obtained in the test section proportional to the u and v pixel shifts measured through Digital Image Correlation (DIC) processing. Geometric optics theory for the lens provides the expected refraction to be measured. The assumptions of geometric optics allow for determination of the refractive angle (ε) simply from the radial position in the lens. Identifying the center of the lens in the image and the pixel spacing are the only required measurements to determine a theoretical refractive angle field (ε).

The MATLAB function "imfindcircles" is an implementation of the Circular Hough Transform (CHT) and and has been used extensively for spatial calibrations in the quantitative schlieren process. The CHT is sensitive to noise and high contrast regions within images. This results in the spatial calibration being more challenging to perform due to the high contrast in the images required to perform BOS measurements. Atherton and Kerbyson discuss the CHT algorithm's robustness to additive zero mean Gaussian noise for a series of position detections in images [29]. The algorithm is robust up to approximately 10^4 level variance zero-mean Gaussian noise, but becomes decreasingly accurate as the noise continues increasing. The BOS background placed in the test section exceeds this noise threshold for accurate position detection. A morphological image processing methodology was developed to ensure that the lens center and radius were identified correctly throughout the entire test series. The morphological image processing used for the spatial calibration was performed across 21 images per test set and the average spatial calibration value and lens center found. The lens center and the lens holder center are assumed to be the same value. Figure 3.5 displays the identified circle comparison between the the most in focus image and the least in focus image obtained by the morphological image processing.

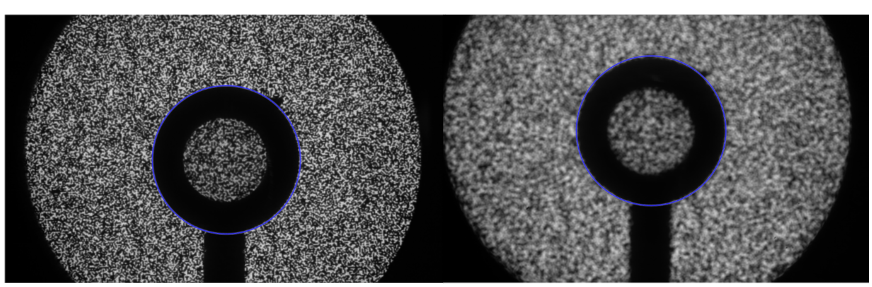

Figure 3.5: (left) crisp focused image with outline of circle identified through CHT. (right) Out of focus image with pre-processed surrogate image CHT algorithm applied for calibration

A series of surrogate images are calculated to correctly identify the spatial calibration value through the CHT for various focus characteristics. The image processing utilizes a zero image used as the "hot" image for post-processing and background subtracts it from the lens image. This background subtraction follows the same algorithm as that used for quantitative traditional schlieren measurements as discussed in Section 3.1.1. The background-subtracted image is thresholded utilizing Otsu's ideal thresholding algorithm. This thresholded image is a black and white image used as a mask applied onto the background subtracted image. The image obtained after the masking and thresholding operation has the morphological image processing transformation of a tophat applied to isolate the lens case in the image. An overview of the tophat morphological image processing algorithm is discussed further in Gonzalez and Woods [38]. The structural element used for the tophat image transform is a large diameter disk which highlights the lens holder in frame. This image is thresholded once again utilizing Otsu's method, and then the CHT is applied to the black and white image to identify the lens case in the image. This methodology returns consistent spatial calibration values through all testing performed. With the center and spatial calibration determined, the theoretical refractive profile is found through geometric optics assumptions.

The distance from the center-line of the lens is used to generate the theoretical refractive profile. From this calculation, the theoretical refractive angle from the calibration lens is obtained simply from the pixel spacing and the center of the lens as defined by:

$$\varepsilon = \tan^{-1}\left(\frac{\text{spatial pixel location}}{\text{lens focal length}}\right) \tag{3.4}$$

The refraction within the test section varies linearly under the thin lens approximation. As a result, a comparison between the slope of the refraction obtained through DIC and geometric optics is appropriate for validation of the parallel light BOS methodology.

Tests were performed in which a BOS background was printed on a transparency using a Brother MFC-L2710dw printer with a dpi of 2400 x 600. The BOS background printed on the transparency is mounted between filter holders on an optical mount placed on optical rails with millimeter accuracy. The BOS backdrop is translated along the optical rails. The test series aimed to determine sensitivity to traditional BOS properties such as values for t and L. BOS calculations are typically sensitive to the t/L ratio as discussed by Hargather and Settles [10]. The lens is placed into the test section and removed from the test section to obtain the "hot", and "cold" images, respectively, for BOS measurements. A Phantom V711 high-speed camera was used to obtain the BOS images set at a frame-rate of 7500 frames/second for full megapixel resolution (1280x800 pixels). A Nikon 80-200 mm zoom lens was used on the camera and was set to approximately 135 mm of zoom. The camera lens was focused to the BOS background. Illumination in these tests was provided by the Ushio SugarCUBE ultra white LED light source since fast exposures were not necessary. The values of

t and L were measured with the assumption that the camera begins at the second collecting schlieren lens. This assumption is different than that of the typical BOS arrangement where the camera is assumed to begin at the outer edge of the camera lens. The internal optics of the camera have no effect on the BOS t/L measurements as shown in Hargather and Settles [10]. As a result, it follows that the beginning of the optics used to recollect the parallel light to a point are analogous to the camera's internal optics. As such, the t and L values are measured within the test section. The commonly used value of $L - t$ for refractive angle calculation is simply the distance between the schliere and the BOS backdrop.

Varying the t/L ratio is obtained by translation of the BOS backdrop along the optical rail. The refracting object is placed in the test section, and its position is measured along the rail as the value for t. The location where the BOS backdrop should be placed in the test section L is calculated for the desired t/L ratio by:

$$L = t + T_r t \tag{3.5}$$

where T_r is the target value for t/L ratio

The transparent BOS backdrop is translated along the rail to the calculated L location. The BOS testbed is schematically shown on Figure 3.6. The "hot" and "cold" image are taken at the desired t/L ratio, and saved for the theoretical refractive field development and the BOS determination of the refractive profile through correlation.

Correlated Solutions' VIC2D is used to obtain orthogonal pixel shifts. The software VIC2D identifies regions of high contrast and where those high contrast regions move through individual correlation subsets. The software requires two images at a minimum to perform a correlation. The hot image is the displaced image and the cold image is the reference image. Regions of interest for correlation were first selected to reduce computational demand. Tools within VIC2D allow for selection of the round area that is the plano-convex lens in this testing. The outside border of the plano-convex lens was selected using the circle tool in VIC2D. From the correlation region selection, an adjustment to the subset size was performed next. The subset size is the region for which the correlation algorithm seeks to segment and register throughout the image. The image registration calculated where that individual subset of the image has shifted to between the hot and cold image. The start point is a location in the cold image that can be identified in both of the the hot and cold image and is a location where the correlation algorithm begins. The subset size is an important consideration for the resolution of the BOS reconstruction. Figure 3.7 displays the post-processing settings with a view of the correlation subset.

VIC2D doesn't pad images, so it will only perform a correlation beginning at pixel locations that are greater than 1/2 of the selected subset size. For the BOS post-processing it is important that the subject not be close to the border of the image. The subset size also controls the amount of distortion generated from the correlation algorithm. Ideally, a small subset is used to resolve fine displacements in the images. The subset size is an odd value for which the center of each subset

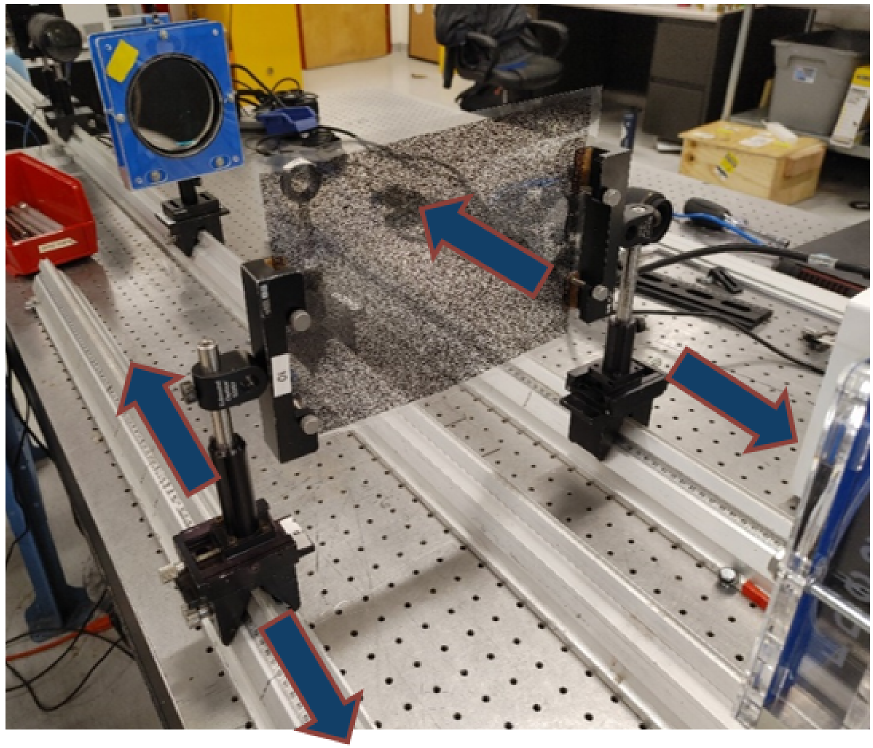

Figure 3.6: Parallel light BOS test bed. Optical rails allow for translation of the transparency in the parallel light focused shadowgraph setup

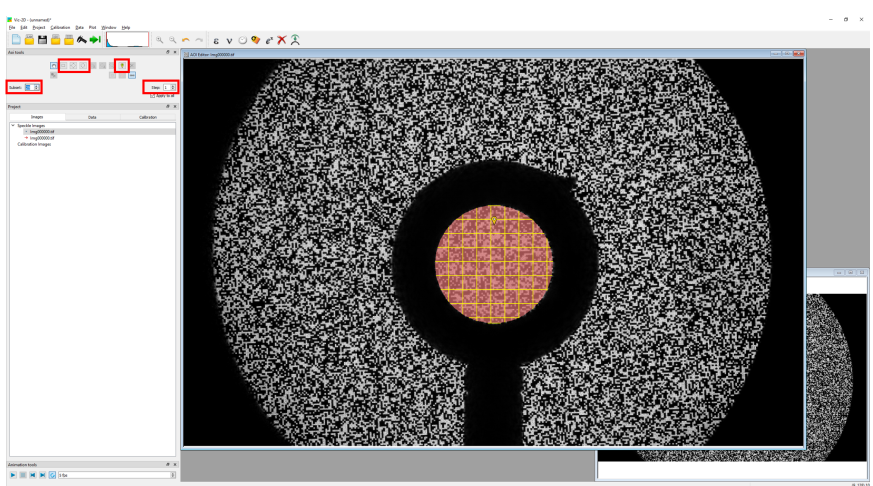

Figure 3.7: VIC2D post-processing window displaying step size, subset for correlation, selection tools, and start point

is searched for in the image. Smaller subsets may be obtained by decreasing the physical size of the regions of contrast in the backdrop. In this test series, printing on the transparency with a higher density of speckling was the method utilized for decreasing the required subset size. Care was taken such that borders of each feature were still resolved and in good focus. Correlation relies on the high contrast between light and dark boundaries and a gradient of intensity is not appropriate for correlation. An iterative approach was taken to minimize the subset and step size. In order to reduce computational load further, a step size can be specified.

For the two image series of tests performed with varying speckle densities on the BOS backdrop, the correlation subset sizes were 35 x 35 for the large speckle pattern, and 29 x 29 pixels for the small speckle pattern, with a step size of 1 for maximum resolution. An output of the VIC2D correlation algorithm is a contour of u pixel shift and v pixel shift. These displacements are similar to the displacements seen in schlieren imaging. These displacements are related to angles via the trigonometry of the setup. Tools within the VIC2D software allow for selection of vertical and horizontal line slice to be extracted from the VIC2D correlation u and v contours. Line slice extractions in conjunction with physical measurements are used to obtain refractive angle profiles similar to those obtained through traditional schlieren. The line profiles are converted from a pixel displacement contour to a refractive angle contour by Equation 1.3 [10]. The refractive field contour obtained from the calculation is equivalent to that visualized through the schlieren technique as discussed in Equation 1.2.

The calculation of the BOS refractive angle field is analogous to the vertical and horizontal knife edge orientations. The displacement in the u contour is the same as vertical knife edge displacements visualized in schlieren imaging. Likewise, the v displacement contour converted to a refractive angle field is the same as the horizontal knife edge displacements visualized in schlieren imaging.

The refractive angle obtained through geometric optics and obtained through the BOS post-processing can be compared with one another. Figure 3.9 displays the vertical pixel shift versus location in calibration lens.

The 2-m-focal-length lens is too strong of a disturbance for the values of t/L to have any noticeable effect on the correlation, but the pixel shifts agree with one another for the range of t/L ratios tested. The refractive angles obtained through this testing are appropriate to use within quantitative BOS measurements. The numerical derivative of the correlated refractive field is compared with the derivative of the refractive field obtained through geometric optics. There is good agreement in the numerical derivative and therefore the refractive angle profile is asserted to be correct and the parallel light BOS methodology appropriate for use in quantitative applications.

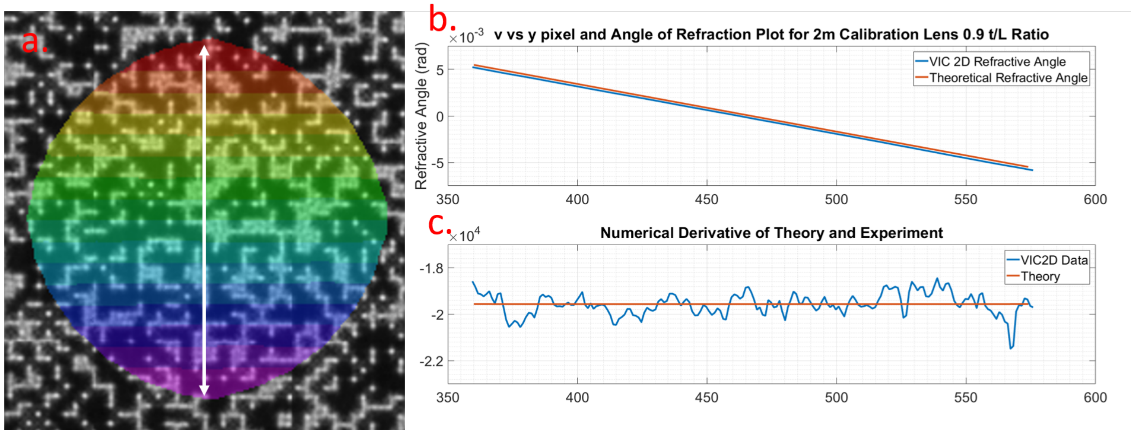

Figure 3.8: (a) VIC2D output of v contour. The white line indicates the extracted profile changed to refractive angle. (b) Refractive plot comparison between the refractive angle and theoretical refractive profile. (c) Numerical derivative versus location between theoretical profile and experimental refractive profile

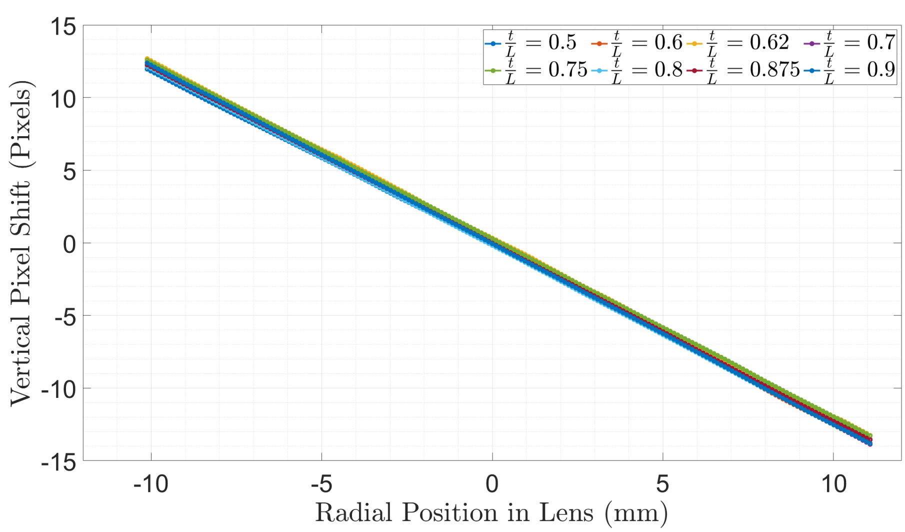

Figure 3.9: Pixel shift versus radial position in lens. On the scale of t and L with the 2m calibration lens the impact of t/L doesn't affect the pixel shift

3.2.2 Quantitative BOS for Conical Flow

A similar approach is taken to obtain quantitative measurements from the BOS test setup discussed in Section 2.4 utilizing the methods developed in Section 3.1.2. The difference between the traditional schlieren reconstructions is that the change in refractive angle ($\Delta\varepsilon$) is directly obtained through the post-processing in VIC2D and the trigonometry of the test setup. The v contour output from VIC2D is used for the reconstruction. The refractive angle is obtained through the physical calibration distance, measured t and L values, and the VIC2D pixel shift. The refractive angle obtained through these measured quantities is defined by:

$$\varepsilon = tan^{-1}\left[\frac{(\text{pixel shift})p}{L-t}\right] \tag{3.6}$$

where p is the physical pixel to distance value, L is the distance between the collecting field lens and the BOS backdrop and t is the distance from the collecting field lens and the schlieren object.

The angle obtained from this calculation is the change in refractive angle ($\Delta\varepsilon$). The change in refractive angles is the input to the Abel inversion. As with the traditional knife edge schlieren data, locations about which to invert must be determined from the images. A separate set of MATLAB codes was utilized to determine these locations. Due to the BOS backdrop, the shock wave cannot be identified by eye in the unprocessed images. The change in refractive field is already obtained and used to determine the locations about which to invert. Normalizing the change in refractive angle field and visualizing the field as an image results in a pseudo-schlieren image. Figure 3.10 displays the normalized image used to identify the endpoints for the Abel inversion. It is evident that the post-processing in VIC2D results in substantial blur to the field, however, this image clearly displays the shock wave and apex of the cone. A simple MATLAB script was written to prompt the user for the location of the apex of the cone and the endpoint in the image of the oblique conical shock wave. A linear least squares regression was performed between the two endpoints to determine the height above the cone for which the spherical symmetry assumption of the Abel inversion is appropriate. After rounding these values, they are saved for the Abel deconvolution algorithm.

Additional inputs to the BOS inversion are nearly the same as those used to input to the quantitative schlieren inversion algorithm. The mask that is applied onto the inverted data is slightly different from that used in the quantitative schlieren work flow. The mask applied is a thresholded image obtained through Otsu's ideal threshold [36] on the normalized change in refractive angle field image. The image has a morphological closing operation performed on it utilizing a diamond structural element to fill in the cone outline. This image is saved out and read back in during the inversion process. Additional properties that are imported during the inversion process are p, the pixel spacing, and the inputs for

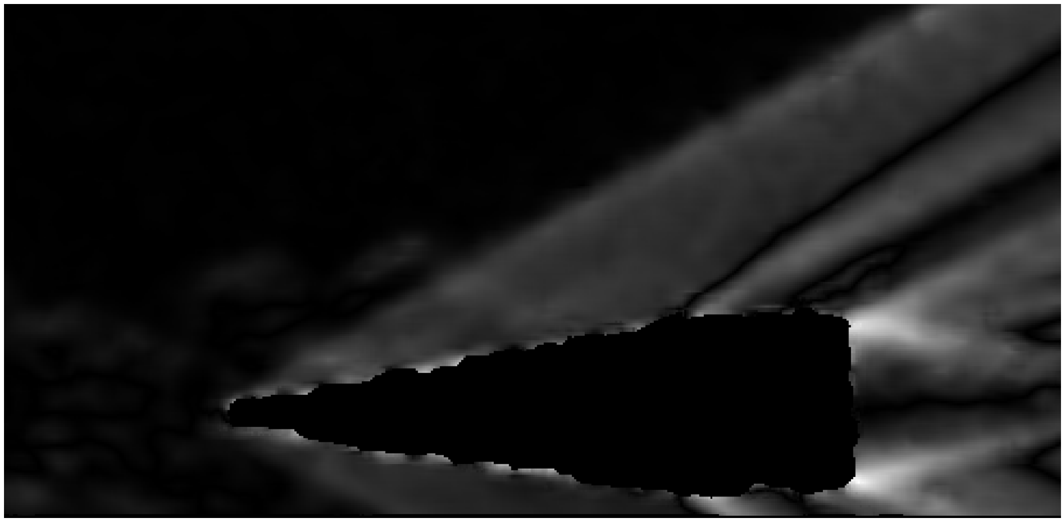

Figure 3.10: Normalized change in refractive angle field image used to determine inversion locations

the Gladstone-Dale and density calculation of the atmospheric conditions at the time of test.

The inversion process is performed on the BOS image utilizing the Abel inversion and the Gladstone-Dale relationship. The reconstructed density field is visualized via the MATLAB built in functions for contour plotting. The standard colormap jet is used to visualize the density variation as a change in color based on the variation in density. The contour overlay indicates that the highest density is obtained at the cone surface as expected from the theoretical Taylor-Maccoll conical flow relationships. Figure 3.11 displays the quantitative overlay of the BOS measured density field.

Only a single BOS data set, with a resolution of 256x512 pixels, was obtained here.

3.3 Nondimensionalization of Flow

The Taylor-Maccoll conical flow solution states that the flow only changes properties across conical rays originating at the apex of the cone. Normalizing the vertical distance by the total vertical distance from the cone surface to the oblique conical shock wave allows for a comparison between all points in the image with the theoretical conical flow solution. This nondimensionalization also allows for a direct comparison between quantitative schlieren and quantitative BOS measurements.

Quantitative data from the schlieren images is obtained via a vertical line profile extracted from the contour overlay. The largest spacing between conical

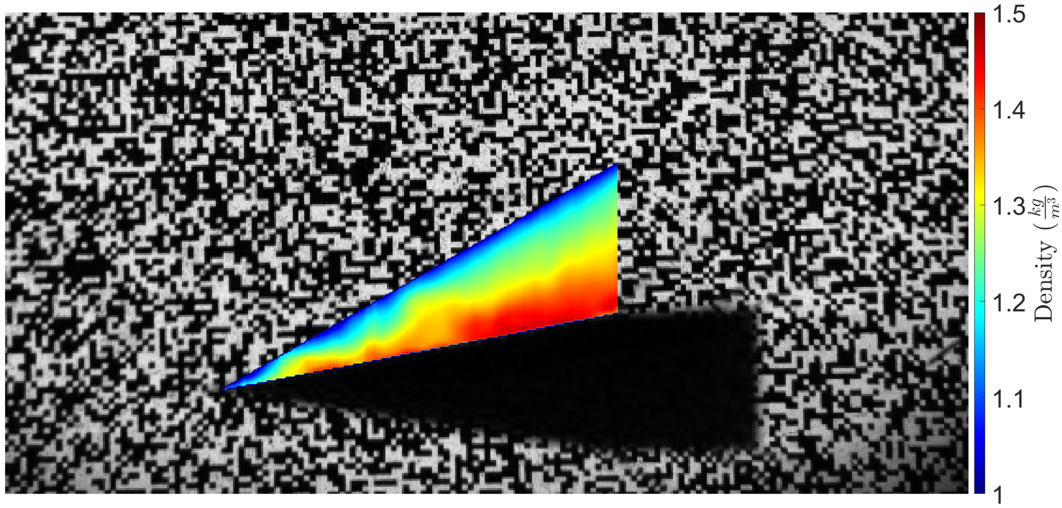

Figure 3.11: Quantitative overlay of inverted density field obtained through BOS post-processing

rays in the experimentally measured fields is seen at the end of the conical portion of the projectile. As such, the highest resolution comparison should be drawn utilizing the last pixel column from the 10° conical tip of the projectile. This column of data is extracted and compared with the Taylor-Maccoll conical flow relationships.

A simple nondimensionalization of the flow is used, where the pixel at the cone surface is asserted to be a value of 0 and the location 1 is at the outside edge of the oblique conical shock wave. In this scenario, the length scale is a function of vertical height above the cone surface defined by:

$$g = \frac{b}{h} \tag{3.7}$$

where g is the normalized height above the cone surface, b is the current height above the cone surface and h is the total distance between the oblique conical shock wave and the cone surface at the pixel column of interest.

These nondimensional coordinates are selected for comparison with the theoretical density variation. The Taylor-Maccoll conical flow solution provides values for the high speed gas dynamics properties just inside oblique conical shock wave and at the cone surface. A common way of presenting the flow properties at these locations is in a normalized form where the density at the desired location is in a ratio with the local atmospheric density. The Virginia Tech Compressible Aerodynamics Calculator provides normalized values for the density at the cone surface and inside the oblique conical shock wave [39]. Choosing this nondimensional space, the value of 0 is assigned to the cone surface density, and 1 is assigned to the outside edge of the oblique conical shock wave.

Conveniently, both of these properties are provided through online compressible aerodynamics calculators. The inputs to the compressible flow calculator are typically parametrized by the cone half angle and incoming Mach number. In order to obtain a theoretical comparison with the Taylor-Maccoll conical flow solution, the cone half angle, local atmospheric density, and Mach number must be known.

Quantitative schlieren reconstructions are performed at multiple resolutions and are normalized for the comparison to the theoretical density variation at the back of the conical portion of the projectiles. Two resolutions are presented here and compared with the theoretical density variation obtained from measured quantities at the time of each test. Each individual resolution is compared with the specific Mach number of the flow that is measured from the images.

The lowest resolution schlieren reconstruction was obtained utilizing a Phantom V711 high-speed camera recording at 40000 frames per second at a resolution of 512x256 pixels. The test series uses a reconstruction quantitative schlieren calibration process and a horizontal knife edge. The properties measured at the time of test relevant to the schlieren reconstruction are presented in Table 3.1.

Table 3.1: Test 1 measured atmospheric and flow properties for quantitative theoretical comparison

Atmospheric Pressure	Absolute Temperature	Pixel Calibration	Measured Muzzle Velocity	Mach Number
(kPa)	(K)	(mm/pix)	(m/s)	
84.5	286	0.122	712	2.10

3.4 Projectile Tracking

Measurement of the cone velocity is obtained through the spatio-temporal resolved data from the parallel light present in schlieren imaging and the timing infrastructure in high-speed imaging, respectively. With known pixel sizing, the velocity can be obtained if the number of pixels moved between subsequent frames can be measured.

Each frame recorded by the high-speed camera is spaced apart in time by the inverse of the framerate. The timing inaccuracy between each frame's nominal spacing in time was within $\pm$ 1 ns of the expected time spacing. With the known timing between each frame, an algorithm was written to identify the outline of the cone in each image.

A MATLAB routine was designed to extract the outline of the projectile through optimal thresholding of an image and the built-in function "regionprops". The regions identified in the MATLAB function provide a bounding box for each 8-connected region in a binary or grayscale image provided to the algorithm. Of interest for the projectiles is the centroid and the bounding box provided by the MATLAB built-in function. Figure 3.12 displays the bounding box and centroid marker for this specific test series.

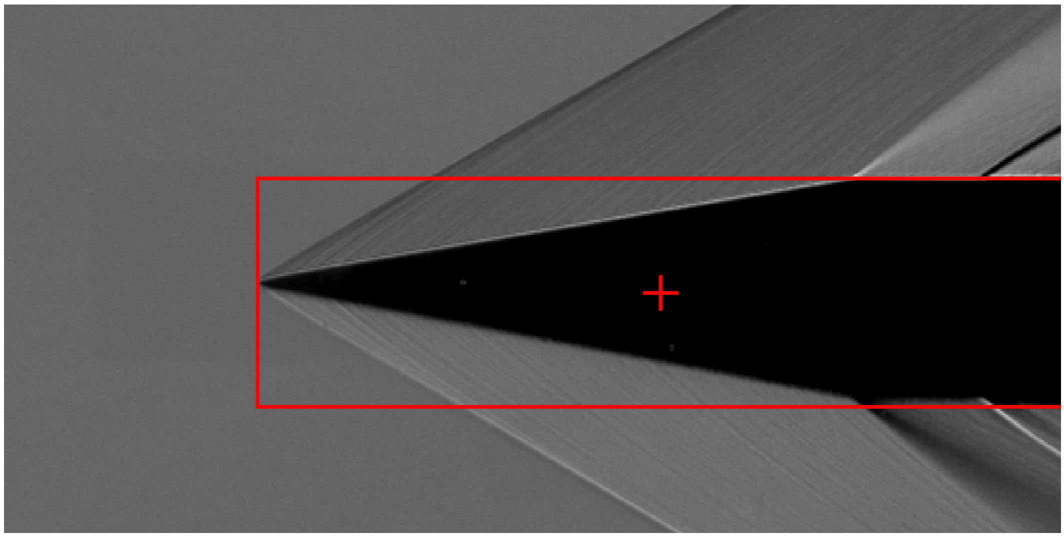

Figure 3.12: Cone image displaying bounding box and centroid marker obtained from tracking MATLAB algorithm

Tracking the displacement of one of the edges of the bounding box allows for a determination of the velocity. Two subsequent images where the cone is in frame were used to determine a local velocity. The x coordinate of the apex of the cone is identified by Equation 3.1. The location of the apex of the cone is identified in all remaining images where the cone is in frame, and a displacement between the x coordinate of the apex was saved. The velocity was determined by averaging the number of pixels moved between subsequent frames. An average of these displacements was taken, and then multiplied by the frame rate and the pixel to distance calibration. This results in a measured average velocity of the projectile.

The experimentally measured velocity is converted to a Mach number through Equation 1.4 and input to an online conical flow calculator [39]. In this equation, the measured quantities are velocity and Temperature. The value for the specific gas constant R and ratio of specific heats γ are taken as the standard values for air of 287.058 J/kg/K and 1.4, respectively.

3.5 Density Reconstruction

The experimental density reconstruction is compared with theoretical values. The calibration and Abel deconvolution were performed to obtain a composite contour overlay of the density around the projectile. Three tests were performed at nominally the same Mach number with varied imaging conditions, which are summarized in Table 3.2. Figure 3.13 displays the composite contour overlay obtained for the low resolution schlieren reconstruction. The contour overlay displays a compression from free stream to the cone surface.

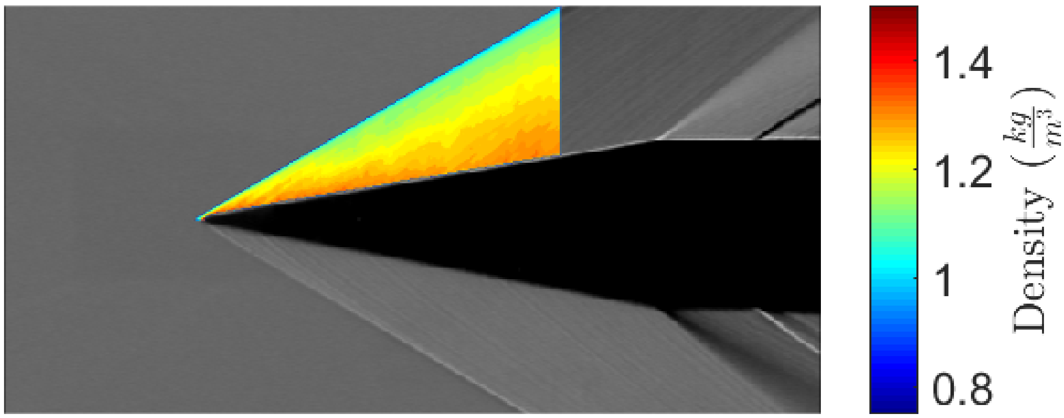

Figure 3.13: Quantitative schlieren contour overlay for low resolution 10° half angle cone traveling 715 m/s

The projectile was tracked to determine the Mach number of the flow around the cone. With the known half angle of the cone and incoming Mach number, the two theoretical density points immediately after the shock wave and at the cone surface were obtained from the compressible aerodynamics calculator. Normalized property variations are shown in Table 3.2.

Table 3.2: Normalized density points for 10° half angle cone cones tested here

	Mach Number	$\frac{\rho_2}{\rho_1}$	$\frac{\rho_c}{\rho_1}$	Image Resolution (mm/pixel)
Low Resolution Schlieren	2.10	1.071	1.218	0.122
High Resolution Schlieren	2.12	1.073	1.221	0.0280
BOS	2.09	1.071	1.217	0.171

It is assumed here that the density between the inside of the oblique conical shock wave and the cone surface varies linearly along the vertical distance from cone surface to inside of the shock wave. This line between the two theoretical points used as a theoretical profile which can be compared with the experimental density variation.

The highest resolution schlieren image set is taken utilizing the Phantom VEO 990S 4K high-speed camera. A full 9.4 megapixel image set is obtained at the camera's maximum resolution recorded at 900 fps utilizing a horizontal knife edge schlieren system. The deconvolution is performed, and results are shown in a composite density contour overlay in Figure 3.14.

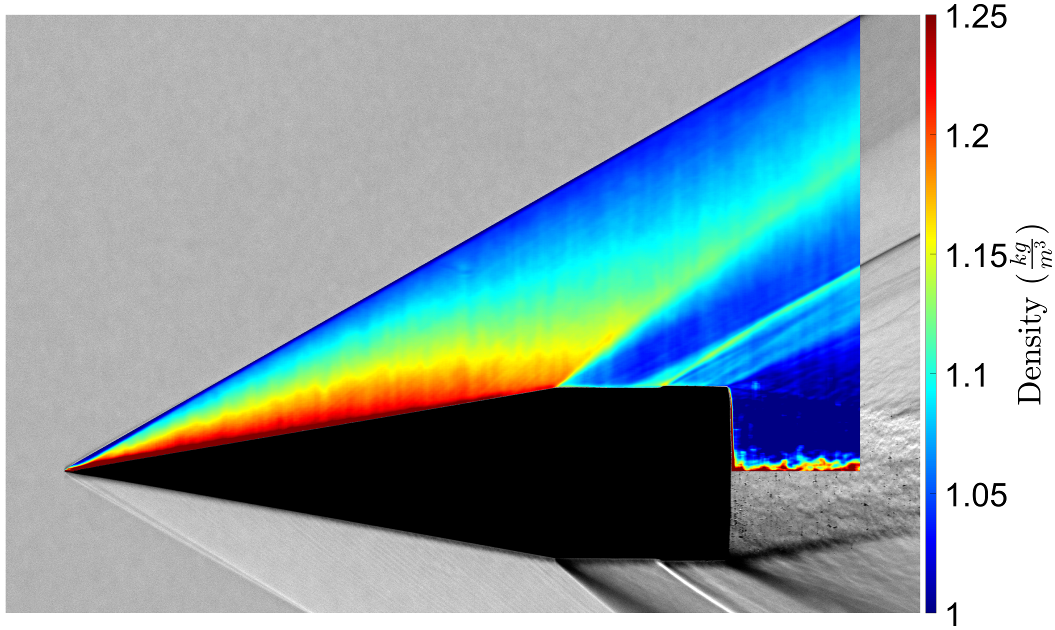

Figure 3.14: Quantitative schlieren contour overlay for high resolution 10° half angle cone traveling 730 m/s

When recording at 900 fps, the high-speed camera is only able to capture a single frame where the cone is present. This requires that the Mach number be determined in a different way. The Taylor-Maccoll conical flow relationships were used in reverse to identify a velocity from two measured or known properties. The flow velocity can be obtained from a single image if the assumptions of Taylor and Maccoll are met. Namely, the assumptions of zero Angle of Attack (AoA) and irrotational flow. Any AoA of the projectile here is minimized though the pitch control on the PDGS. The boundary layer is the only region where the flow is rotating during the cone testing. The boundary layer has been evaluated for long distances in a similar geometry by James [40]. The height of the boundary layer is only of importance when the distance downstream from the tip of the cone is approximately 6 times the diameter of the projectile in the geometry tested by James [40]. The thickness of this boundary is not substantial until the distance from cone tip is much greater than the overall length of the projectiles evaluated here. As the flow condition of $M \approx 2.12$ remains supersonic at all locations around the cone, information cannot propagate far from the cone face. Since classical Taylor-Maccoll conical flow has been achieved, any two flow parameters can be used to determine the remainder of the flow parameters. The cone half angle and shock wave angle are thus used here to determine Mach number.

The shock wave in the schlieren image is a very crisp light to dark boundary which can be identified manually in the image. The shock wave originates from the cone apex and the wave angle is measured between the center-line of the cone and the shock wave. The image processing software from the National Institutes of Health: ImageJ has a simple built-in angle measurement tool which was used to measure the wave angle. The cone half-angle is known to a high tolerance from the manufacturing process.

The online compressible aerodynamics calculator for Taylor-Maccoll cone flow [39] accepts an input of Mach Number and wave angle to determine flow properties such as the density for the flow. The measured wave angle of 29.4° is input into the calculator along with an assumed incoming Mach Number. Iterations on the input Mach number are performed to obtain the correct cone half angle of 10° in the output data. After several iterations, the Mach number was determined to be M = 2.12 for this flow case and the flow properties are given in Table 3.2

The single BOS data set that allowed for a reconstruction was recorded using the Phantom V711 high-speed camera recording at 40000 fps with a pixel resolution of 512x256 pixels. The BOS post-processing is performed using Correlated Solutions' VIC2D and is of a final resolution of 490x238 pixels since the correlation algorithm uses a correlation window that results in loss of data around the edges of the area of interest. The Abel inversion algorithm and density reconstruction are performed to display a composite density contour overlay. Figure 3.15 displays the composite density contour overlay on the BOS image.

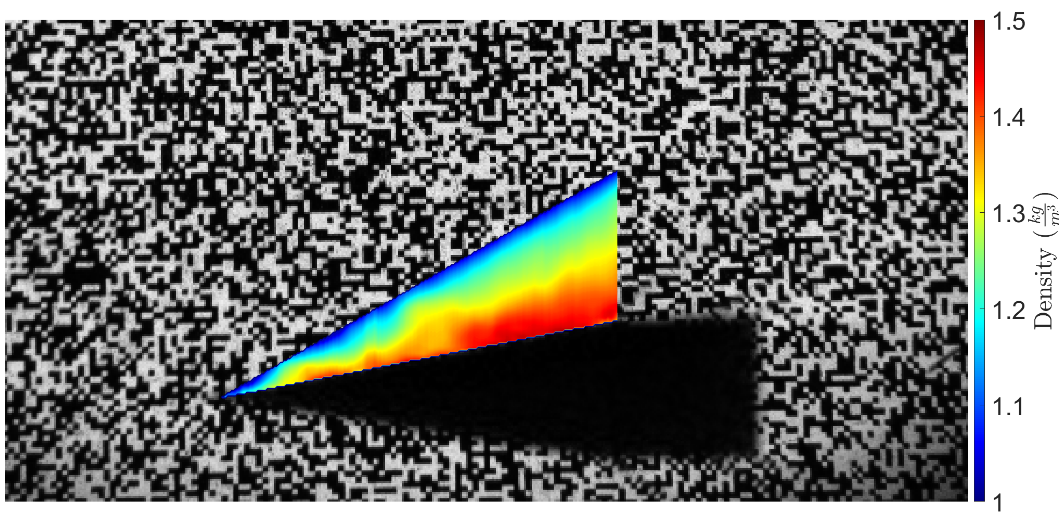

Figure 3.15: Quantitative overlay of inverted density field obtained through BOS post-processing

The velocity for this test is measured through the tracking algorithm discussed in Section 3.4. The Mach number obtained through this method is also approximately M = 2.10. A calculation through the compressible aerodynamics calculator is performed to determine the normalized density variations. The density ratios for this flow condition and the incoming Mach number are shown on Table 3.2.

The normalized density values are obtained for each flow condition, but the normalized densities do not vary substantially from one another. The change in the normalized density only varies in the hundredths place at the cone face, and in the thousandths place inside the oblique conical shock wave. A single normalized density profile is therefore plotted with the line slices from each resolution of schlieren reconstruction and the single BOS density reconstruction. Figure 3.16 displays the density variation for a single theoretical profile, and the three experimental density profiles.

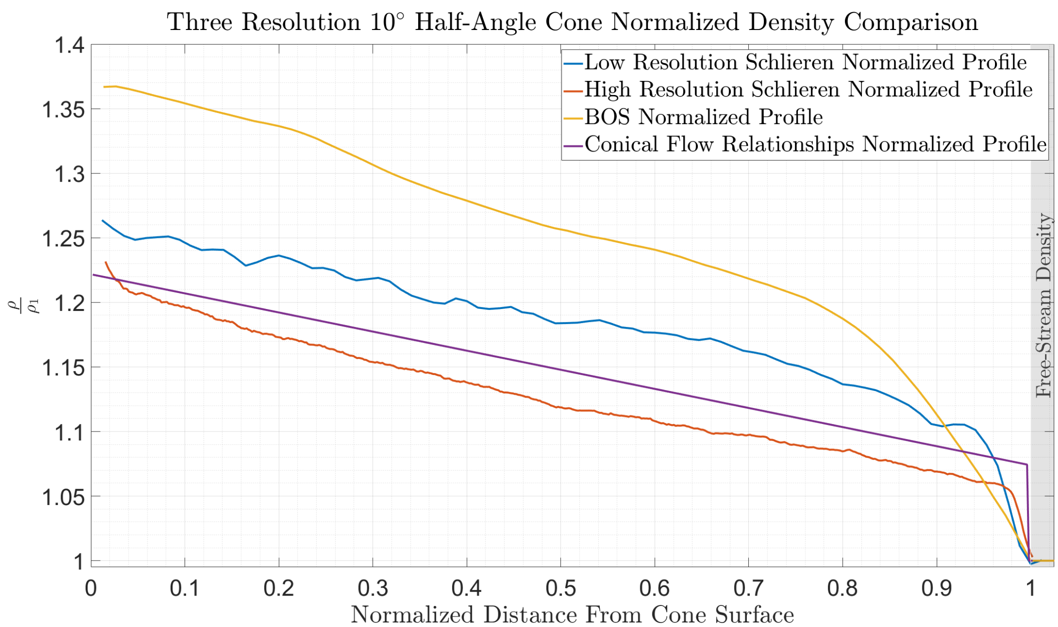

Figure 3.16: Normalized density variation for the three reconstructed density fields

The line of theoretical density variation is fit to an average of the property variation for the Mach number. The density at each location is normalized by the atmospheric density measured at the time of the test. All three density profiles have an apparent shock wave thickness which is larger than physically realistic, but representative of how the shock wave appears in the schlieren image. The overall apparent thickness of this shock wave is a function of the width of the schlieren test section. The refracted light that interacts with the knife edge at the focal point displaces along the entire optical path and therefore results in the apparent shock wave thickness in the schlieren image. The slope of the isentropic compression from inside oblique conical shock wave to cone surface is similar once the shock compression is complete for the three cases. Further analysis for each reconstructed density field allows for a comparison at individual locations along the cone.

An analysis was performed on each reconstructed density field from the cone image to examine the density profile at different locations along the cone length. The density profile at every pixel point along the cone legth was examined for comparison with the theoretical profile. Each location along the cone, represented by a column of pixels, should display a compression from inside the oblique shock wave to the cone face. The nondimensionalization was performed for each column of the reconstructed data. A selection of the reconstructions are shown in Figure 3.17. Pixel columns are extracted every 20 pixels along the length of the cone. The data are plotted with varying grayscale intensity, where line profiles extracted near the cone top are lighter gray and profiles more toward the rear are darker gray. Reconstructions begin with a high degree of error as fewer pixels are reconstructed in the Abel inversion near the tip of the cone because the distance from the cone tip to shock wave is small.

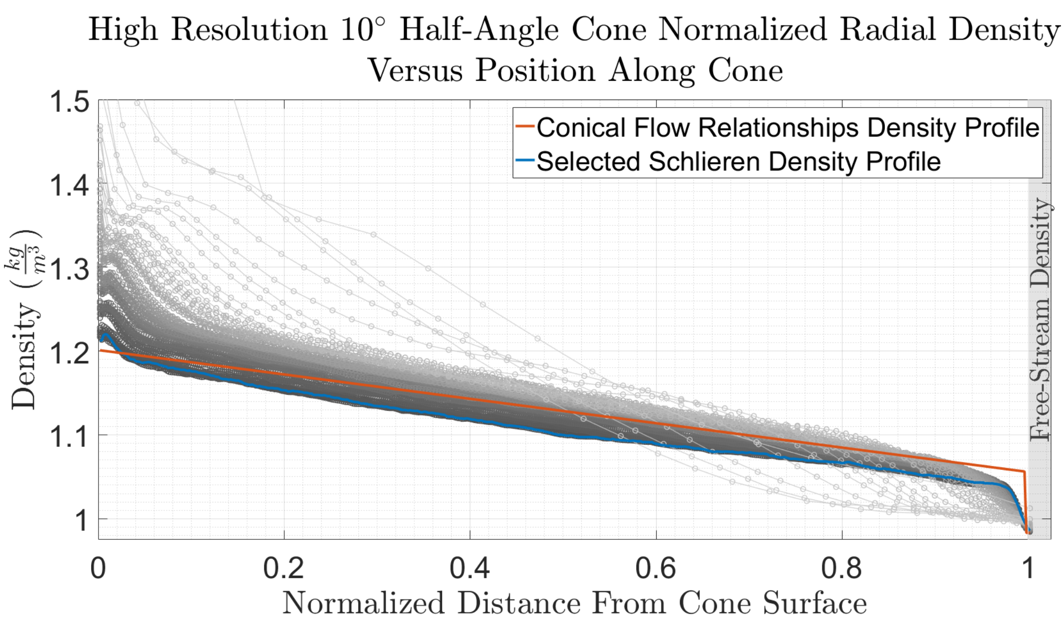

Figure 3.17: Nondimensional density variation as a function of position along cone for high resolution schlieren reconstruction. Line profiles are colored by intensity where darker grayscale indicates more near the rear of the cone.

This reconstruction displays a nonphysical shock feature when the reconstruction is of insufficient length to perform the measurement. Beginning from the apex of the cone rearward, the nondmensional reconstruction is plotted for every 20 columns of data. The total pixel width along the purely conical portion of the projectile is approximately 1200 pixels. Plotting every 20 columns of reconstructed data resulted in a discretization of approximately 60 individual locations. The nonphysical reconstruction for the shock wave's density profile is observed in the first 9 line profiles. This number of nonphysical shock wave reconstructions is approximately 15% of the distance between the cone apex and rear of the conical region of the projectile. It was determined that a selected density profile at the rear of the projectile provides the best comparison with the theoretical density profile because of the largest spacing between the conical rays and best resolved for quantitative schlieren imaging.

Similar line extractions along the cone were performed for the low resolution schlieren and BOS data sets. The low resolution schlieren reconstruction has fewer columns of data from which to reconstruct. Due to the alignment of the projectile in frame, the entire flow field around the conical region of the projectile cannot be reconstructed: the reconstruction requires the entire field to be visible from the shock wave to the cone surface, therefore the reconstruction stops when the shock wave reaches the edge of the field of view. Similar results are obtained for the low resolution schlieren with an initial inaccuracy of the profiles near the apex of the cone. Figure 3.18 displays the normalized density profiles as a function of position along the cone. High grayscale intensities indicate close proximity to the cone apex, and low grayscale intensities (darker) indicate more rearward distance along the conical region of the projectile. A similar distance of approximately 15% from the apex of cone was observed in the low resolution schlieren reconstructed field before the density profile accurately captures the expected profile.

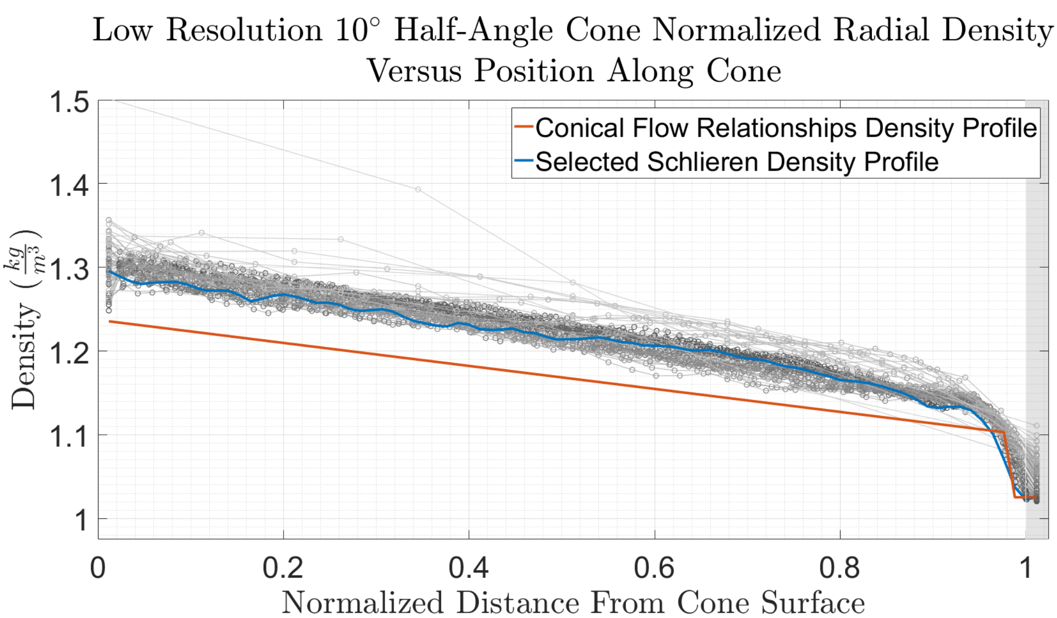

Figure 3.18: Nondimensional density variation as a function of position along cone for low resolution schlieren reconstruction. Line profiles are colored by intensity where darker grayscale indicates more near the rear of the cone.

The Background Oriented Schlieren reconstruction results in a different spread of the reconstructed densities as a function of position along the cone. Figure 3.19 displays the reconstructions for the BOS data set.

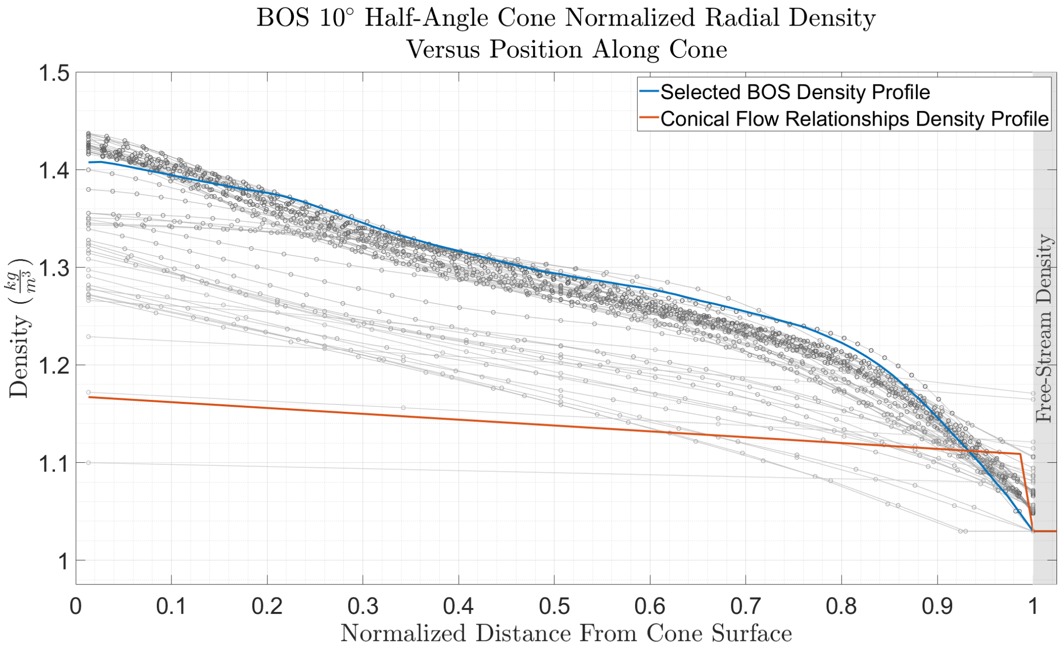

Figure 3.19: Nondimensional density variation as a function of position along cone for Background Oriented Schlieren reconstruction. Line profiles are colored by intensity where darker grayscale indicates more near the rear of the cone.

The reconstructed density field in the BOS data initially begins below the theoretical density profile. Further along the span of the cone, a similar convergence to a density field that contains a compression between oblique shock wave and cone face was observed.

3.6 Error Analysis

A standard error propagation was performed on the optically measured properties of the projectile for determining the error associated in the Mach number. The general propagation of uncertainty is described by Ku [41]:

$$\alpha_z = \sqrt{\sum_{a=1}^{N} \left(\frac{\partial Z}{\partial a_i}\right) (\alpha_i)^2} \tag{3.8}$$

where: α_z is the overall uncertainty in a measurement of a quantity Z, $\frac{\partial Z}{\partial a_i}$ is the current partial derivative of the functional form of Z with respect to the variable a_i, and α_i is the uncertainty associated with the variable a_i.

Applying the general propagation of uncertainty to the reported accuracy associated with the Extech SD700 laboratory weather station and the pixel uncertainty in the measurement from the tracking code allows for the determination of the uncertainty in the Mach number. The uncertainty in the cone angle is related to the manufacturing uncertainty, which here is insignificant compared to the other uncertainties. The uncertainties associated with the atmospheric property variation are displayed on Table 3.3.

Table 3.3: Uncertainties relevant for Mach Number determination from optically measured velocity and atmospheric conditions

Timing Drift	Pixel Measurement Uncertainty		Pressure Uncertainty	Temperature Uncertainty	Mach Number Uncertainty
(ns/frame)	(mm)	(pixels)	(kPa)	(K)	
0.111	0.122	1	0.005	0.8	0.0147

The propagation of uncertainty in the theoretical Taylor-Maccoll conical flow is determined through the uncertainty in the Mach number. The compressible aerodynamics calculator is queried to determine the ranges on the normalized relationships between the two density values for the specific conical flow [39]. Performing this query allows for a determination of the spread of normalized densities at the shock wave and cone surface.

In order to obtain the local density at the cone face and inside the shock wave, the ratio is multiplied by the local atmospheric density. The atmospheric density has an uncertainty associated with it from measured quantities. The general propagation of uncertainty on this final multiplication is carried out to calculate the overall uncertainty in the theoretical density field. The propagation of uncertainty in the theoretical field is very small. The largest uncertainty in this measure is a total of: $\pm$ 0.0034 kg/m^3. This is approximately a 0.03% uncertainty in the density. The change in compression seen within the error of the method is negligible.

Uncertainty within the Abel inversion is somewhat more challenging to obtain since the Abel inversion froward propagates any error from free-stream up to cone surface. Since the average background intensity is the value that is assigned to the atmospheric density (ρ_1), any variance in this value is propagated through the accuracy of the reconstruction. An estimate of the uncertainty in the density field is obtained by adding and subtracting one half of the standard deviation in the background intensity along the inclined shock profile and propagating this through the density calculation process. Since this is the pixel where the inversion begins, it will propagate the error through the Abel deconvolution algorithm. The inversion is performed for addition of half a standard deviation, and subtraction of half a standard deviation. With a theoretical and experimental profile obtained through the projectile tracking, a comparison with theoretical cone flow is obtained. Figure 3.20 displays the comparison in nondimensional distance.

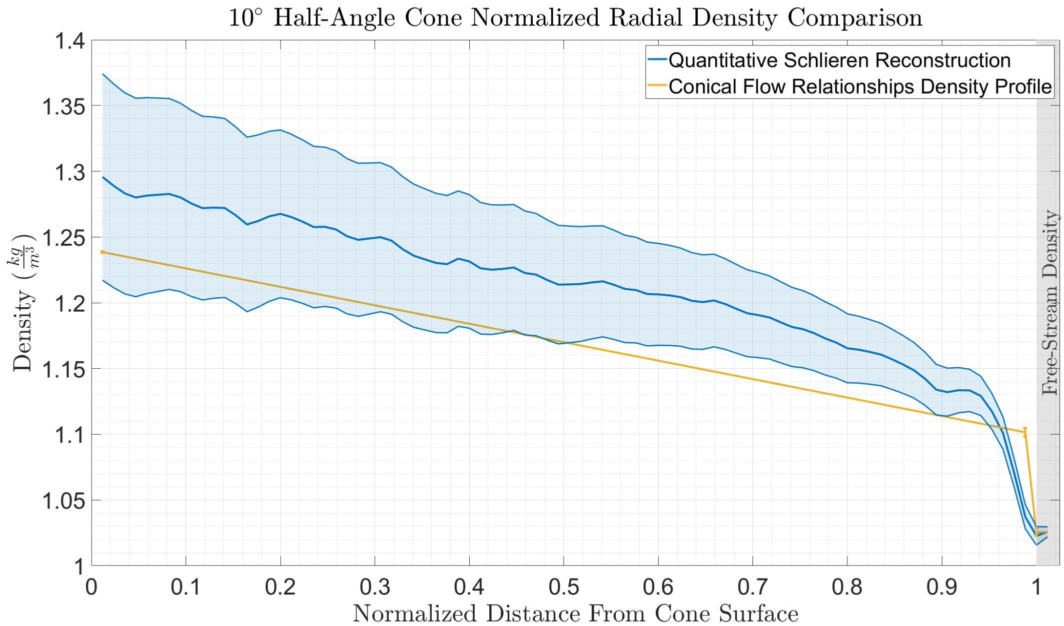

Figure 3.20: Nondimensional low resolution schlieren comparison between theoretical density profile and experimentally measured density profile

There is good agreement between the schlieren reconstruction and the theoretical Taylor-Maccoll conical flow along the vertical line slice extraction. An apparent shock wave thickness is seen in the experimental results. The reconstructed is shown throughout nondimensional space, and the theoretical profile is nearly within the error of the experimentally measured field. A signed error plot is generated along the vertical position between the theoretical density and the experimental density. The percent difference is defined by:

$$\% \text{ Difference} = \left(\frac{\text{Experimental-Theoretical}}{\text{Theoretical}}\right) \times 100\% \tag{3.9}$$

where the experimental value is obtained through the Abel deconvolution and the theoretical value is obtained from the Taylor-Maccoll conical flow relationships and the compressible aerodynamics calculator.

Figure 3.21 displays the percent difference between the theoretical and experimental data. At the shock wave there is a change in the sign of the error, but the overall signed error reconstructs a density within 10% of the theoretical density variation around the projectile. Improvements to the schlieren reconstruction can be obtained through increasing the pixel resolution.

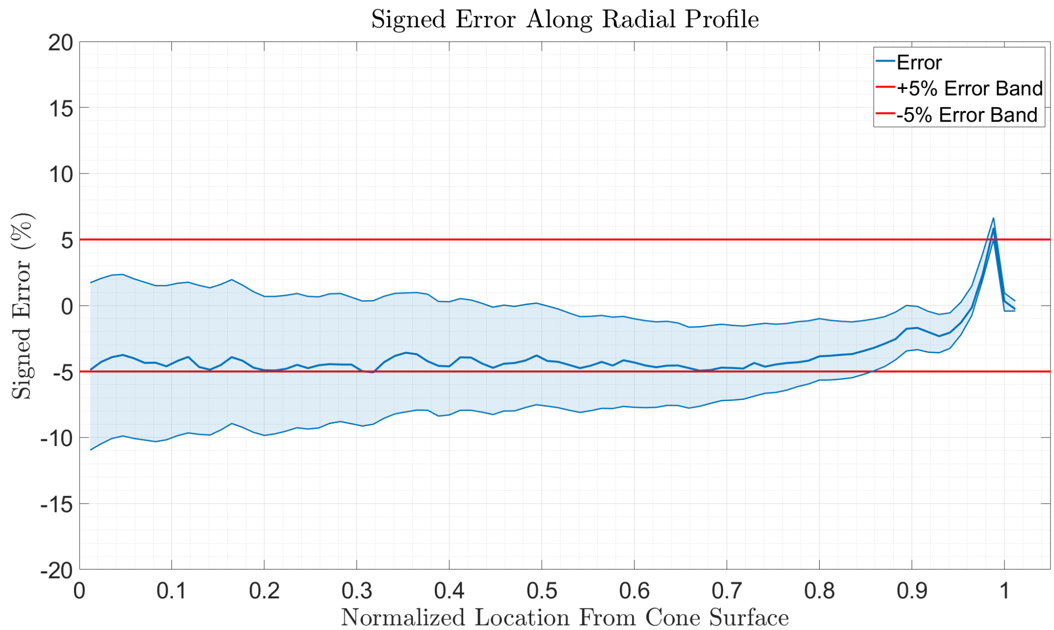

Figure 3.21: Low resolution signed radial density percent difference versus nondimensional location, desired $\pm5\%$ error bars indicated

The high resolution reconstruction has a similar plot generated displaying the density versus nondimensional location relative to the cone surface. A propagation of uncertainty into this test series for the theoretical method is not performed due to the negligible error determined from the projectile tracking methodology. The vertical density variation is shown on Figure 3.22. In this scenario, the density between the cone surface and the oblique shock wave is under-predicted, but to a lesser degree than the previous data set which over-predicted the density. An apparent shock wave thickness is also visible in this nondimensional comparison. In addition in this data set, the density can seen sharply increasing just off of the cone surface. This sharp increase is attributed to a better visualization of the boundary layer.

The intensity obtained in the boundary layer is different from that obtained through the isentropic compression up to the cone surface. The viscous effects and rotational flow that is present in the boundary layer results in large refractions and therefore a large intensity gradient immediately off of the cone surface. In this data set, the boundary layer is visualized in 7 pixels. The symmetry argument with the boundary layer in the Abel inversion is not appropriate to make. As such, the reconstructed densities are not correct in this region and cannot be used.

The increased resolution obtained from the Phantom VEO 990S camera results in a better reconstructed density field. The radial percent error plot for this data set is also generated for comparison to the theoretical profile. The error propagation of the noise variance through the Abel inversion returns an over-

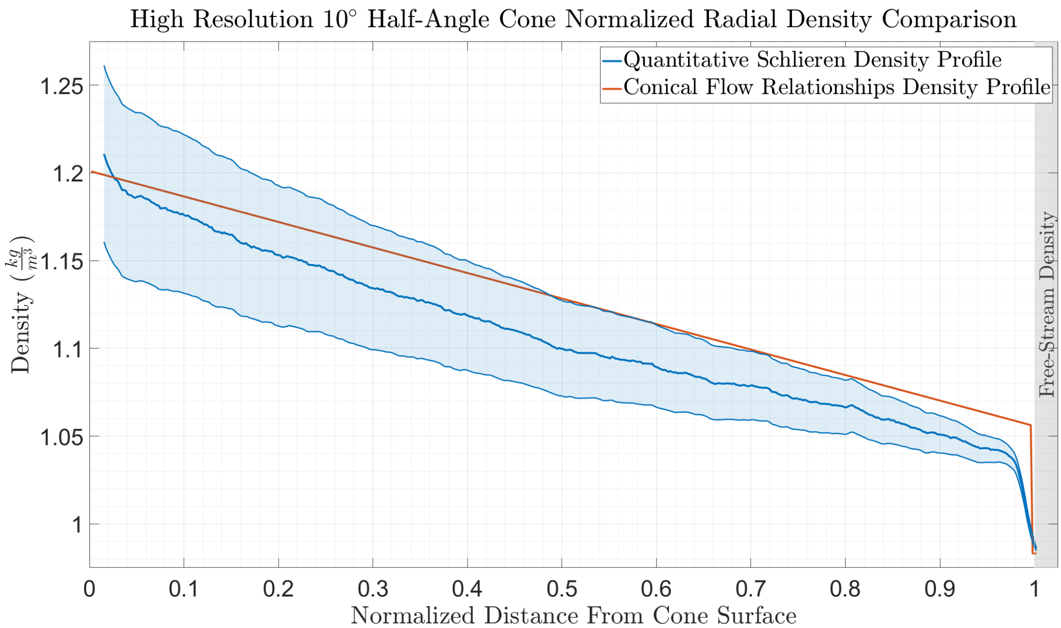

Figure 3.22: High resolution nondimensional comparison between theoretical density profile and experimentally measured density profile

all density within approximately 5% for all locations. The increase in resolution also increases the overall accuracy of the reconstructed conical flow. Figure 3.23 displays the percent error as a function of height above the cone surface.

The single BOS data set with a reconstructed density field has the nondimensional comparison for the specific flow conditions. The velocity for this test is performed through the time resolved nature of high-speed imaging and contains multiple BOS frames where the edge of the bounding box around the cone can be tracked. The Mach number obtained through this method is also approximately M = 2.10.

The uncertainty in the BOS method is performed based only on measurement uncertainty. In the method development test series it was determined that the measured value of t and L were measured from the outside edge of the second field schlieren lens. This testing determined that the optical plane at the center of the achromatic doublet collecting schlieren lens was the true reference for which t and L should be measured with respect to. The linear correction to this measurement was performed, and is the only measured property where the variance is quantified by measured values. In this data set, the theoretical Taylor-Maccoll conical flow solution is normalized and plotted as prior. Figure 3.24 displays the nondimensional comparison between the theoretical Taylor-Maccoll conical flow and the reconstructed density field through the parallel light BOS methodology.

Of specific interest, the BOS post-processing algorithm with a subset size of 21 pixels returns a smooth variation through the shock profile. This shock wave

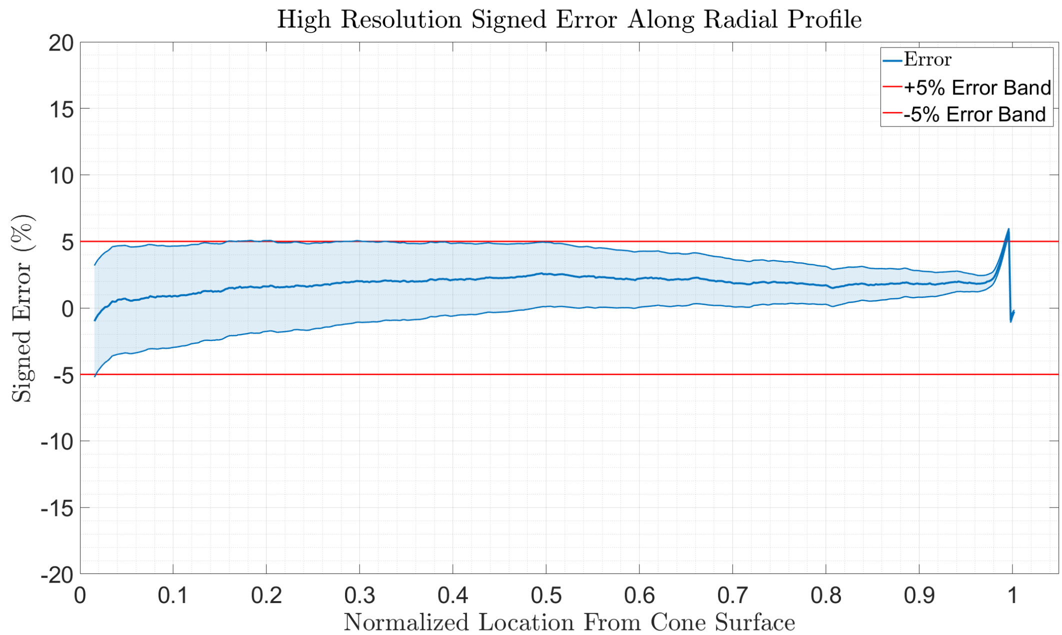

Figure 3.23: High resolution signed radial density percent difference versus nondimensional location, desired ±5% error bars indicated

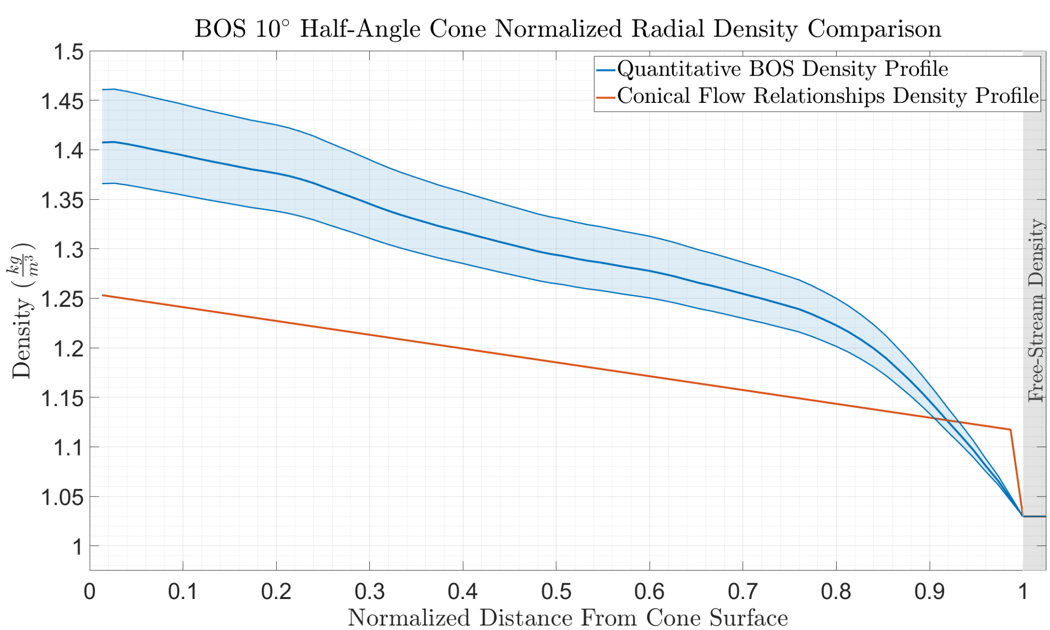

Figure 3.24: Nondimensional comparison between theoretical density profile and Background Oriented Schlieren experimentally measured density profile

is also of much greater width than that seen with the traditional schlieren measurement. The shock width is approximately 1/2 the size of the subset window used for post-processing, which may indicate that the processing algorithm is responsible for some of the apparent shock width. The BOS method over-predicts substantially from the theoretical density profile. The radial error plot is generated for this flow condition and compared with the theoretical density profile. Figure 3.25 displays the radial error profile.

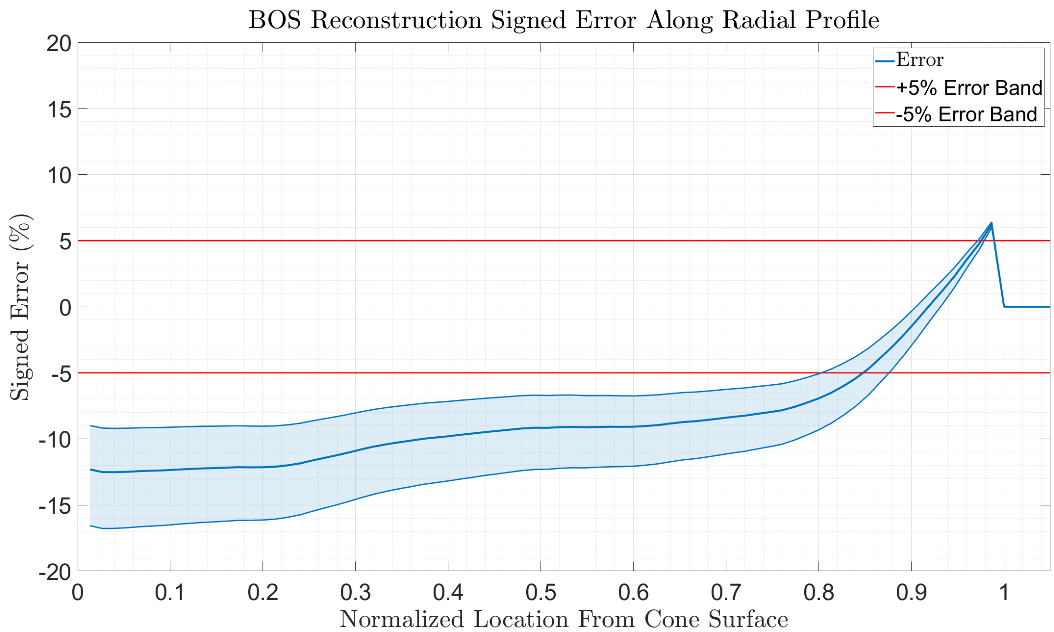

Figure 3.25: BOS signed radial density percent difference versus nondimensional location, desired $\pm 5\%$ error bars indicated

The error associated with this method is greater than that obtained through the traditional schlieren method. While the post-processing associated with the BOS method does provide information on the vector valued displacements in the field, the reconstruction at this resolution is not as accurate as traditional schlieren measurements. Higher resolution reconstructions could alleviate some of the averaging visualized in this test series.

CHAPTER 4

CONCLUSIONS AND RECOMMENDATIONS

Supersonic conical flow has been characterized utilizing schlieren imaging and BOS. Image pre- and post-processing techniques were developed for input to the Abel inversion for density reconstructions. Theoretical conical flow is compared with the experimentally measured density around the cones.

4.1 Conclusions

The density field around supersonic conical projectiles has been characterized through the use of quantitative schlieren measurements and quantitative BOS measurements. Agreement is seen between the two methodologies with the highest resolution schlieren image producing the most accurate result. A difference in reconstruction accuracy can be seen in the radial percentage error plots. Increasing the pixel resolution decreases a signed error from approximately 5% to approximately 2%. The Background Oriented Schlieren reconstructed field contains a higher degree of error of approximately 15%. An apparent shock wave thickness is observed due to the nature of schlieren imaging and the refraction being integrated along the entire optical path. The three reconstruction methodologies return an accurate slope of the isentropic compression from inside of the oblique conical shock wave to the cone face. An increase in the pixel resolution of the high-speed imaging allows for a more accurate reconstruction of the conical flow field. An investigation of the accuracy of the reconstructed field along the span of the cone resulted in a determination of the region for which the Abel inverted density results are accurate with the expected theoretical density variation. In the high resolution schlieren, a minimum distance of 15% of the length of the cone is necessary before the reconstructed density fields display both the shock wave jump in density and the expected compression to cone face. Methodologies for measurement of the Mach number result in negligible uncertainties when propagated through the velocity calculation.

High tolerance machining utilizing CNC machines allowed for the Mach number to be determined from simple geometric measurements taken within the schlieren images of the supersonic projectiles. The projectiles were designed for optimal ballistic launch, and the overall setup was tuned taking into account the specific friction between the gun barrel and the conical projectile. A new BOS method was developed and proof testing was performed to ensure that refractive angle gradients obtained from the setup can be used in quantitative measurements around supersonic cones. A quantitative comparison between traditional schlieren reconstructions and BOS measurements with this system was performed.

The novel parallel light BOS method has been developed and proof tested for both general refraction measurement as well as quantitative measurement of conical flow. A series of tests using the BOS methodology were performed to determine the system's sensitivity to t and L and other common BOS setup parameters. It was determined that decreasing the point source size of the light in the parallel light BOS setup is the most effective way of increasing the quality of correlation and therefore accuracy in the reconstruction of schlieren fields.

4.2 Recommendations for Future Work

Further experiments should be performed to determine properties such as aerodynamic coefficients, measurement applicability to AoA, additional post-processing techniques for deconvoluting the path integrated change in refractive angle field, and additional flow geometries such as spherically blunted cones or cones of differing half angle.

Additional effort should be expended to evaluate the applicability of the method to calculate aerodynamic coefficients such as the coefficient of drag C_D and/or the coefficient of lift C_L. The assumption of isentropic compression inside the oblique conical shock wave should be applied to determine the pressure distribution around the free flight cones. The schlieren reconstruction in the wake behind the projectile should be evaluated to calculate the aftbody drag at the rear of the projectile. An evaluation to determine the gaseous species in the wake should be performed, in addition to performing inversion techniques which can account for asymmetries in the flow field.

Previous studies have applied the BOS measurement technique to geometries in supersonic flow utilizing wind tunnels. Studies such as Venkatakrishnan and Meier and Kato et. al. display the applicability of the Radon inversion and Parallel Slice Theorem for Computed Tomography reconstruction of the three-dimensional flow field [19, 20]. The benefit of using the Radon Inversion in place of the Abel Inversion algorithm is that there is no restriction on the model's symmetry. Despite other authors utilizing the Radon inversion and filtered back-projection algorithm, studies in the past have all utilized axi-symmetric models. Projectiles of differing geometries or asymmetries in the form of AoA should be evaluated utilizing this method, but not the Abel inversion. As a result, asymmetric fields can be reconstructed, but this necessitates that multiple camera viewpoints must be used for reconstruction. Further works should involve an implementation of the parallel slice theorem and Radon inversion.

The BOS methodology in diverging light suffers dramatically from depth of field limitations, but the parallel light solves some of these problems associated with these measurements. The parallel light BOS does lack sensitivity to variation in t and L values for the refractions tested. Further refractions should be characterized in the parallel light to determine the setup values for t and L that result in a different sensitivity to refractive disturbances. Additional focus characterizations and methods to determine the required degree of parallel light in the test section through the iris aperture size should be performed.

The post processing techniques utilized in the BOS reconstructions are limited to the correlation algorithms that are used in solid mechanics applications. In solid mechanics applications, strains or other deformations measured through DIC are continuously varying fields. Shock waves by definition are discontinuous changes in high speed gas properties, so the use of a tool typically used for smoothly varying fields presents some challenges. Additional post-processing algorithms which can be modified by the user to capture the discontinuous nature of shock waves are needed. Algorithms such as Optical Flow discussed by Horn and Schnuck provide similar displacement fields with a relatively simple implementation [42]. The Horn Schnuck optical flow algorithm is built around a conservation of intensity argument between the hot and cold BOS image. A post-processing algorithm such as this could be used in conjunction with a correction for the jump at the shock wave. Further works to utilize this post-processing algorithm in the BOS reconstructions is recommended.

The applicability of the Taylor-Maccoll conical flow solution to conical flow has been shown to accurately predict the property variation around small cone half angles and moderate supersonic flow conditions [14]. Larger cone half angles or higher supersonic and hypersonic flow conditions should be evaluated for quantitative reconstructions.

REFERENCES

[1] Geoffrey Ingram Taylor and J. W. Maccoll. The air pressure on a cone moving at high speeds. *Proceedings of the Royal Society of London. Series A, Containing Papers of a Mathematical and Physical Character*, 139(838):278–297, 1933.

[2] J. W. Maccoll. The conical shock wave formed by a cone moving at a high speed. *Proceedings of the Royal Society of London. Series A - Mathematical and Physical Sciences*, 159(898):459–472, 1937.

[3] G. S. Settles. *Schlieren and shadowgraph techniques: Visualizing phenomena in transparent media*. Springer-Verlag, 2001.

[4] Gary S. Settles and Michael J. Hargather. A review of recent developments in schlieren and shadowgraph techniques. *Measurement Science and Technology*, 28:042001, 2017.

[5] A.K. Agrawal, K.N. Alammar, and S.R. Gollahalli. Application of rainbow schlieren deflectometry to measure temperature and oxygen concentration in a laminar gas-jet diffusion flame. *Exp.Fluids*, 32(6):689–691, 2002.

[6] Josef Stricker, Boris Zakharin, Binyamin T. Hornick, and Florence Rosenblatt. Bidirectional quantitative color schlieren. *Optical Engineering*, 45(12):1 – 6, 2006.

[7] G. E. Elsinga, B. W. Van Oudheusden, F. Scarano, and D. W. Watt. Assessment and application of quantitative schlieren methods: Calibrated color schlieren and background oriented schlieren. *Exp. Fluids*, 36(2):309–325, 2004.

[8] Kyle O Winter. *Irregular Reflections of Unsteady Shockwaves*. phdthesis, New Mexico Institute of Mining and Technology, 801 Leroy Place Socorro, NM 87801, January 2021.

[9] Markus Raffel. Background-oriented schlieren (bos) techniques. *Experiments in Fluids*, 56:60:1–17, 2015.

[10] M. J. Hargather and G. S. Settles. A comparison of three quantitative schlieren techniques. *Optics and Lasers in Engineering*, 50:8–17, 2012.

[11] J. D. Anderson. *Modern compressible flow: with historical perspective*. McGraw-Hill, 2003.

[12] Anderson B. H. and Bowditch N.D. Investigation of inlet control parameters for an external-internal-compression inlet. techreport NACA RM-E58G08, National Advisory Committee for Aeronautics, Cleveland, Ohio, September 1958.

[13] Ames Research Staff. Equations, tables, and charts for compressible flow. Technical Report 1135, National Advisory Committee for Aeronautics, 1953.

[14] G B Whitham. *Linear and Nonlinear Waves*, chapter 9, pages 312–338. John Wiley & Sons, Inc., 1974.

[15] Helen D. Gordon Milton D. Van Dyke. Supersonic flow past a family of blunt axisymmetric bodies. techreport R-1, National Aeronautics and Space Administration, Moffett Field, California, December 1959.

[16] Robert V Owens. Aerodynamic characteristics of spherically blunted cones at mach numbers from 0.5 to 5.0. techreport TN D-3088, National Aeronautics and Space Administration, Washington, DC, December 1965.

[17] Mushtak Al-Atabi Abdulkareem SH. Mahdi Al-Obaidi. Effect of body shape on the aerodynamics of projectiles at supersonic speeds. *Journal of Engineering Science and Technology*, 3(3), December 2008.

[18] Hornady. 50 bmg 750 gr a-max match. https://www.hornady.com/ammunition/rifle/50-bmg-750-gr-a-max-match#!/, 2021.

[19] L. Venkatakrishnan and G. E. A. Meier. Density measurements using the background oriented schlieren technique. *Exp. Fluids*, 37(2):237–247, 2004.

[20] Hiroko Kato, Kenta Hamada, Masanori Ota, and Kazuo Maeno. Quantitative measurement of supersonic flow field around an asymmetric cone model with cgbos method and 3d-ct reconstruction. *Japanese Society of Experimental Mechanics*, 11:s153–156, 2011.

[21] K L Smith T B Fisher, M K Quinn. An experimental sensitivity comparison of the schlieren and background-oriented schlieren techniques applies to hypersonic flow. *Measurement Science Technology*, 30(6), May 2019.

[22] Defence Safety Authority. Proof of ordanance, munitions, armour and explosives. techreport, Ministry of Defence, November 2006.

[23] Kistler Group. Quartz high-pressure sensor for ballistic pressure measurement to 6000 bar. techreport 6215_000-043e-05.10, Kistler Group, strasse 22, 8408 Winterthur,Switzerland, 2010.

[24] Bisping B Backstein G., Bettermann P. *Handbook on Weaponry*. Rheinmetall GmbH, Dusseldorf, 1 edition, February 1982.

[25] Fickie K D Anderson R D. Ibhvg2 (interior ballistics of high velocity gun, version 2) – a user's guide. techreport, Army Ballistic Lab., Aberdeen Proving Ground, MD, July 1987.

[26] Relative burn rates from fastest to slowest. https://imrpowder.com/wp-content/uploads/2019/12/2020-burn-rate-chart.pdf, November 2019.

[27] Bin Wu, Jing Zheng, Qing tao Tian, Zhi qiang Zou, Xiao lei Chen, and Kai shuan Zhang. Friction and wear between rotating band and gun barrel during engraving process. *Wear*, 318(1):106–113, 2014.

[28] Eugene Hecht and Alfred Zajac. *Optics*. Addison-Wesley Publishing Company, Inc., December 1974.

[29] T.J. Atherton and D.J. Kerbyson. Size invariant circle detection. *Image and Vision Computing*, 17(11):795–803, 1999.

[30] Jessica Tobin. Quantitative schlieren measurement of explosively-driven shock wave density, temperature, and pressure profiles. Master's thesis, New Mexico Institute of Mining and Technology, 2014.

[31] Michel Bornert, François Hild, Jean-José Orteu, and Stéphane Roux. *Digital Image Correlation*, chapter 6, pages 157–190. John Wiley & Sons, Ltd, 2013.

[32] Jones E.M.C and Iadicola M.A., editors. *A Good Practices Guide to Digital Image Correlation*. International Digital Image Correlation Society, 2018.

[33] Pankaj S. Kolhe and Ajay K. Agrawal. Abel inversion of deflectometric data: comparison of accuracy and noise propagation of existing techniques. *Applied Optics*, 48(20):3894–3902, July 2009.

[34] Matthew M. Biss and Kevin L. McNesby. Laboratory-scale technique to optically measure explosive impulse for energetic-material air-blast characterization. Technical Report ARL-TR-6185, Army Research Laboratory, 2012.

[35] MathWorks. Matlab: Image processing toolbox. r2020a edition, 2020.

[36] N. Otsu. A threshold selection method from gray-level histograms. *IEEE Transactions on Systems, Man, and Cybernetics*, Vol. 9(No. 1):62–66, 1979.

[37] Jesse D. Tobin and Michael J. Hargather. Quantitative schlieren measurement of explosively-driven shock wave density, temperature, and pressure profiles. *Propellants, Explosives, Pyrotechnics*, 41:1050–1059, 2016.

[38] Rafael C. Gonzalez and Richard E. Woods. *Digital Image Processing*. Prentice Hall, Upper Saddle River, New Jersey, USA, 2002.

[39] Krauss Stephen Davenport William, J. Compressible aerodynamics calculator. http://www.dept.aoe.vt.edu/ devenpor/aoe3114/calc.html, March 2021.

[40] Carlton S. James. Boundary-layer transition on hollow cylinders in supersonic free flight as affected by mach number and a screwthread type of surface roughness. techreport, National Aeronautics and Space Administration, Washington, February 1959.

[41] H. H. Ku. Notes on the use of propagation of error formulas. *Journal of Research of the National Bureau of Standards*, 70C(4):263–273, December 1966.

[42] Berthold K.P. Horn and Brian G. Schunck. Determining optical flow. *Artificial Intelligence*, 17(1):185–203, 1981.

APPENDIX A

TECHNICAL SPECIFICATIONS FOR CONICAL PROJECTILES

A.1 Engineering Drawing

Conical projectile technical specification

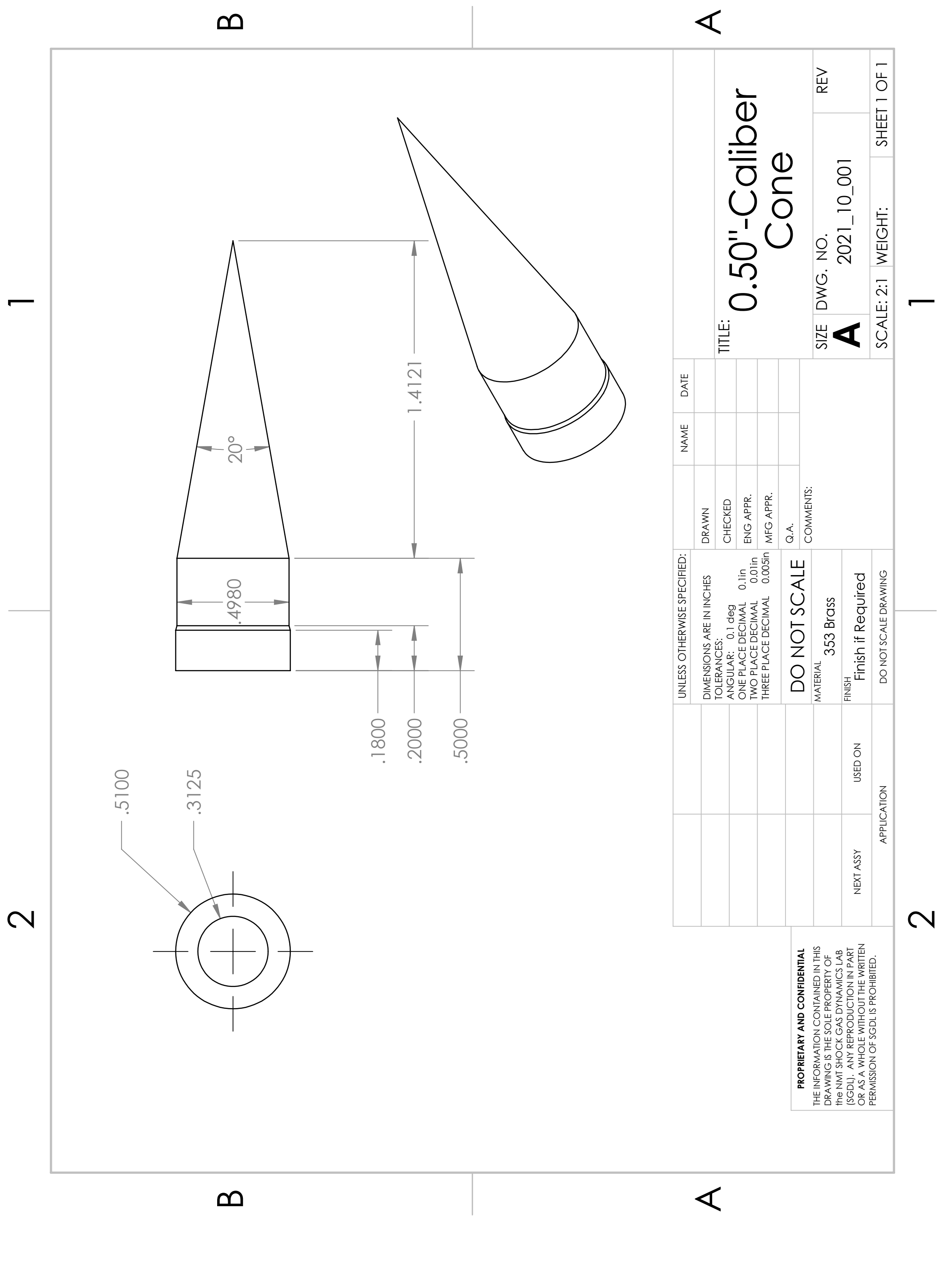

0.50"-Caliber Cone
TITLE:
SIZE A
DWG. NO. 2021_10_001
REV
SCALE: 2:1
WEIGHT:
SHEET 1 OF 1
1.4121
20°
.4980
.1800
.2000
.5000
.5100
.3125
UNLESS OTHERWISE SPECIFIED:
DIMENSIONS ARE IN INCHES
TOLERANCES:
ANGULAR: 0.1 deg
ONE PLACE DECIMAL 0.1in
TWO PLACE DECIMAL 0.01in
THREE PLACE DECIMAL 0.005in
DO NOT SCALE
MATERIAL 353 Brass
FINISH Finish if Required
DO NOT SCALE DRAWING
NAME
DATE
DRAWN
CHECKED
ENG APPR.
MFG APPR.
Q.A.
COMMENTS:
NEXT ASSY
USED ON
APPLICATION
PROPRIETARY AND CONFIDENTIAL
THE INFORMATION CONTAINED IN THIS DRAWING IS THE SOLE PROPERTY OF the NMT SHOCK GAS DYNAMICS LAB (SGDL). ANY REPRODUCTION IN PART OR AS A WHOLE WITHOUT THE WRITTEN PERMISSION OF SGDL IS PROHIBITED.

A.2 G-Code for Haas ST-20 Computer Numerical Control Lathe

The CNC g-code for the Haas ST-20 lathe is provided for recreation of the cones from 1″ stock material. Note that the perfect tip on the cones requires that the starting stock of 353 brass must be a 1″ stock of material. A cutting tool is custom ground to cut the sharp tip on the cones.

```
%
O00112 (50 Cal Cone from 1" Bar)
(Set end of bar 2.5" from face of chuck jaws)
G00 G18 G40 G80 G97 G99
N1 ( Turn Rough1 )
G54 (SET Z 2.673 FRONT OF STOCK)
T0202 (VNMG 332 35DEG SQR HOLDER)
G97 S2000 M03
G99 G18 G00 Z.1571
M08
X1.1141
G01 X.9 Z.05 F0.008
Z-1.9771
X1.
X1.0141 Z-1.9701
G00 X1.2141
Z.0571
X.8246
G01 X.8105 Z.05
Z-1.9771
X.9
X.9141 Z-1.9701
G00 X1.1141
Z.0571
X.7351
G01 X.7209 Z.05
Z-1.2193
X.796 Z-1.4321
G03 X.798 Z-1.4436 R.0665
G01 Z-1.7339
X.8044 Z-1.7445
G03 X.81 Z-1.7636 R.0665
G01 Z-1.9771
X.8105
X.8246 Z-1.9701
G00 X1.0246
Z.0571
X.6456
G01 X.6314 Z.05
Z-.9655
X.7209 Z-1.2193
X.7373 Z-1.2251
G00 X.9373
Z.0571
```

```
X.556
G01 X.5419 Z.05
Z-.7116
X.6314 Z-.9655
X.6478 Z-.9712
G00 X.8478
Z.0571
X.4665
G01 X.4524 Z.05
Z-.4577
X.5419 Z-.7116
X.5583 Z-.7173
G00 X.7583
Z.0571
X.377
G01 X.3628 Z.05
Z-.2039
X.4524 Z-.4577
X.4687 Z-.4635
X.4987
G00 X.6687
Z.06
X.3326
G01 X.2733
Z.05
X.3628 Z-.2039
X.3792 Z-.2096
G00 X.6922
Z.0632
X.2323
G01 X.2208 Z.055
X.7467 Z-1.4364
G03 X.748 Z-1.4436 R.0415
G01 Z-1.7376
X.7565 Z-1.7517
G03 X.76 Z-1.7636 R.0415
G01 Z-2.0021
X.937
X.9511 Z-1.9951
G00 X1.1511
G00 Z0.1
X0.15
G01 F0.005 Z0.
G00 Z0.1
X0.1
G01 Z0.
G00 Z0.1
X0.05
G01 Z0.
G00 Z0.1
X0.
```

```
G01 Z0.
G00 X11. Z5.
M01

N2 (FINISH)
G54
T202
G97 S2000 M03
G99 G18 G00 Z0.1
Z.0822
X.2105
G01 X0. F0.002
Z0.
X0.02
G01 X.0105 Z-.0178 F0.002
X-.001 Z-.026
X.497 Z-1.4382
G03 X.498 Z-1.4436 R.0315
G01 Z-1.739
X.5073 Z-1.7546
G03 X.51 Z-1.7636 R.0315
G01 Z-1.9436
X.697
X.7111 Z-1.9366
G00 X.9111
X11. Z5. M09
M01

N3 (TIP CLEAN UP)
G54
T707 (SHARP 35 DEGREE PROFILING TOOL)
G97 S2000 M03
G99 G18 G00 Z0.1 M08
X0.0
Z0.0
G01 X0.0355 Z-0.10 F0.0005
G00 X11.0 Z5.0

M09 N4 ( Cut Off1 )
G54
T0505 (0.118W CUT-OFF BLADE)
G97 S2000 M03
G99 G18 G00 Z-1.9301 M08
X1.1
G01 Z-2.0301 F0.002
X0.25
G00 X1.1
X11. Z5. M09
M01
M05 G28
M30


%
```

APPENDIX B

BALLISTIC LIGHT-GATE TRIGGER

B.1 Wiring Diagram

The ballistic light gate contains an 850nm light emitter LED and a 850nm photo-diode which drops a 5V Transistor-Transistor-Logic (TTL) signal high to low. The response time is purported of 60ns which is more than sufficient for timing applications for ballistics. The emitter and photo-diode both run on a constant DC source of +5V provided from a simple DC power supply. An electrical wiring diagram for the light gate is shown on Fig. B.1. The light gate outputs a high $\geq$ 3.3V signal during standby operations.

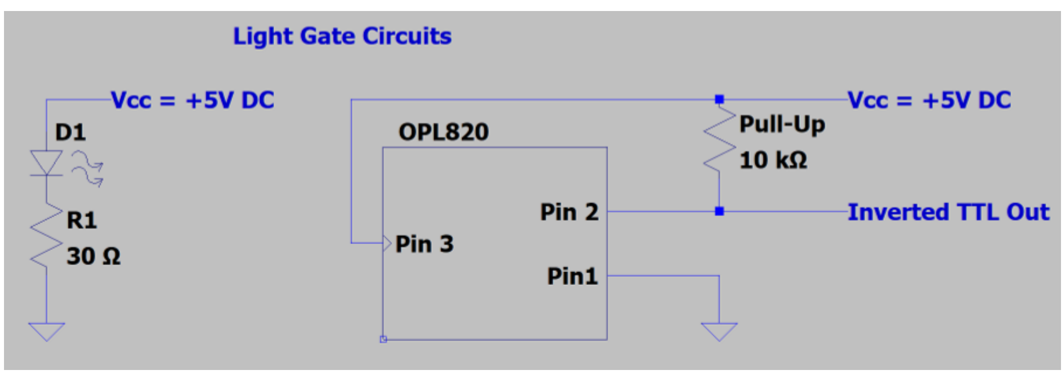

Figure B.1: left: Wiring schematic for sender LED of light gate right: Receiver photo-diode for ballistic chronograph

B.2 Setup and Operational Best Practices

The light gate trigger has 3D printed holder which allows for the photo-diode and the LED to be held by an optical post holder. A magnetic mount with angle post clamps for optical posts is used to freely suspend the light gate above and below the shot line of the gun. When the supersonic bullet breaks the beam of the LED, the photo-diode drops the +5V TTL below the 3.3 V minimum for a TTL. The falling side of this output is sent through an RG-58 coaxial BNC cable to the Stanford Research Systems DG535 delay generator. The distance between the IR LED and the photo-diode changes the sensitivity for the trigger, and as such is placed $\approx$ 20 cm (8 in) from the LED such that the gate will be sensitive to the projectiles passing through the IR light. The Stanford Research Systems' DG535 delay generator controls the triggering for the high-speed camera and Specailised Imaging SI-LUX spoiled coherence laser illumination source.

APPENDIX C

SI-LUX LASER OPERATIONS

The SI-LUX user manual is written for the operation of the

C.1 SI-LUX General Setup for Photron, and Phantom Cameras

C.1.1 Important

- Do not overexpose the camera. Make sure to start out at the lowest exposure and use a neutral density filter. Adjust the delay before changing the exposure to increase light. (See section C.2.2)
- Make sure to use laser safety glasses rated to OD 5 at the correct wavelength of 640 nm.
- Make sure all doors in the room are locked and laser safety signs are on all the doors.
- Do not exceed a 5V TTL signal on any of the BNC cables to protect electronics, use the oscilloscope to check voltage.
- Do not exceed 30 μs of laser on time. Double check Calculations done with Eq. C.1.

C.1.2 Materials Needed

The items needed to setup the laser for an event trigger are listed below

- SI-LUX laser including laser safety unit and liquid light guide
- SugarCUBE
- Specialised Imaging 1 channel delay generator
- One or two laptops with an Ethernet connection

- Stanford Research Systems DG535 box
- Trigger input
- Oscilloscope
- High-speed camera of choice
- 3 Ethernet cables
- At least 4 RG-58 BNC cables

C.1.3 General Setup Using Camera Triggering

1. Set up an optical system by using the liquid light guide connected to the SugarCUBE. An optical rod holder can be used to secure the liquid light guide

Figure C.1: Light Guide Mount

2. Connect power connectors to all devices
3. Connect green cable from laser safety box to laser
4. Turn on all devices
5. Connect the camera to laptop and set input/output ports on the camera's respective software (see section C.2.1 for setting up output ports. For Photron cameras, outputs need to be set on each start-up of PFV)
6. Set delay in SI-LUX software (see section C.2.5 for software installation and section C.2.2 for information on setting delay)
7. Set laser pulse width to in SI-LUX software (see section C.2.3 for information on selecting pulse width)
8. Connect trig out on SI delay generator to sync on laser safety unit using a BNC cable
9. For Photron, connect port assigned to REC POS terminal on the camera to Stanford box trigger. For Phantom, the port used is "TRIGGER"

10. Connect A⊓B terminal on Stanford box to ENABLE terminal on the SI Delay Generator

11. For Photron, connect the port assigned to EXPOSE POS on the camera to TRIG IN on SI Delay Generator. For a single Phantom, use the "F-SYNC" port

12. Connect Ethernet cables from the camera and the SI Delay Generator to the switch, then connect the switch to the computer. If both the SI Delay Generator and the camera do not work with the same computer, a separate computer can be used for each

13. Set the total pulse duration on the Stanford box for the duration of the event (keep in mind not to exceed 30 μs of laser on time). Use Eqn. C.1 for setting the Total Event duration. See Sec. C.2.4 instructions on setting a pulse duration

$$Total\ Event\ Duration = \frac{30\ \mu s}{Laser\ Pulse\ Width * FPS} \tag{C.1}$$

14. Switch the SugarCUBE with the laser without moving the liquid light guide. The same liquid light guide used for the SugarCUBE should be used for the laser. Don't use excessive force when plugging light guide into laser

15. To avoid overexposing the camera use a neutral density filter. Set the camera to the highest exposure from the selected frame rate as long as it is less than 20 μs

16. Ensure delay generator is connected by looking at the bottom left of the SI-LUX software, as shown in Fig. C.2

17. For Photron cameras, set the level in SI-LUX software to 2.5V

18. Ensure all BNC's match the wiring diagram in Fig. C.3 if using the camera to trigger

    *Outputs on Camera
    Photron: Gen Out 1

    **Output on Camera
    Photron: Gen Out 2

19. Set camera trigger to start

20. Put on laser safety glasses, arm SI pulse generator in the software, and turn key on the laser safety unit to on

21. Record video

22. Make sure to disarm the laser by turning the key to the "OFF" position and the SI-LUX

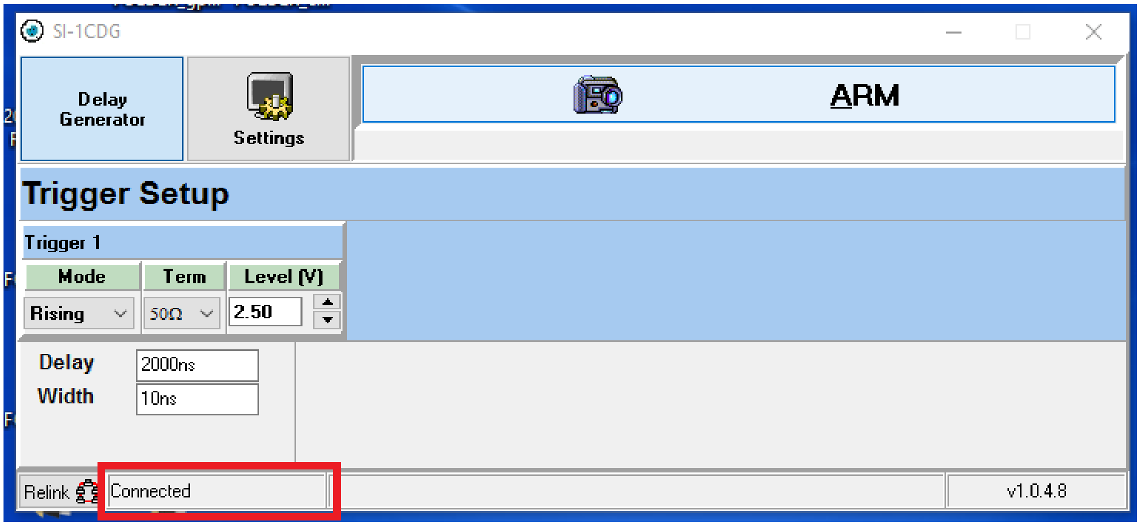

Figure C.2: SI-LUX User Interface Displaying ”Connected”

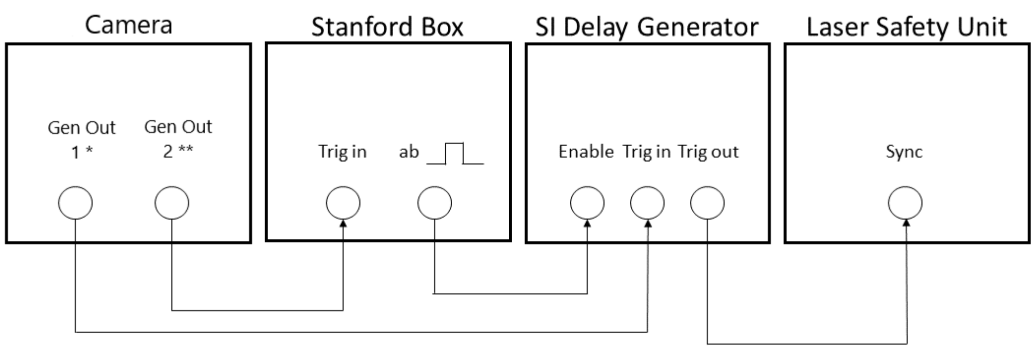

Figure C.3: BNC wiring diagram

C.1.4 General Setup Using Stanford Box Triggering

1. Follow setup from step 1 through 8 in Sec. C.1.3
2. Connect port assigned to REC POS terminal on Photron camera to ”A” port on the Stanford Box. For Phantom, the port used is ”TRIGGER”
3. Connect A⊓B terminal on Stanford box to enable terminal on the SI delay generator
4. Connect port assigned to EXPOSE POS on Photron camera to trig in on SI delay generator, for Phantom: use the ”F-SYNC” port
5. Connect Ethernet cables from the camera and the delay generator to the switch, then connect the switch to the computer. If both the delay generator

and the camera do not work with the same computer. A separate computer will be needed for each.

6. Set the total pulse duration on the Stanford box for the duration of the event (keep in mind not to exceed 30 μs of laser on time). Use Eqn. C.1 for setting the Total Event duration. See section C.2.4 instructions on setting a pulse duration.

$$Total\ Event\ Duration = \frac{30\mu s}{Laser\ Pulse\ Width * FPS} \tag{C.2}$$

7. Switch the SugarCUBE with the laser without moving the liquid light guide. The same liquid light guide used for the SugarCUBE should be used for the laser. Don't use excessive force when plugging light guide into laser.

8. To avoid overexposing the camera use a neutral density filter. Set the camera to the highest exposure from the selected frame rate as long as it is less than 20 μs.

9. Make sure delay generator is connected by looking at the bottom left of the SI-LUX software, as shown in Fig. 1.

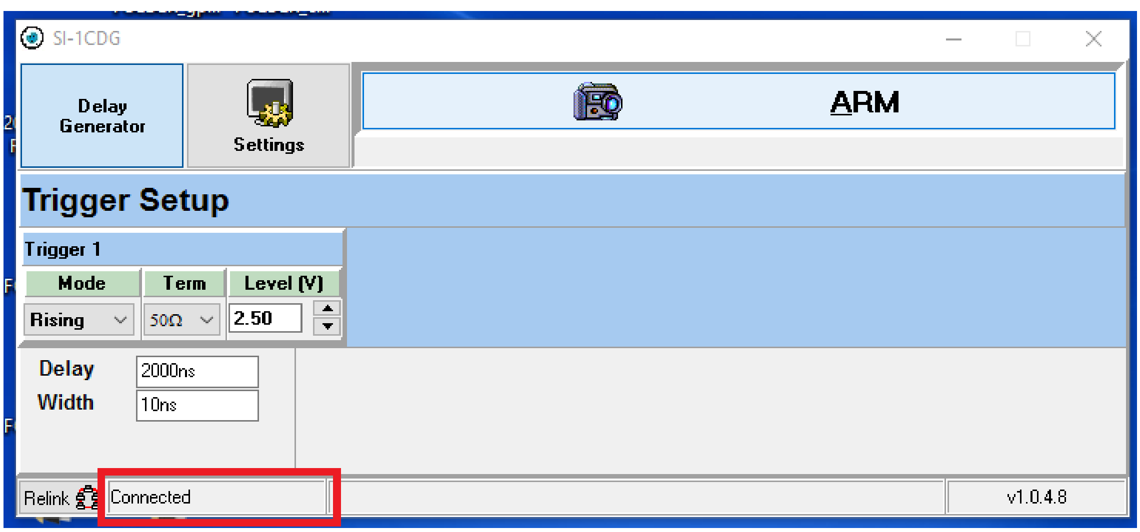

Figure C.4: SI-LUX User Interface Displaying "Connected"

10. For Photron and Phantom cameras, set the level in SI-LUX software to 2.5V

11. Make sure all BNC's match the wiring diagram in Fig. C.3

*Ports on Camera
Photron: Gen Out 1
Phantom:

**Ports on Camera
Photron: Gen Out 2
Phantom:

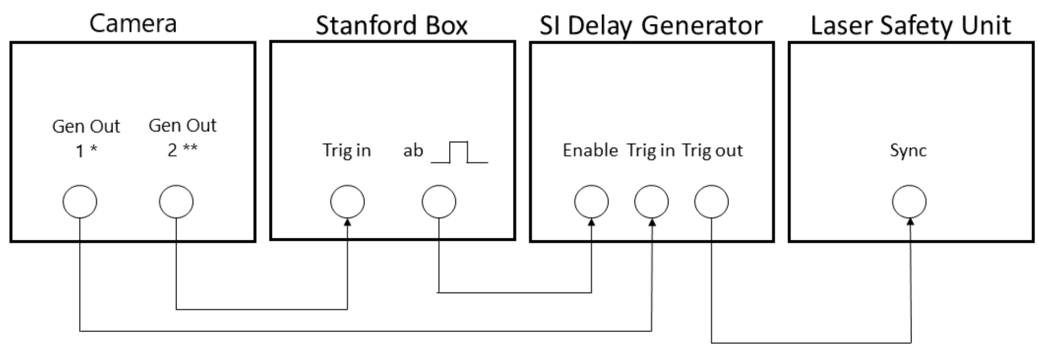

Figure C.5: BNC wiring diagram

12. Set camera trigger to start.
13. Put on laser safety glasses, arm SI pulse generator in the software, and turn key on the laser safety unit to "ON"
14. Set the trigger on the Stanford Box to Single Shot
15. Press the "EXC" button on the Stanford Box to trigger the event
16. Make sure to disarm the laser by turning the key to the "OFF" position and the SI-LUX

C.1.5 General Setup Using an External Trigger

1. Follow setup in subsection C.1.4 from step 1 to 10.
2. Connect the external trigger to "TRIGGER" port on the Stanford Box. Make sure to use an attenuator on the line. (Do not exceed a 5V TTL signal to the Stanford box. Use the oscilloscope to check voltage)
3. Make sure all BNC's match the wiring diagram in Fig. C.6 .

*Ports on Camera Photron: Gen Out 1 Phantom:	**Ports on Camera Photron: Gen Out 2 Phantom:

4. Set camera trigger to start.
5. Make sure the camera is ready to receive a trigger signal.
6. Set the trigger on the Stanford Box to External.

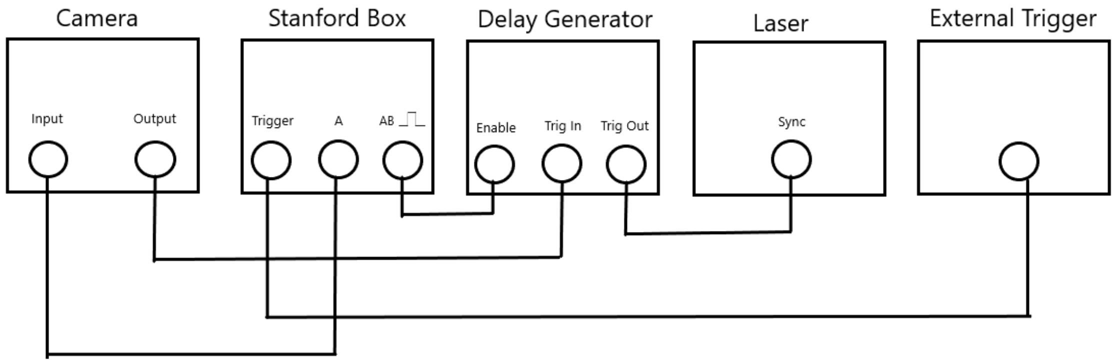

Figure C.6: BNC wiring diagram

7. Put on laser safety glasses, arm SI pulse generator in the software, and turn key on the laser safety unit to on.

8. Trigger the event

9. Make sure to disarm the laser by turning the key to the ”OFF” position and disabling the arm button on the SI-LUX software.

C.2 Advanced Setup

C.2.1 Camera I/O

Setting I/O ports correctly is important for laser illumination. The following steps discuss the settings for both Photron and Phantom cameras

Photron

1. Plug in camera and make sure it is connected to the PFV software.

2. Click on camera options on the right side of the user interface.

3. On the menu tree click on I/O

4. On the I/O menu, select ”EXPOSE POS” for ”GENERAL OUT 1”. Select ”REC POS” for ”GENERAL OUT 2”. Click Apply, then click OK.

Phantom

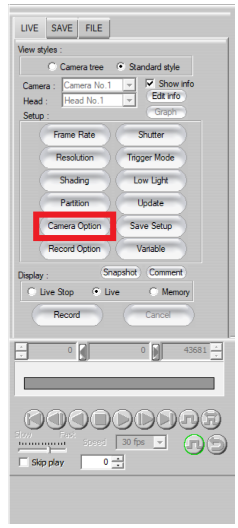

Figure C.7: Location of "Camera Options" on PFV User Interface

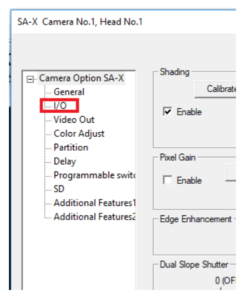

Figure C.8: Location of "I/O" on Camera Option Menu

C.2.2 Setting Delay

The delay setting in the SI-LUX software is the time it takes to output the laser pulse after receiving the signal from the Standford box.

C.2.3 Setting Pulse

The pulse width is the time the laser is on for each frame. If the pulse width is less than the exposure time than the pulse width is effectively the exposure. Less exposure time reduces motion blur, typically in our work we want the least motion blur possible. The laser is very bright and the smallest pulse width of 10 ns usually provides enough light. It is recommended to always start at 10ns and go up to protect the camera sensor from overexposure.

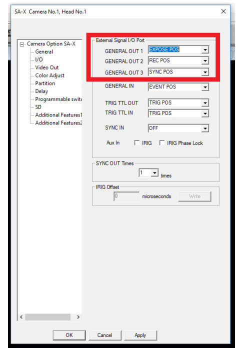

Figure C.9: Location of ”Camera Options” on PFV User Interface

C.2.4 Setting Stanford Box Pulse Duration

The Stanford box A⊓B positive pulse duration is the time difference between the time of channel a and the time of channel b.

1. Press the ”Delay Button” until the screen displays what is shown in Fig. C.10 and input the ”Total Event Duration” value using the arrows on the number pad.

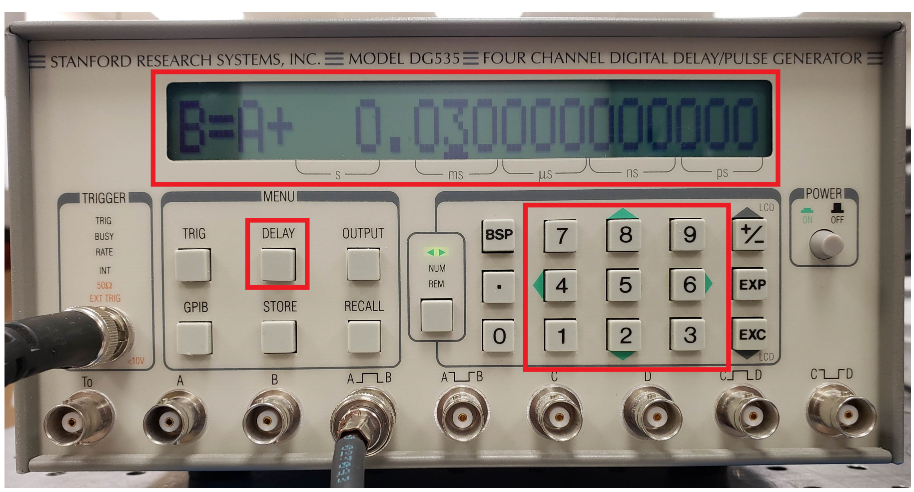

Figure C.10: Stanford Box Delay Display

2. Press the ”Trig” button and select Ext using the arrows on the number pad
3. Press the ”Output” button and select A⊓B positive using the arrows on the number pad.

For more information check the Stanford box manual.

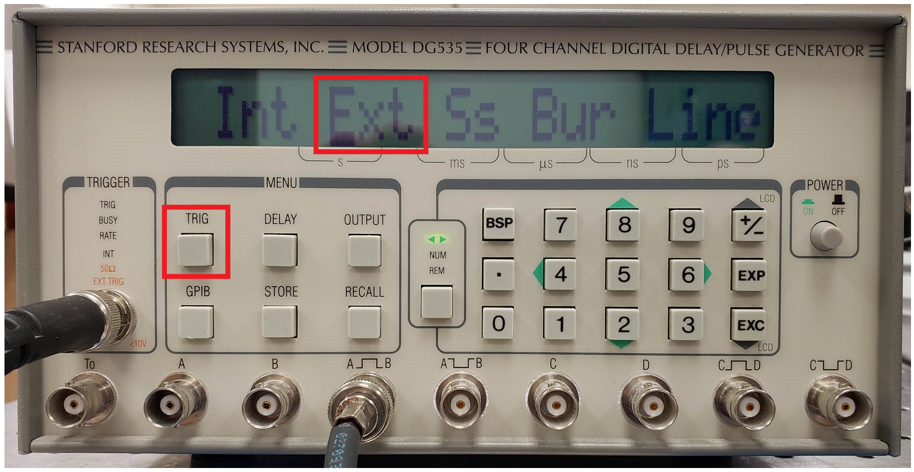

Figure C.11: Stanford Box Trigger Display

C.2.5 SI-LUX Software Setup

1. Install software using provided CD.
2. Change IP address of the Ethernet connection to 192.168.0.XXX where XXX must be between 2 and 49. Refer to the "SI-1CDG 1 Channel Delay Generator" Use Guide for more information on setting the IP address. If only using one computer for both the camera and the SI delay generator, is recommended to end the IP address with .2.
3. Open the SI-LUX software, then open the settings and set the IP address there to 192.168.0.73
4. Click the "ON/OFF' button under the "Output" section in the SI LUX User Interface. This button is partially hidden and will disappear once clicked.

C.3 Troubleshooting

C.3.1 The delay generator is not connecting

Possible Solutions

1. Click the "Relink" button on the bottom left corner of the SI-1CDG interface.
2. Make sure all equipment is on and BNC match the wiring diagram in Fig 2.
3. If just installed software and inputted IP address, restart computer.
4. Make sure that the hidden button is clicked

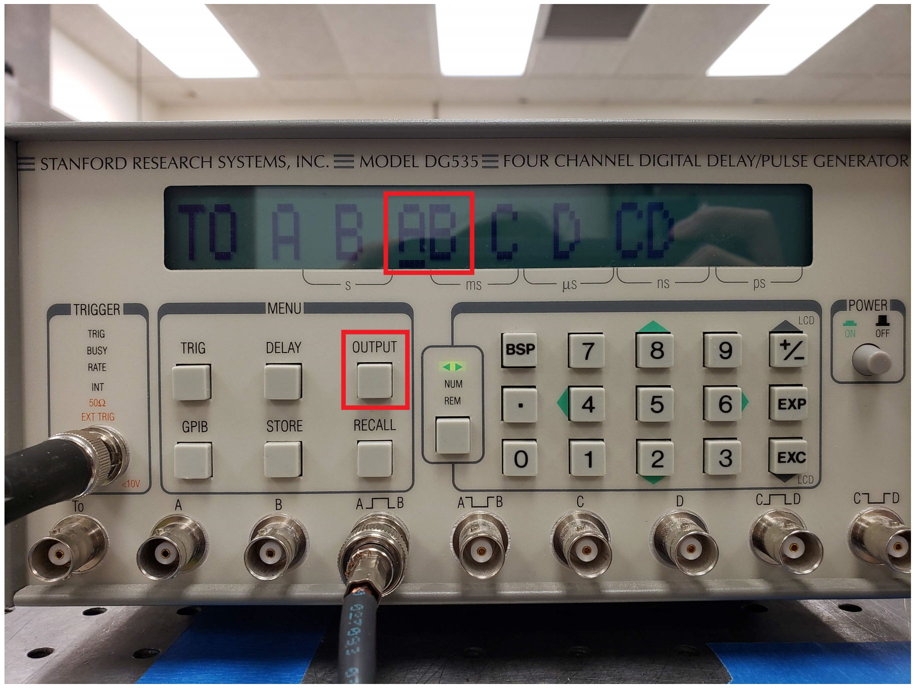

Figure C.12: Stanford Box Output Display

C.3.2 Flickering or Sudden Cutoff in Video

Possible Solutions

1. Make sure the output from camera to "Trig in" on SI Delay Generator.
2. Make sure the delay in SI-1CDG software in 55 ns.
3. Make sure the highest exposure is set on the camera for the selected frame rate as long as it is under 20 μs
4. If "Expose Pos" output is not available or c Since the Photron camera begins the image frame and opens the exposure at a later, time a delay is needed.The sync pos output on the camera outputs a 5V TTL signal for every frame. The exposure pos output outputs a 5V TTL signal every time the camera shutter opens. To find the correct delay for the camera, two BNC cables should be connected to the oscillope, one should be connected to the output on the camera assigned to the sync pos and the other to the output on the camera assigned to exposure pos. The oscilloscope should be set to 5V/div in the vertical direction, and 1/(frame rate) for the horizontal direction. with the camera on, there should be two pulses visible, the sync pulse will occur before the exposure pulse. Measure the time difference between the sync pulse and the exposure pulse. This value should be entered in to the SI software in the delay field. It is recommended to set the delay so that

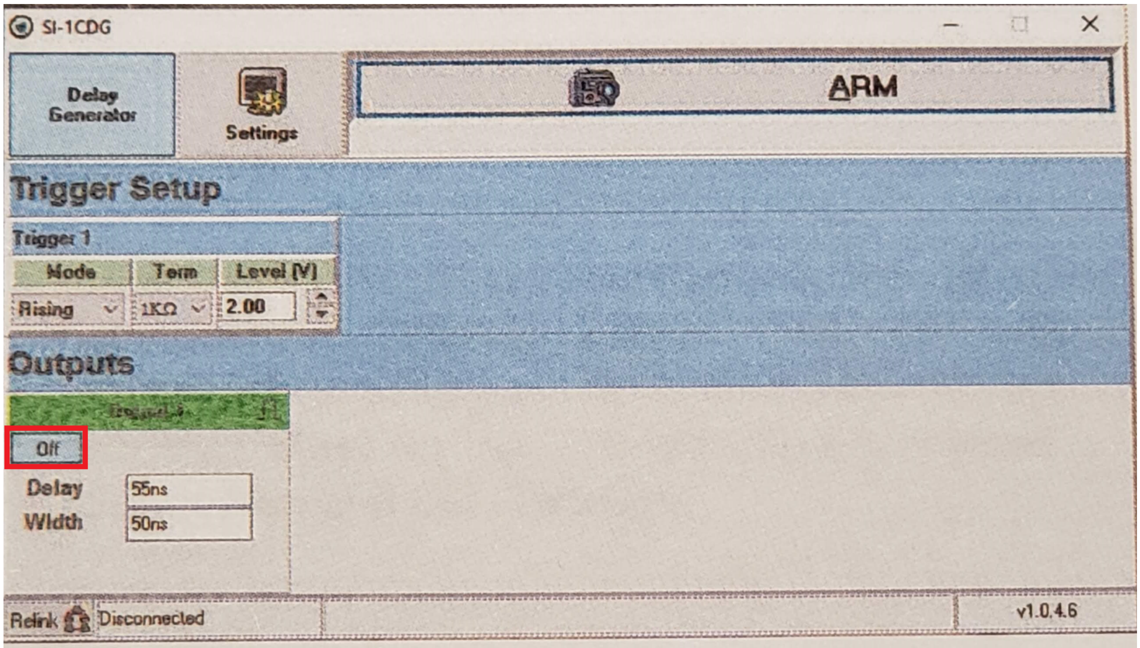

Figure C.13: Hidden "ON/OFF" Button on SI-LUX Inferface

it is well within the exposure pulse to avoid having some of the light clipped due to the light being on while the shutter is in the process of opening.

C.4 Appendix A: Dual Phantom Camera Testing

The following appendix is designed for the use of the dual Phantom testing utilizing the "F-Sync" pulse for the intended use rather than as a laser trigger input. A pigtail will have to be used with the dual Phantom testing utilizing the "Strobe" output. The "Strobe" output is a pulse which staggers the exposure pulse, so the laser setup will have to be modified to use the "Falling" edge of the pulse that the delay generator receives from the Phantom. If dual cameras are being used with the Phantom V711's note that the laser pulse width will likely have to be modified to utilize a 20 ns pulse since the V711 is not as light sensitive as other cameras like the Photrons. See Fig. C.14 for the general setup for utilizing an external trigger.

C.4.1 Synchronizing the Phantoms

PCC is less intuitive than PFV for the Photrons, so the synchronization procedures do not have a set of menus which walk the user through the synchronization of the Phantoms. The procedure involves using a BNC cable to connect

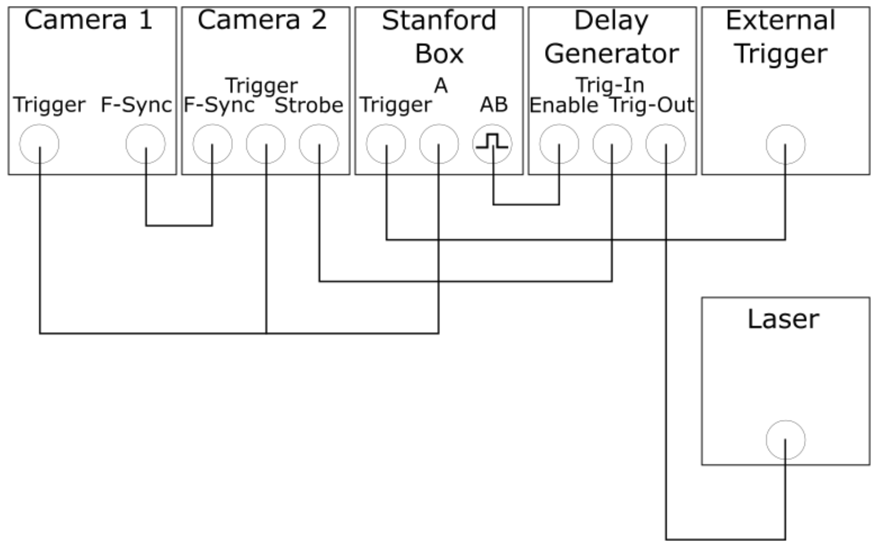

Figure C.14: Dual Phantom Camera Setup

the "F-Sync" terminals of each camera together. In the PCC software, the following image Fig. C.15 displays the changes that need to be made to ensure that the two cameras will synchronize and record the same frames. The "Advanced Settings" tab contains the information for synchronization of the cameras. The master camera's "External Sync" settings should have the "Sync Imaging:" drop-down menu set to "Internal". For the slave camera, the "Sync Imaging:" should be set to "External". On the slave camera, the value for the Master camera serial field should have the serial number of the master camera input in it. **Note:** The serial number of the master camera can be found on the side of the camera next to the location where the camera's IP address can be found.

If using cameras with different buffer sizes, one must change the trigger location such that the two cameras will begin recording when the trigger signal is received. By default, PCC synchronize the cameras' end frames. The "Image Range and Trigger Position" location should be set to the maximum value in the drop-down if the slave camera's buffer is smaller than the master's buffer. Additionally, when using the laser illumination, the shutter speed doesn't matter, so it is advantageous to keep the "Exposure Time" set to the maximum value as shown in Fig. C.15.

C.4.2 SI-LUX Software Setup

The general setup for the SI-LUX software utilizes the rising edge of the exposure pulse from the camera as well as 50Ω termination shown in Fig. C.2.5.

The strobe pulse form the Phantom straddles the typical exposure pulse, so the settings for the SI-LUX software should be set to see the falling edge rather than the rising edge of this pulse to synchronize the laser illumination with the camera's shutter being open. The default pulse width for the SI-LUX is a 10*ns* pulse width, which is what the exposure of the camera will be forced to. If using two cameras a good rule of thumb is to use 20*ns* pulse width if using the liquid light guide and either the bifurcated light guide or the beamsplitter as the main illumination source/splitting setup. If adding an iris and a condenser lens, the usage of a 80*ns* pulse width is appropriate with the Phantom V711's.

The delay to set the Stanford for the AB pulse can be obtained using the Frame Rate Excel spreadsheet by imputing the frame rate of interest as well as the pulse width necessary for proper illumination. With these additional settings for the Phantom cameras, the cameras should be setup to record using the SI-LUX and return temporally consistent frames.

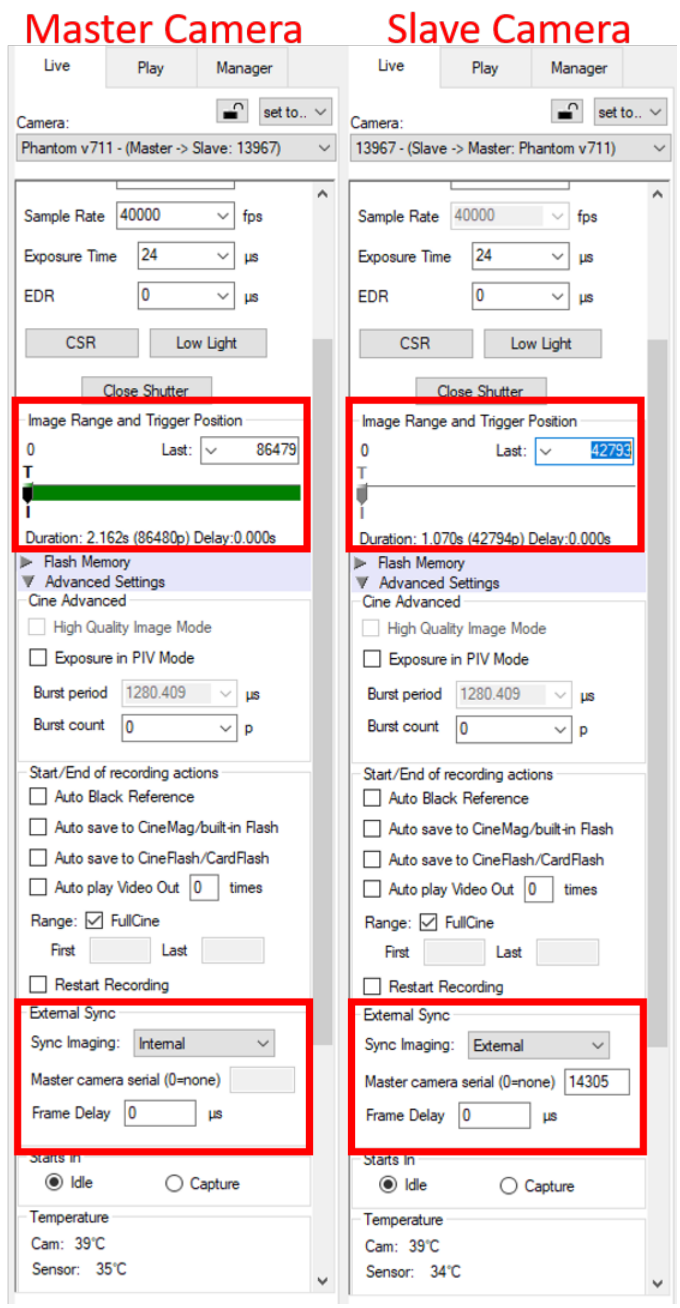

Figure C.15: PCC relevant settings change for master and slave testing.

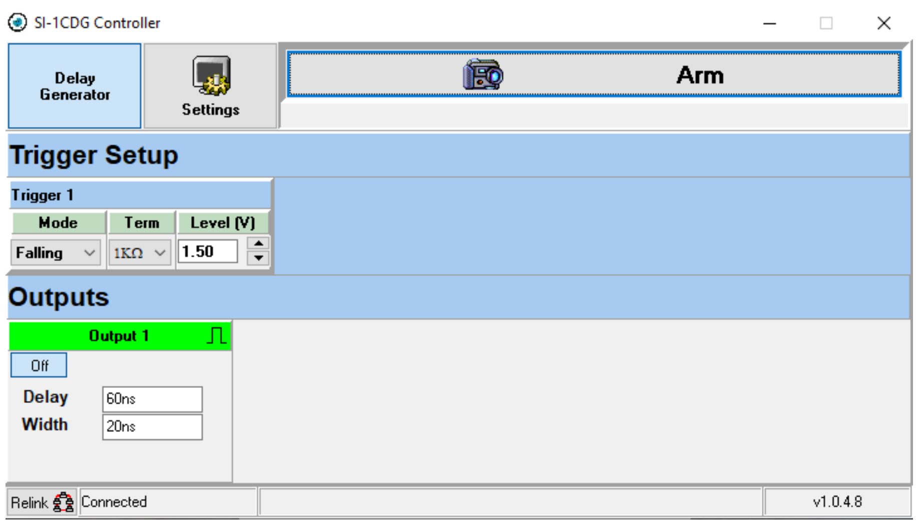

Figure C.16: SILUX software settings for two Phantom camera testing. Note that 20ns pulse width is for obtaining enough light such that both cameras have sufficient light.

APPENDIX D

RESEARCH PLAN FOR BALLISTIC LAUNCH OF PROJECTILES

The following is the research plan utilized for the ballistic launch of projectiles from the PDGS

Research Project Summary:

The Shock and Gas Dynamics Laboratory (SGDL) is studying the density variation around ballistically launched projectiles of varying geometries. The purpose of the testing described here is to visualize and perform quantitative measurements using schlieren photography for density variation characterization.

High velocity ballistic experiments will be performed projectiles of various size, shape, and composition. The projectiles will be launched and caught using a sand catch in accordance with EMRTC Test Plan TP-19-25: 50 Cal Match Ammunition Testing. High speed schlieren imaging will leverage the Specialised Imaging SI-LUX 640 spoiled coherence laser illumination source. Where applicable, projectiles will be held in 3D printed or machined sabots and launched at velocities up to 2km/s. The launching of the projectiles will be performed using SGDL's universal receiver (UR) and various powder gun barrels located at the Ballistics Sciences Laboratory (BSL). A cut-down 50 BMG brass cartridge will be used to hold the powder charge and percussion primer when using 50, 55, 65, and 75 caliber systems. Other commercial cases will be used where appropriate. Commercial smokeless powders will be used for these powder charges. The IBHVG2 program will be used for predicting gun performance before a powder load is utilized to ensure developed gas pressure remains within the gun system, projectile, and sabot design specifications. Testing at the BSL and operation of the gun system will be in accordance with the Gun Start of Day and Operational Procedures attached at the end of this document (attachment 6 and 7 respectively).

Energetic Materials, Chemicals, or Hazardous Materials Involved:

- Commercial smokeless powders
- 50 BMG CCI #35 primers

Location of Operations:

- All testing will be conducted at the BSL
- Sabot assembly with projectiles (where applicable) will be performed offsite at the SGDL research lab L4 (EMRTC chemistry labs)

Material Storage Requirements:

- Smokeless powder will be stored in accordance with EMRTC ordinance requirements
- Projectiles do not require special storage considerations

Disposal Requirements:

- Any spilled smokeless powder will be collected and determination made if still usable:
    - If powder is still usable, it is not considered waste and will be used or stored as applicable and per regulatory requirements
    - Powder deemed not suitable for use in the gun system will be properly containerized in a designated container and stored as applicable and per regulatory requirements. No disposal of powder is required for this testing

Required Personnel:

- Operation of the gun system requires a minimum of two personnel (Gun Operator and Safety)
- SGDL personnel may fill the role of Test Engineer, Gun Operator, and/or Safety

- At least one EMRTC employee or Dr. Hargather must be present during gun operation as either the Test Engineer, Gun Operator, or Safety. The present EMRTC employee must be either an Ordnance Gunner or an Engineer 1 or higher.
- Personnel Limits – A maximum of three essential personnel may be present in the Firebooth. All non-essential personnel will be located in the Visitors and Instrumentation Observation Loft during operation of the gun system unless prior approval has been granted by the Safety Office

Personal Protective Equipment (PPE):

- Safety glasses and hearing protection will be worn by all personnel present during loading and firing of the gun system
- Laser safety glasses will be worn when the SI-LUX system is armed (see callouts in Attachment 7) (OD +5 at 640nm)
- Hardhats and steel toe boots will be worn by those lifting and unloading the sand catch when applicable
- See Attachment 2

Equipment Needed:

- Gun system
- 50 BMG reloading press
- Scale with tenth of a grain resolution (milligram resolution)
- Working Ventilation System
- Fire Extinguishers. Minimum requirements: One Class ABC fire extinguisher
    - One class D fire extinguisher if performing testing using metals which could combust (Aluminum or Magnesium)
    - It will be noted that in the event of a fire all personnel are to evacuate the BSL and contact campus police. No students shall fight any fire.
- Instrumentation as needed and provided by SGDL

Firing System Schematic:

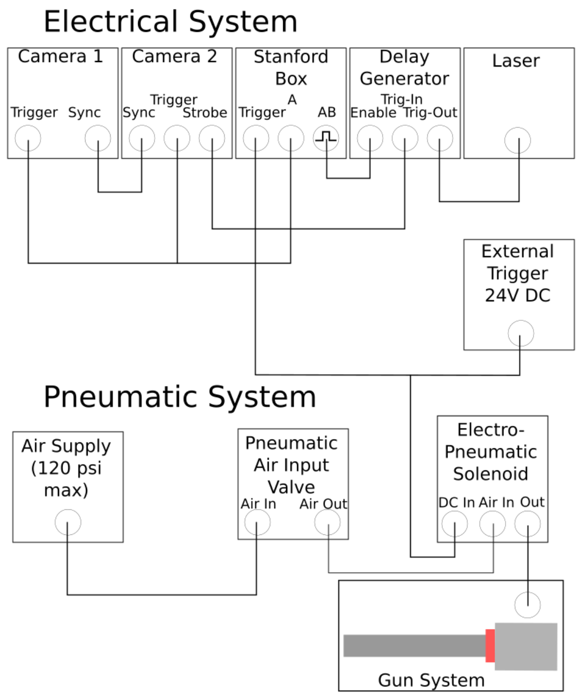

Planned Test Matrix:
Testing will encompass a variety of conical projectiles over an extended period of time. A test matrix will filed with the Safety Office and on file at the BSL prior to the start of each day of testing

Planned Testing Schedule or Duration of Project:
Testing may take place anytime Monday through Friday during normal EMRTC Field Lab operation hours.
This program is expected to have at least a 3-year duration.

References:
Include all references pertinent to the project

- SOP 101, Health and Safety
- SOP 103, Industrial Safety
- SOP 104, Laboratory Safety and Operations
- SOP 402, Emergency Action Plan
- SOP 403, Risk Management
- SOP 404, Hazardous Waste

Attachments:

1. Job Hazard Analysis
2. PPE Selection
3. Site Closure
4. Safety Data Sheets
5. Tailgate Briefing Form
6. Gun Start of Day Log
7. Gun Operational Procedures
8. Revised sandcatch cleaning operation procedures

Attachment 1

Job Hazard Analysis

Attachment 2

PPE Selection

Attachment 3

Site Closure

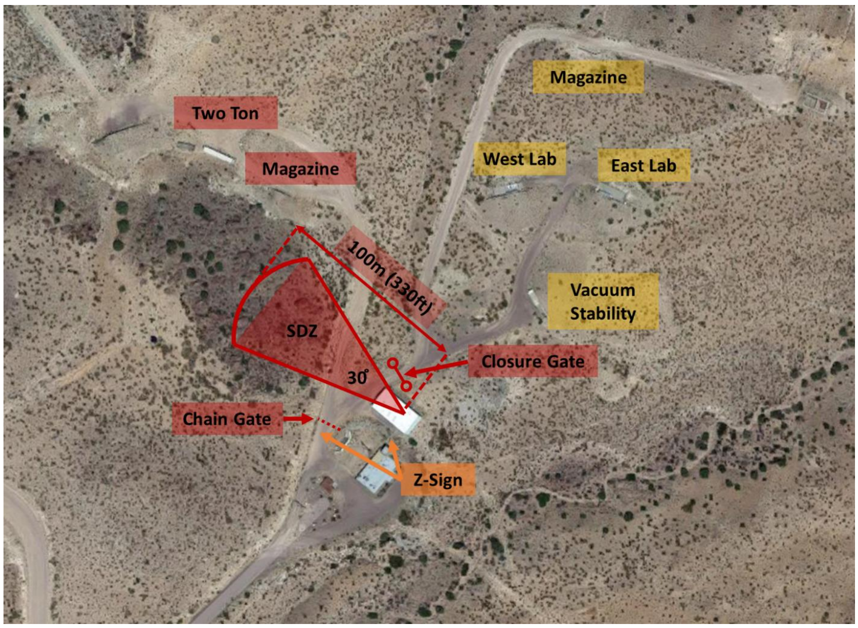

Site Closure

The following site closure shown in the map above will be observed:

1. Two Ton and the Torres facility magazine north west of the BSL building will be cleared and closed to personnel during testing
2. West Lab, East Lab, Vacuum Stability and the Torres facility magazine north of the BSL building will be open to personnel, but the personnel will remain behind the closure gate during testing. The Gun Operator is responsible for ensuring personnel at the listed facilities understand the closure and is responsible for providing these personnel clearance to enter or exit
3. The gate to East and West Labs will be closed.
4. The chain gate at the start of the access road leading to the BSL and lower Torres facilities will be closed
5. A Z-sign will be placed in front of the chain gate at the start of the access road leading to the BSL and lower Torres facilities as shown
6. A Z-sign will be placed at the top of the exterior staircase connecting the main Torres building to the BSL building
7. Personnel may work in the main Torres building during testing

Surface Danger Zone (SDZ)

The powder gun system is mounted in a fixed position with the barrel axis horizontal to the ground plane and the barrel bore 1.23 meters (48.5 inches) above the ground surface. A 50 caliber conical projectile travelling at 2km/s (6600ft/s) was found to demonstrate the farthest fly out distance of the projectile shapes and sizes to be tested at the maximum theoretical muzzle velocity. This maximum fly out distance was calculated to be 770 meters (2530 feet) for the fixed horizontal orientation of the gun barrel. With the applied engineering controls, the surface danger zone (SDZ) for testing at the BSL with the powder gun system is reduced to a 100 meters (330 feet) radius with a 30-degree arc as shown in the site closure map above. The applied engineering controls to reduce the SDZ are as follows:

1. The powder gun is fixed to a test stand. This test stand ensures the gun's axis is horizontal to the ground to mitigate over shoot of projectile stops and the gun's axis is oriented parallel to the building NW centerline to minimize risk of projectiles missing projectile stops
2. Two primary projectile stops are employed to restrict potential projectile fly out to no more than 100 meters (330 feet):
    a. The primary projectile stop is installed down range of the gun system at the NW end of the BSL building. This stop is nominally 24" high by 24" wide by 36" deep and consists of a solid fill of dry sand. The primary stop will be no more than 15.15 meters (50 feet) from the muzzle of the gun system to minimize the possibility of a projectile missing the stop due to vertical or horizontal drift during flight
    b. The secondary projectile stop is the earthen hill directly behind the primary projectile stop. This hill starts approximately 57.6 meters (190 feet) from the gun emplacement and rises approximately 45.5 meters (140 feet) above the gun emplacement. This secondary stop ensures any projectiles that miss the primary projectile stop due to vertical or horizontal drift are restricted to a horizontal fly out of no more than 100 meters (330 feet)

Attachment 4

Safety Data Sheets

Attachment 5

Tailgate Briefing Form

Attachment 5

NEW MEXICO TECH
ENERGETIC MATERIALS RESEARCH AND TESTING CENTER

Tailgate Briefing Form

TEST INFORMATION

Date:		Time:		Briefed By:	
Site:				Test Title:	
Test Engineer:				Safety:	
Gun Operator:					

WEATHER

Temp:		Wind:	Direction:		Precip:	
			Speed:		Cloud %:	

TOPICS COVERED

	Planned Site Activities		Chemical Hazards		Buddy Team Procedures
	Physical Hazards		PPE Required		Emergency Procedures
	Biological Hazards		Explosive Hazards		First Aid Procedures
	Heat/Cold Stress		Respiratory Hazards		Site Access / Clearances
	Site Communications		Decon Procedures		Other: Describe Below

Other:

BRIEFING ATTENDEES

Printed Name	Signature	Printed Name	Signature

By signing above, I certify that I have been breifed on and understand the information above.

NOTE: Tailgate briefings may need/have attachments from Ordnance or Instrumentation. Ensure all Tailgate Briefing forms are available if questions arise.

Attachment 6

Gun System Start of Day Log

START OF DAY LOG SHEET FOR GUN SYSTEM
(If already completed for the day of testing, go to gun system operation procedures)

1.1. Testing Conditions and Test Matrix:

1.1.1. Test Engineer: ___________________________

1.1.2. Gun Operator: ___________________________

1.1.3. Safety: ___________________________

1.1.4. Note date/time: ____

1.1.5. Barometric pressure (HPa):______________________________________

1.1.6. BSL inside temperature:____

1.1.7. Number of planned gun tests:__________________

1.1.8. Test matrix with powder loads to be used is attached
Test Engineer Signature:______________________

1.1.9. File Start of Day Log Sheet in designated folder at BSL

1.1.10. File Tailgate Briefing Form in designated folder at BSL

1.1.11. Pre-Test walkthrough completed with Dr. Hargather or EMRTC representative:
____

Attachment 7

Gun System Operational Procedures

The following operational procedures apply when using the SI-LUX 640 spoiled coherence 640nm laser illumination source for high speed imaging (henceforth referred to as "laser illumination source", "laser", or "SI-LUX"). The following modifications to test procedures apply to all projectiles. The testing procedure differs from RP-19-01 for reactive materials with modified and added steps included for SI-LUX laser operations

1. GUN PRETEST PROCEDURES

(If already completed and start of new test, go to 2)

1.1. **Start of Day**

1.1.1. Ensure Start of day log has been filled and filed with a copy of test matrix at BSL

1.1.2. Ensure Tailgate Briefing has been performed and form filed at BSL. Repeat if any new personnel arrive on site during testing. Gun Operator performs this review

1.1.3. Check that a Z-sign is on entry road to Torres facility and a Z-sign is in place at the start of the stairs to the Ballistics Science Building (BSL) according to site closure map

1.1.4. Check the Torres Main Building. If non-test related personnel are to be present in the Torres Main Building, inform them of testing to be performed in the BSL. Personnel may enter or exit Torres Main Building at will during testing in BSL.

1.1.5. Ensure Torres facilities North of BSL, labeled in red in the Site Closure figure are clear of personnel.

1.1.6. Check that the closure gate is closed according to the site closure map. Ensure personnel at West Lab, East Lab, Vacuum Stability and the Torres facility magazine north of the BSL building are aware that they are to remain behind the closure gate during testing and must obtain clearance from the Gun Operator to enter or leave the area

1.1.7. Review fire procedures with all personnel to be present during testing. Repeat if any new personnel arrive on site during testing. Gun Operator performs this review

1.1.8. Distribute PPE (hearing protection, laser safety goggles, and safety glasses) to all personnel to be present during testing

1.2. **System Hardware Checkouts (Firebooth, gun system, sabot stripper (where applicable), and ventilation system)**

1.2.1. Ensure power is off to Firebox (No green or red light) by disconnecting power supply

1.2.2. Ensure Firebox cage is locked

1.2.3. Approach gun from rear and switch Air Input Valve on air cylinder to “SAFE”

1.2.4. Visually confirm breech and barrel are clear. As required to conduct visual inspection, disconnect cocking sear, open breech, and/or remove Chamber Flag

1.2.5. Insert Chamber Flag into breech

1.2.6. Check lateral play in recoil carriage. If play in the assembly is found, discontinue testing until recoil carriage has been disassembled and all fasteners checked and appropriately tightened

1.2.7. Check that red barrel retainer nut is tight

1.2.8. Check play in the bolt handle assembly. If play in the bolt assembly is found, discontinue testing until all fasteners have been checked and appropriately tightened

1.2.9. Connect yellow airline to compressor or suitable compressed air supply (120psi main supply maximum)

1.2.10. Set regulator pressure on compressor or air supply between 80 and 120psi

1.2.11. Visually inspect sabot stripper for damage which could degrade operation and ensure sandbags are in place on bottom tray

1.2.12. Situate ventilation duct perpendicular to muzzle of barrel. Duct opening should be two feet from barrel exit. Turn on ventilation system

1.2.13. Visually inspect BSL building to ensure no equipment/hardware are in the line of fire of the gun system that is not designed to be so. Ensure all cleaning supplies and any flammables are safely stored behind the firing line

1.3. **Fire System Checkout**

1.3.1. Ensure that laser warning signs are posted on the East and West doors to BSL, place the door barricades across the East and West doors, note the laser operator as the gun operator

1.3.2. Ensure power to Firebox is disconnected, Firebox cage is locked, breech is open, Air Input Valve is set to “SAFE”, and Chamber Flag is inserted in breech

1.3.3. Pull air cylinder rod up to extend. Extend rod until it stops

1.3.4. Turn Air Input Valve to “ARM”

1.3.5. Return to Firebooth

1.3.6. Obtain CAGE KEY and FIRE KEY from lockbox

1.3.7. Obtain SI-LUX ARM KEY from instrumentation

1.3.8. Confirm all persons present during testing are ready for a trigger check, announce LASER GOGGLES ON

1.3.9. Arm the laser using SI-LUX software announcing ARMING LASER and LASER ARMED when the laser illumination source is being armed and is armed

1.3.10. Using the SI-LUX ARM KEY arm the laser announcing LASER ARMED when the laser is ARMED

1.3.11. Return to the Firebooth

1.3.12. Open Firebox Cage

1.3.13. Connect power supply to Firebox and ensure power is supplied (Green light on)

1.3.14. Insert FIRE KEY into Firebox, turn to arm system (Red light on), and press fire button

1.3.15. Disconnect power from Firebox (no green or red light) and close and lock Firebox Cage. Gun Operator retains CAGE KEY and FIRE KEY for all following steps

1.3.16. Approach gun system and turn Air Input Valve to “SAFE”. Visually confirm air cylinder rod has retracted

1.3.17. When the gun system has been Safed approach the laser illumination source, check that the laser has been disarmed. disarm the SI-LUX if necessary announcing LASER DISARMED

1.3.18. Turn off the laser illumination source and keep the SI-LUX ARM KEY announcing LASER OFF when clear

1.3.19. If air cylinder rod retracts and system operates as expected, the gun system is ready for operation.

1.3.20. If the air cylinder fails to retract, Gun Operator should repeat steps 1.3.2 through 1.3.13 after checking the following:

- Air Input Valve is set to “ARM”
- Air is supplied to control solenoid
- Trigger line from Firebox to control solenoid is undamaged
- Firebox outputs power when fire button is depressed

2. GUN FIRING PROCEDURE

(May only begin if Start of Day Pretest Sheet and all system checkouts have been performed. Perform for each test firing of the gun system)

2.1. **System Alignment**

2.1.1. Ensure power to Firebox is disconnected, Firebox cage is locked, breech is open, Air Input Valve is set to “SAFE”, and Chamber Flag is inserted in breech

2.1.2. Remove Chamber Flag and insert laser bore sight

2.1.3. Align target/gun for desired impact point

2.1.4. Visually inspect sabot stripper for damage which could degrade operation and ensure sandbags are in place on bottom tray

2.1.5. Align sabot stripper to ensure projectile will not impact stripper plate

2.1.6. When alignment complete, remove bore sight and insert Chamber Flag

2.2. **Cartridge Loading**

2.2.1. Ensure power to Firebox is disconnected, Firebox cage is locked, breech is open, Air Input Valve is set to “SAFE”, and Chamber Flag is inserted in breech

2.2.2. Clear BSL ground floor of all non-essential personnel. Non-essential personnel are to remain in the Visitors and Instrumentation Observation Loft during loading and firing of the gun system. The Firebooth is restricted to a maximum of three essential personnel only. The Test Engineer, Gun Operator, and Safety are the only personnel considered essential

2.2.3. Turn on ventilation fan. Ventilation fan is to remove combustion gases from BSL whenever necessary

The following steps are to be conducted by the Gun Operator only. Eye protection is required for all steps for all personnel, hearing protection is required for the gun operator from Step 2.2.9 and from Step 2.2.14 for all other personnel until the gun has been cleared. The CAGE KEY FIRE KEY and SI-LUX ARM KEY are to remain on the Gun Operator’s person at all times unless inserted in the Firebox Cage lock, Firebox, or SI-LUX laser unit, respectively.

2.2.4. Obtain propellant to be used for testing from the back room and bring to the loading bench. ONLY ONE powder may be on the loading bench at any given time

2.2.5. Install resizing dies on 50 BMG reloading press on loading bench

2.2.6. Deprime and resize propellant case (cutdown 50 BMG case)

2.2.7. If case originally had a crimped primer, deburr primer pocket

2.2.8. Use rotary scraper to remove carbon deposits

2.2.9. If removed primer was impacted, but did not initiate, return impacted primer to the lock box for later removal by EMRTC personnel

2.2.10. Remove resizing dies and install primer installing tool on 50 BMG reloading press

2.2.11. Insert No. 35 50 BMG primer, open end up, into tool and resized case into holder. Fully press primer into case (press until tool stops at preset depth). Check that primer face is recessed (~0.005”) below surface of the case base

2.2.12. Weigh out desired powder load for test using weigh boat on scale

2.2.13. Pour powder that has been weighed out into case using funnel. Press floral foam into case to fill empty volume and ensure powder is retained against primer

2.2.14. Place the projectile and loaded cartridge onto opposing sides of the gun stand and approach the laser illumination source

2.2.15. Announce LASER GOGGLES ON, arm laser announcing ARMING LASER and LASER ARMED when each step is completed

2.2.16. Turn on the laser illumination source using the SI-LUX ARM KEY announcing LASER ON

2.2.17. Return to gun and load projectile using depth gauge to achieve desired insertion depth in breech

2.2.18. Verbally announce “EARS ON, LOADING GUN” to all personnel. Insert loaded case into breech and close bolt

2.2.19. Engage cocking lever, then move to rear of gun and turn Air Input Valve to “ARM”

2.2.20. Return to Firebooth

2.2.21. Ensure non-essential personnel are behind barricades in the loft. Ensure essential personnel are behind Firebooth barricades

2.2.22. Open Firebox Cage and connect power to Firebox (Green light on)

2.2.23. Verbally announce “KEY IN” to all personnel and insert FIRE KEY into Firebox. Turn FIRE KEY to arm Firebox (Red light on)

2.2.24. Verbally announce countdown “FIRING IN THREE, TWO, ONE” to all personnel. Press orange fire button

2.2.25. After gun fires, verbally announce “KEY OUT” to all personnel, remove key from Firebox, disconnect power from Firebox, and lock Firebox Cage.

Retain CAGE KEY and FIRE KEY on person. Proceed to the Clear Gun Procedure (Section 2.3)

2.2.26. If gun fails to fire, verbally announce "KEY OUT" to all personnel, remove key from Firebox, disconnect power from Firebox, and lock Firebox Cage.
Retain CAGE KEY and FIRE KEY on person. Proceed to the Gun Misfire Procedure (Section 2.4)

2.3. **Clear Gun Procedure:**
The following steps are to be performed only by the Gun Operator. Eye and ear protection is to be worn by all personnel until gun has been announced as clear

2.3.1. Ensure power to Firebox is disconnected and Firebox cage is locked

2.3.2. Approach gun from rear and turn Air Input Valve to "SAFE"

2.3.3. Lower bolt and use extraction tool to remove case from breech. If case cannot be extracted using extraction tool, insert the brass pushrod into the muzzle and push case out of breech

2.3.4. Visually inspect breech/bore to ensure barrel is clear

2.3.5. Insert Chamber Flag into breech and verbally announce "GUN CLEAR" to all personnel

2.3.6. Approach the laser illumination source, disarm the laser announcing LASER DISARMED, and LASER OFF. Retain SI-LUX ARM KEY on person

2.3.7. Personnel may now remove laser safety goggles and return to the BSL main floor

2.3.8. For continued testing, return to step 2.1.1

2.4. **Misfire Procedure:**
The following steps are to be performed only by the Gun Operator. Eye and ear protection is to be worn by all personnel during these steps

2.4.1. Ensure power to Firebox is disconnected and Firebox cage is locked

2.4.2. Verbally announce “MISFIRE, 30 SECOND COUNT” to all personnel and begin a 30 second count

2.4.3. Approach gun from rear and turn Air Input Valve to “SAFE”

2.4.4. If cocking lever has not been pulled, disconnect cocking lever from bolt

2.4.5. Lower bolt and use extraction tool to remove loaded case

2.4.6. Return loaded case to loading bench and approach laser illumination source

2.4.7. Disarm SI-LUX laser announcing LASER DISARMED and LASER OFF, the gun operator retains the SI-LUX ARM KEY

2.4.8. If the misfire occurred due to a failure of the firing system (failure to trigger, broken firing pin, etc), return loaded case to loading bench. Make the necessary repairs to the firing system and return to Section 1.3: Fire System Checkout before returning to Step 2.2.13

2.4.9. If the firing system was observed to operate and a primer indentation found on the loaded case, return to Step 2.2.13 and proceed

2.4.10. If three misfires are observed, return loaded case to loading bench, remove foam wadding, and pour powder into weigh boat. Leave powder and set misfired primed case to the side. Return to beginning of firing procedure to proceed forward reloading a new case

2.4.11. If another misfire is observed with a newly primed case, suspend testing until the misfire cause can be identified and rectified

2.4.12. If three misfired are observed, return loaded case to loading benc, remove foam wadding, and pour powder to source container and set misfired primer to the side. Return to beginning of firing procedure to proceed forward reloading a new case

2.4.13. If another misfire is observed with a newly primed case, suspend testing until the misfire cause has been identified and rectified. Powder should be returned to source container and impacted primer to the lock box for later removal by EMRTC personnel

3. GUN POST TEST PROCEDURES

(Proceed if all testing with the gun system is complete for the day)

3.1. **System Hardware Shutdown (Firebooth and gun system)**

3.1.1. Ensure power is off to Firebox (No green or red light) by disconnecting power supply

3.1.2. Ensure Firebox Cage is locked

3.1.3. Approach gun from rear and switch Air Input Valve on air cylinder to “SAFE”

3.1.4. Visually confirm breech and barrel are clear. As required to conduct visual inspection, disconnect cocking handle, open breech, and/or remove Chamber Flag

3.1.5. Insert Chamber Flag into breech

3.1.6. Disconnect yellow airline from air supply

3.1.7. Return CAGE KEY and FIRE KEY to lockbox

3.1.8. Turn off ventilation system

Attachment 8

Revised Sand Catch Cleaning Operation Procedures

1. SANDCATCH POST TEST PROCEDURES

A revised sand catch is used to safely catch projectiles of greater mass than the original 55 gallon drum used for RP-19-01: Study High Velocity Impact of Reactive Materials Using 0.55 Caliber Powder Gun. Specifications on the revised sand catch are in accordance with TP-19-25 for lot testing of 50 BMG. The sand catch is approximately 1800 pounds fully loaded, and as such any lifting operations will be performed by those wearing hard hats and steel toes. The Titan Telescoping Gantry Cane has the lowest capacity rating of all components in the sand catch with a load rating of 3000 pounds. The minimum factor of safety for the lifting operation is 1.7 on the published ratings for all components. No fewer than two operators will be involved with the emptying of the sand catch. The sand catch will be cleaned after a maximum of 20 shots into the catch, or at the end of a test series where the next session will exceed the maximum number of shots before cleaning.

1.1. Distribute appropriate PPE

1.2. Move the gantry crane into place and the sand catch tub and cribbing into place for receiving the sand if fully dumping

1.3. Ensure that the casters on the gantry crane and the catch tub are locked

1.4. Attach the three lifting lugs of the sand catch chain hoist to the crane using the lifting straps, and D-Ring shackles

1.5. Tension the chain hoist without lifting the sand catch, check that all lengths of chain are equal and tensioning properly

1.6. Begin lifting using the chain hoist such that the sand catch is raised off of the steel welding table

1.7. Unlock the casters on the gantry crane and using team pushing to position the sand catch above the catch tub

1.8. Position the front 4 to 10 inches of the sand catch overhanging the catch tub

1.9. Lower the sand catch onto the cribbing and the catch tub

1.10. Translate the gantry crane back and attach the rearward lifting lugs on the sand catch onto the crane

1.11. Remove the face plate of the sand catch using the four toggle clamps

1.12. Tip the catch up slightly using the gantry crane

1.13. Remove all of the sand from the catch using a shovel

1.14. Inspect the rubber plug and the plywood for damage

1.14.1. Rubber plugs can be used for three shooting sessions

1.14.2. Plywood is to be replaced after every other shooting session, or if any damage is noted on the face

1.14.3. Visibly Inspect the AR500 back plate for damage, replace the AR500 plate if any damage is visible

1.15. Lay the sand catch back level, refill sand (if applicable) using shovels, and reinstall the faceplate on the catch

HIGH-SPEED QUANTITATIVE SCHLIEREN MEASUREMENT OF DENSITY FIELDS AROUND CONICAL SUPERSONIC PROJECTILES

by

Jason Michael Falls

NEW MEXICO TECH
SCIENCE • ENGINEERING • RESEARCH UNIVERSITY